Weak lensing shape measurement calibration studying effects of stronger shears and cluster contamination for the mass estimation of relaxed galaxy clusters

Dissertation
zur
Erlangung des Doktorgrades (Dr. rer. nat.)
der
Mathematisch-Naturwissenschaftlichen Fakultät
der
Rheinischen Friedrich-Wilhelms-Universität Bonn

von
Beatriz Hernandez Martin
aus
Madrid, Spanien

Bonn, 05.03.2020

Angefertigt mit Genehmigung der Mathematisch-Naturwissenschaftlichen Fakultät der Rheinischen Friedrich-Wilhelms-Universität Bonn.

1. Gutachter:	Prof. Dr. Peter Schneider
2. Gutachterin:	Prof. Dr. Thomas Reiprich
Tag der Promotion:	31.08.2020
Erscheinungsjahr:	2020

Para mi madre

Abstract

Weak lensing measurements suffer from well-known shear estimation biases, which can be partially corrected for with the use of image simulations. In this work we present an analysis of simulated images that mimick observations of high-redshift galaxy clusters as seen by different telescopes, including cluster specific issues such as non-weak shear and increased blending. Our synthetic galaxies have been generated to have similar observed properties as the background-selected source samples studied in the real images. The study of the bias coming from isolated galaxies, as well as the inclusion of the effect of neighbours and selection bias provide a round analysis of the different effects. The impact of cluster members was found to be negligible for high-redshift ($z > 0.7$) clusters, whereas shear measurements can be affected at the $\sim 1\%$ level for lower redshift clusters given their brighter member galaxies. The presence of faint neighbours and selection bias, however, is shown to be important to obtain robust bias estimates. Simulations were created mimicking the galaxy and telescope properties of cluster images from the Hubble Space Telescope Advance Camera for Surveys, the HAWK-I camera in the Very Large Telescope and the Hyper Suprime-Cam in the Subaru telescope. New corrections dependent on the signal-to-noise ratio are obtained for all of them, leading to a residual multiplicative bias below 1%, and an uncertainty level of $\sim 1.5\%$. The study of the systematic constraints for this bias is done by carefully analysing the impact of the different parameters used to create our simulations in the bias estimation. As an application we use the results obtained for the HST/ACS-like simulations for a refined analysis of three highly relaxed clusters from the SPT-SZ survey, where we now include measurements down to the cluster core ($r > 200$ kpc) as enabled by our work. Compared to previously employed scales ($r > 500$ kpc) this tightens the cluster mass constraints by a factor 1.38 on average.

Acknowledgements

I would like to thank first and foremost Tim for all your hard work, patience and support, answering all my questions and helping me when I needed. I also would like to thank you for the opportunity I had to do professional observations on your behalf in the Very Large Telescope in Chile. That is an experience that I will always remember.

Thanks to Peter for being my official supervisor and his help with the research, to Thomas for agreing to be my second supervisor and to the other members of the comitee for accepting to be a part of it.

Thanks to all my group members, present and past, for our discussions and their suggestions. Especially to Hannah, which has been a great support and always encouraging me on my research, but also a great friend outside of the institute who was always there when I needed to rant. To my officemates, Fatimah and Weiwei, I want to say that these years would not have been the same without our chats and our silly conversations.

My physics career started already a few years ago, with my bachelors, and I would not want to forget my friends from those days, which to this day still support me and are happy for my successes. Miguel, Sid, David Garces, David Gomez, Miguel Angel, Paloma, Gabriel, Jorge, David Amaro and Maria Angeles, you have been greatly missed throughout my time in Bonn, but I am glad we still managed to meet sometimes when I had time to go back to Madrid.

My masters time certainly brought a lot of new people into my life which unfortunately did not continue around. But one person has been incredibly missed. Julia, I know you would be proud of me.

During this PhD, I am greatful to have met amazing people who have always been there when I needed to complain but also for many game nights. Sven, Dato, Luis, Joseph, Diana, Maude, Devika, Nils, Alya, and more recently Benedetta, thanks for our lunches and good times. To everyone else who has been a part of my journey in the institute, thanks. My flat mate and neighbours, Pari, Johanna, Marcus and Bethina, sorry I was too busy to hang out most times, but it was nice to share our lovely house with you.

Finally, I wanted to have a special mention for the most important people in my life: my family. The support, encouragement and how proud you all are of me is what kept me going all this time. Dad, I miss you and love you. I hope you are happy for me. Mum, I don't know what I would do without you, thank you for coming to Bonn and helping me so much, even from far. Marcus, you are the best thing I got out of my PhD time. I don't think I could have done it without you. I look forward to what is coming next for us and giving everything back during your PhD.

Contents

CHAPTER 1

Introduction

The study of the objects that we can see in the sky has always been a fascinating subject through History. From the Ancient Greeks to the current era of large deep surveys with unimaginable amounts of data taken every second, the drive has been the same: to understand what is beyond our planet, where does everything come from and how it has evolved. The field of Cosmology properly started on the 20th Century and has developed inmensely in the recent years, in part thanks to the technological advances of big telescopes and charged couple devices (CCDs), which replaced photographic plates as the way to gather the light reaching the telescopes. Its ambitious aim to reach a fundamental general understanding of our Universe presents many challenges. The detailed study of the origin and evolution of our Universe has led us to the discovery of new physics, such as the dark matter and dark energy, which still present many unknowns. Another of such discoveries are gravitational waves, which after many years of simply being a theoretical prediction were finally observed in 2016 by the LIGO collaboration (Abbott et al. 2016).

Large collaborations, which aim to obtain large datasets that can constrain the cosmological parameters are common nowadays, with the Planck satellite (Planck Collaboration et al. 2011), the Kilo Degree Survey (de Jong et al. 2015), the Large Synoptic Survey Telescope (Ivezić et al. 2008), Hyper Suprime Cam (Miyazaki et al. 2012a) or the Dark Energy Survey (Flaugher et al. 2015). In the coming years, even larger advances will be made thanks to large telescopes both ground-based like the Extremely Large Telescope (Shearer et al. 2010), the Thirty Meter Telescope (Skidmore et al. 2015) and in orbit like Euclid (Laureijs et al. 2011), James Webb Space Telescope (Gardner et al. 2006) or eRosita (Merloni et al. 2012) that are being planned, constructed or recently launched. Preparations to achieve the maximum outcome out of their observations are well underway and are already proving useful (e.g. Euclid Collaboration et al. 2019, which will be useful later in this work). But in any case, nothing can be predicted about what new and exciting discoveries will be made in the future.

In 1916, Einstein proposed his General Relativity theory (Einstein 1916), which states that light is affected by the gravitational potential of other objects. This is the basis of the gravitational lensing effect, which has proven to be a very useful direct approach to measure

Figure 1.1: Cluster SDSS J0333+0651. Image taken by the Hubble Space Telescope. Credit: ESA/Hubble and NASA

masses in the Universe (e.g. Schrabback et al. 2018a). In this work, we focus on weak lensing, which happens for less massive objects and in regions further from their center. Due to the weaker nature many simplifications on the theory can be applied, but we require large numbers of galaxies to obtain meaningful results. Despite all its benefits, many systematic effects are still far from being controlled or even understood. For this reason the advance of lensing surveys needs to be supported by different works to better understand the methods used and their limits, as well as develop more advanced techniques that can help us obtain the best results with the next generation surveys.

Measuring masses using lensing works best for very massive objects which create large image distortions, such as galaxy clusters (an example of which is shown in Fig. 1.1), which provide a very good environment to study the contents of the Universe and their interactions, as they fairly represent them. They are the largest known structures which are gravitationally bound. Clusters have been studied in many different contexts, and using different tools as they can be observed in the optical, X-ray and radio regimes and each will probe a different element of the cluster. Galaxy cluster lensing studies are the best tool to obtain unbiased estimates of

the masses of the clusters, including the dark matter, which is not directly observed. Some works that have already provided mass estimations of large number of clusters are Schrabback et al. (2018a), Bellagamba et al. (2019) or McClintock et al. (2019). These clusters which have a mass estimate from lensing are then used to calibrate the scaling relations which connect observable properties with the weak lensing mass. These observables (such as X-ray luminosity, temperature, optical richness or the strenght of the Sunyaev-Zel'dovich effect) are later used as a proxy for the mass, by simply measuring them for new clusters and estimating their mass employing the scaling relation (e.g. Mantz et al. 2016, Dietrich et al. 2019). Even though this means we do not directly measure the mass of many clusters, observing them in the X-ray regime or through the Sunyaev-Zel'dovich effect is easier than doing a full lensing analysis. Furthermore, weak lensing mass estimates are generally quite noisy and the observable properties provide mass proxies with a low scattering. If the scaling relations are properly calibrated, they will provide more precise mass estimates. However, all the assumptions made in order to obtain the mass estimates can change the measured masses of the clusters, which will indirectly also affect any other related studies which rely on weak lensing mass measurements. This is the reason why understanding the limitations and uncertainties of our methods is key to trust scientific results coming from them.

Weak lensing is also used to map the matter distribution on large scales. Fluctuations in the foreground matter distribution in the Universe will create a distortion for the light coming from far away galaxies. This is known as cosmic shear. This distortion is typically much smaller than what can be found in the case of clusters, but can provide a good insight on the dark matter distribution in the Universe.

We approached this present work with the challenging task of reproducing and simulating how galaxy cluster images taken with a few telescopes look like and try to gather useful information on how one of the widely used weak lensing methods behaves, which problems it might have and possible corrections for them. With simulated images, we can compare the average measured distortion on the galaxy light with the "real" distortion we have put into our simulations. This helps us understand the bias that our methods introduce into the measurements which would be impossible to discern from real observations. However, the shortcomings of the creation of the simulations themselves proved to be more demanding than the original task. In this context, we aimed to reach valuable conclusions on the creation of simulations regarding the most crucial parameters which should be controlled when creating simulated data. This can help in the calibration of next generation surveys. The challenge of creating simulations, is the need to have realistic inputs for the galaxy and telescope properties. This means, ideally we should have data with a better resolution and greater depth in order to be able to use them as the "true" input data. This poses a small problem for ground-based observations, but is particularly difficult for this work, since in Chapter 3 we simulate very deep and high resolution data. More details on how we tackled this can be found in Chapter 3. Results obtained from these simulations are also directly put into use with the measurement of the mass of three galaxy clusters in Chapter 5. This is ultimately the goal of using simulated images: applying the knowledge that we get from it to real observations and verify that this can be done robustly.

Image simulations testing different weak lensing methods have been used in several

previous studies. Early work aimed to compare different shape measurement methods and understand how different they are. This was done by creating more general simulations, without the particulars of each telescope, and applying different weak lensing methods to study the bias they introduce. Some of these works include the Shear TEsting Program (STEP, Heymans et al. 2006) and the GRavitational lEnsing Accuracy Testing (Bridle et al. 2010; Mandelbaum et al. 2015). Some more recent work has focused on creating tailored simulations to the particular telescope and camera setup as well as science objectives, which will change the observed properties of the galaxies used for the analysis. This includes Pujol et al. (2017), Hoekstra et al. (2017), Fenech Conti et al. (2017), Mandelbaum et al. (2018a), Euclid Collaboration et al. (2019), Kannawadi et al. (2019) and many more. We should note, that all of them focus on cosmic shear studies, unlike in this work where we simulate galaxy cluster observations. The differences between these two approaches are mainly the shear regime that is simulated as well as the effects that blends and neighbours have on them. These works present interesting results which argue for the need of creating realistic simulations in order to fully capture the bias of the shape measurement. A selection of papers relevant to this work includes Euclid Collaboration et al. (2019), which simulates images for the Euclid survey and studies the influence of introducing faint undetected galaxies into the simulations. Euclid Collaboration et al. (2019) uses three different shear measurement algorithms, including the KSB+ implementation used in this work, which allows for a direct comparison with the current work (see Sect. 3.3). Mandelbaum et al. (2018a) presents simulations for the HyperSuprime-Cam survey (Aihara et al. 2018a), which we also do here in Sect. 4.2. Kannawadi et al. (2019) study in detail the importance of some of the choices of the input parameters on the bias estimation in a similar manner to what we do in Chapter 3, and we refer to it for comparison. The difference here is that they mimick observations of a ground-based telescope (KiDS), whereas we simulate space-based images from the Hubble Space Telescope (HST). This is discussed in Sect. 3.3.2.

In this work we created custom simulated images which resemble data from the Hubble Space Telescope/Advanced Camera for Surveys (Sirianni et al. 2005) in Chapter 3, the Very Large Telescope/HAWK-I (Kissler-Patig et al. 2008) in Sect. 4.1 and the Subaru/Hyper Suprime-Cam (Miyazaki et al. 2012a) in Sect. 4.2, selecting the adequate properties of our mock galaxies to resemble those used in lensing measurements of galaxy clusters with each of these setups. Careful considerations were taken to assure the most realistic selection of the galaxies and the reproduction of real systematics. An extension for regimes which exhibit a larger lensing effect as well as the analysis of the influence of background and foreground objects are also included here.

The layout of this work is as follows. In Chapter 2 we summarize the relevant cosmology and lensing theory and we present the methods used in this work. We describe the shear measurement method used, called KSB+. We also explain the basics of creating simulations, clusters and mass determination. In Chapter 3 we present the results obtained using simulated Hubble Space Telescope/Advanced Camera for Surveys images, including a detailed analysis of the changes in the bias due to the particular choices used in the creation of the simulations. We also study the effects that neighbours have in our estimates, as well as the presence of bright galaxies which are part of the cluster. An estimate of the impact the different steps in

our pipeline have on the bias is obtained and a final estimation of the different contributions to the bias is discussed in Sect. 3.4. In Chapter 4, we discuss the simulations from two other telescope setups: the VLT/HAWK-I and the Subaru/HSC. We derive estimations of the bias to use in future cluster work. In Chapter 5 we use the obtained calibrations from Chapter 3 to measure the mass of three relaxed galaxy clusters, improving their constraints with the knowledge acquired. In Chapter 6 we present our conclusions and the outlook for the next generation of surveys.

CHAPTER 2

Theory and methods

2.1 Cosmology

Cosmology is the study of the Universe as a whole and the understanding of its evolution. At small scales, the Universe is full of galaxies, stars and other celestial objects. However, there are no individual structures at scales larger than $\sim 200h^{-1}$Mpc. At these scales, the Universe is homogeneous and isotropic. This idea is known as the cosmological principle and it is one of the key elements on which cosmology is based. Observationally, it was found that most galaxies are receding from us. Assuming we are not in any privileged position in the Universe, this means that all points in space are moving away from each other and hence the Universe is expanding.

According to the results of the Planck satellite (Planck Collaboration et al. 2014), the Universe is made out of mostly ($\sim 68.3\%$) Dark Energy, which is a mysterious energy which drives the acceleration of the expansion that has been observed. The rest consists of matter. But only $\sim 4.9\%$ of the total contents is in the form of baryonic matter, which makes up all we can see. The other $\sim 26.8\%$ are Dark Matter (DM). This form of matter only interacts gravitationally and hence cannot be observed with our normal telescopes. Plenty of evidence, however, supports its existence. Its exact nature is unknown but we have a good understanding of its behaviour.

2.1.1 Brief History of the Universe

Time and space were created at the Big Bang, which happened 13.8 Gyr ago. The Universe then went through an inflation period, where it experienced a rapid expansion currently estimated to have lasted only 10^{-33} s (until $T = 10^{32}K$ was reached). The protons and antiprotons annihilated, and due to the slightly larger amount of protons than antiprotons, we ended up with a small number of protons still present. It is when we reached a temperature of about $T = 10^{10}K$ (1 second after the Big Bang) that the neutrino decoupling happened and neutrinos stopped interacting with baryonic matter. 100 seconds after the Big Bang

($T = 10^9 K$), electrons and positrons annihilated and neutrons and protons started combining to make atoms. Dark Matter inhomogeneities started to collapse at $T = 9000K$ (about 56000 yr after the Big Bang) and the first structures started forming (more on this on Sect. 2.1.5). 380,000 years after the Big Bang, at a temperature of $T = 3000K$ the Universe became neutral, since the electrons and the protons combined, creating neutral hydrogen. It is then that the Cosmic Microwave Background was created (more details of this in Sect. 2.1.4). The first stars started forming around 10^8 yrs, and the Universe evolved to what we see today.

2.1.2 Hubble expansion

The local Hubble law (Hubble 1929) correlates the distance (r) to a galaxy with the velocity (v) at which it is moving away from us, through the Hubble constant ($H_0 = 100\,h\,\mathrm{km\,s^{-1}Mpc^{-1}}$). A value of $h = 0.7403 \pm 0.0142$ has recently been measured with observations of the Hubble Space Telescope (HST; Riess et al. 2019). The Hubble law, which is valid on the local Universe, follows

$$v = H_0\, r. \tag{2.1}$$

Using General Relativity, we can characterize the Universe through the Robertson-Walker metric which is the most general form to describe an expanding, homogeneous and isotropic Universe,

$$\mathrm{d}s^2 = c^2\mathrm{d}t^2 - a(t)^2\left(\mathrm{d}\chi^2 + f_K^2(\chi)(\mathrm{d}\theta^2 + \sin^2(\theta)\mathrm{d}\phi^2)\right), \tag{2.2}$$

where $a(t)$ is the scale factor which characterizes the expansion of the Universe. We define the comoving radial coordinate χ and both θ and ϕ as the angular coordinates. The comoving coordinates stay constant with time as they follow the Hubble flow,

$$\chi = \int_t^{t_0} c\,\frac{\mathrm{d}t'}{a(t')}, \tag{2.3}$$

where t_0 is the time today. We define $f_K(\chi)$ as the comoving angular diameter distance, which depends on the curvature parameter K as

$$f_K(\chi) = \begin{cases} K^{-1/2}\sin(K^{1/2}\chi) & (K > 0) \\ \chi & (K = 0) \\ (-K)^{-1/2}\sinh[(-K)^{1/2}\chi] & (K < 0) \end{cases}. \tag{2.4}$$

This distance definition will be different depending on the geometry of the Universe. We have a closed Universe if $K > 0$. If $K < 0$, we are dealing with an open Universe, and if $K = 0$ we have a flat Universe, which is the case supported by observations of our Universe (Planck Collaboration et al. 2018).

The dependence of the scale factor with time can be described with the Friedmann equations,

$$\left(\frac{\dot{a}}{a}\right)^2 = \frac{8\pi G}{3}\rho - \frac{Kc^2}{a^2} + \frac{\Lambda}{3}, \tag{2.5}$$

and

$$\frac{\ddot{a}}{a} = -\frac{4\pi G}{3}\left(\rho + \frac{3p}{c^2}\right) + \frac{\Lambda}{3}\,, \tag{2.6}$$

where ρ is the density, p the matter pressure, and Λ accounts for the dark energy. $G = 6.67408 \times 10^{-11}\mathrm{m}^3\,\mathrm{kg}^{-1}\mathrm{s}^{-2}$ is the gravitational constant and $c = 2.998 \times 10^8$ m/s is the speed of light in a vacuum.

We define redshift (z) as the shift in the spectrum of the objects due to the expansion of the Universe. Objects situated further away from us will recede faster and will have a larger redshift, so it can be understood as a distance measure. Its definition is

$$z = \frac{\lambda - \lambda_0}{\lambda_0}\,, \tag{2.7}$$

where λ is the observed wavelength and λ_0 is the wavelength at emission. It is related to the scale factor as

$$a(t) = \frac{1}{z+1}\,. \tag{2.8}$$

We can also define the Hubble parameter, which depends on the scale factor as

$$H(t) = \frac{\dot{a}(t)}{a(t)}\,, \tag{2.9}$$

which can be particularized for today (t_0) to the Hubble constant, mentioned in Eq. (2.1). Using H_0, we can redefine the first Friedmann equation as

$$H^2 = H_0^2[\Omega_\mathrm{r} a^{-4} + \Omega_\mathrm{m} a^{-3} + (1-\Omega_0)a^{-2} + \Omega_\Lambda]\,, \tag{2.10}$$

where $\Omega_\mathrm{r} = \frac{\rho_\mathrm{r}}{\rho_\mathrm{cr}}$ is the radiation density parameter, which is negligible today but was important in the past due to its strong evolution with the scale factor of a^{-4}. $\Omega_\mathrm{m} = \frac{\rho_\mathrm{m}}{\rho_\mathrm{cr}}$ is the matter density parameter and $\Omega_\Lambda = \frac{\rho_\Lambda}{\rho_\mathrm{cr}}$ is the dark energy density parameter. $\Omega_0 = \Omega_\mathrm{r} + \Omega_\mathrm{m} + \Omega_\Lambda$ is the total density parameter which determines the curvature of the Universe. The values of the density parameters give us an idea of the relative contents of the Universe, and are critical in understanding how it evolved. The critical density used in the definition of the density parameters is

$$\rho_\mathrm{cr} = \frac{3\,H_0^2}{8\,\pi\,G} = 1.88 \times 10^{-29} h^2 \mathrm{g/cm}^3\,. \tag{2.11}$$

The values of the different cosmological parameters have been obtained independently by different probes and they agree remarkably. Examples of these probes can be CMB analyses (e.g. Goldstein et al. 2003, Rebolo et al. 2004, Planck Collaboration et al. 2018), cosmic shear (e.g. Hildebrandt et al. 2017), Supernova type Ia results (e.g. Blinnikov & Sorokina 2004), or neutral hydrogen observations (e.g. Bharadwaj et al. 2009). This indicates that the Standard Model is a good framework for the Universe, which with a small set of parameters describes a large variety of observations.

2.1.3 Cosmological distances

In the non-Euclidean space there is no unique description of distances. One of the most common ways to measure distances in extragalactic astronomy is the redshift mentioned before. But we can also use alternative distance definitions. The comoving distance, also explained above, follows the Hubble flow so it is not affected by the expansion of the Universe. This means that there is no direct way for us to measure it. Instead, we can define two distances which are easier to measure and more easily related to our everyday Euclidean life: the angular diameter distance and the luminosity distance. The angular diameter distance relates the physical size of objects (diameter d) to the observed size (δ) as

$$D_{\rm ang}(z) = \frac{d}{\delta} = a(z) f_K(\chi)\,. \tag{2.12}$$

Due to the geometry of the Universe, there is a maximum possible angular diameter distance which depends on Ω_Λ. Assuming the current best estimate of $\Omega_\Lambda \simeq 0.7$, the maximum distance is situated around $z \sim 1.6$ and corresponds to around $\sim 1800\,$Mpc.

Another description of distances can be obtained relating the luminosity of an object (L) and the observed flux (S)

$$D_{\rm lum}(z) = \sqrt{\frac{L}{4\pi S}}\,. \tag{2.13}$$

The luminosity distance does not have a maximum value and continues to grow as a function of redshift. Both distance measures can be related by

$$D_{\rm lum}(z) = (1+z)^2 D_{\rm ang}(z)\,, \tag{2.14}$$

which shows that they agree for $z \ll 1$ and are interchangeable for the local Universe. These distances are not additive, meaning $D_{\rm ang}(z_1 + z_2) \neq D_{\rm ang}(z_1) + D_{\rm ang}(z_2)$ and the same happens for the luminosity distance. The decision of which distance should be used is not general and it intrinsically depends on the problem we are studying. When we deal with lensing, we generally deal with sizes, so the angular diameter distance is used in this case.

2.1.4 Cosmic Microwave Background

After the Big Bang, the Universe was very dense and the mean free path of the photons was smaller than the separation of the particles. Photons and electrons were coupled by Thomson scattering and in thermal equilibrium. This means that no photons could escape the mix and freely travel reaching us today. Instead they kept interacting with other particles. Once the Universe had expanded enough ($z \sim 1100$) the photons could finally escape. This is known as the surface of last scattering which created a hot radiation background, about 380,000 years after the Big Bang. This background has cooled due to the expansion of the Universe reaching a temperature today of $T \sim 2.7K$ and it is known now as the Cosmic Microwave Background (CMB) since it can be observed in the microwave regime.

In Fig. 2.1 we show an image of the CMB from the Planck satellite (Planck Collaboration

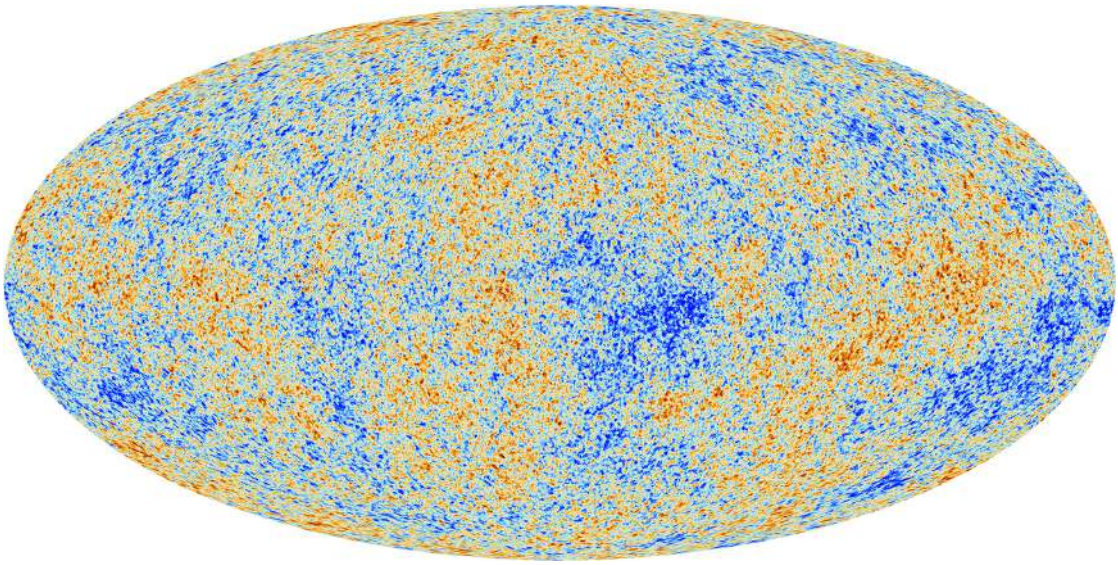

Figure 2.1: Temperature map of the CMB. This is a linear combination of the Planck single frequency maps in order to remove contamination from the foreground. Credit: ESA and the Planck Collaboration

et al. 2011). Planck has observed the CMB at different frequencies in the radio regime, from 30 to 857 GHz. There are small temperature fluctuations of the order $\frac{\Delta T}{T} \sim 10^{-5}$ which we can study and they can help us constrain the cosmological parameters (Planck Collaboration et al. 2018) that characterise the Standard Model of Cosmology. In combination with other probes, the CMB anisotropy measurements provide quite precise constraints on a number of cosmological parameters. One disadvantage is cosmic variance which is the statistical error introduced due to only being able to see one realization of the CMB. This is particularly important at large scales, above 10 deg. An analysis of the particular placement of the peaks does not provide any meaningful information, however, a statistical analysis of the number of peaks at different scales is what allows to constrain the cosmological parameters.

2.1.5 Structure formation

As mentioned before, the Universe is considered homogeneous and isotropic on large scales. Tiny perturbations present at early times are the precursors of the large structures we see today, for example, in the form of galaxies and galaxy clusters. These small perturbations are present in the early times as shown by the CMB through the anisotropies (see Fig. 2.1). Evidence of the inhomogeneities today are the large structures which clump together following the Dark Matter (DM) overdensities that are not directly observable. Connecting these overdensities (or halos) we find filaments. In between filaments and halos, we can see empty regions, called voids. A sample image of the DM-only Millenium simulation (Springel et al. 2005) where halos and filaments are visible is shown in Fig. 2.2. Galaxy clusters, which are the main subject of this work, live in the DM halos so the evolution of halos and clusters is closely

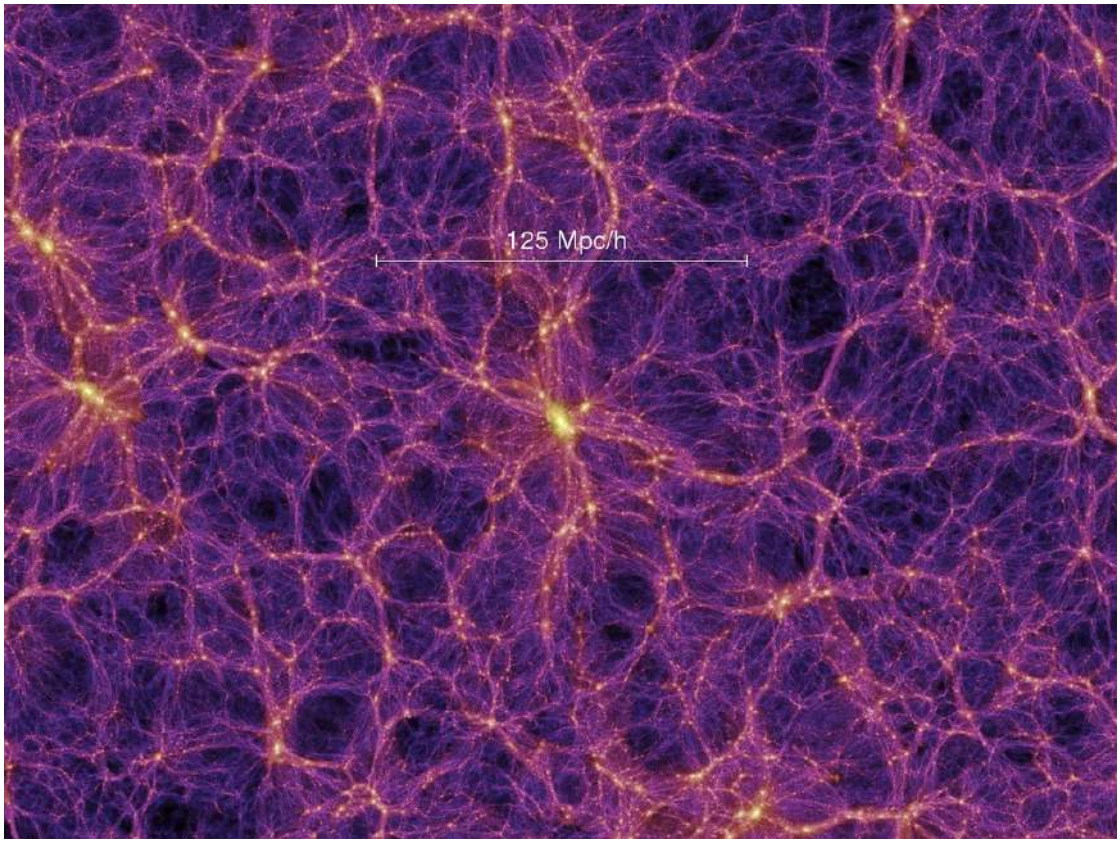

Figure 2.2: Image of the Millenium Simulation. Credit: Springel et al. (2005)

linked.

For an analytical description of the DM structures in the Universe, we define the density contrast as

$$\delta(\mathbf{x}, t) = \frac{\rho(\mathbf{x}, t) - \bar{\rho}(t)}{\bar{\rho}(t)}\,, \tag{2.15}$$

where $\rho(\mathbf{x}, t)$ is the DM density as a function of position and time and $\bar{\rho}(t)$ is the mean DM density which only depends on time. Because the fluctuations are small we can simply use linear perturbation theory to obtain the equations that describe their growth:

$$\frac{\partial \delta}{\partial t} + \frac{1}{a}\nabla_x \cdot \mathbf{v} = 0\,, \tag{2.16}$$

$$\frac{\partial \mathbf{v}}{\partial t} + \frac{\dot{a}}{a}\mathbf{v} = -\frac{1}{a}\nabla\Phi\,, \tag{2.17}$$

$$\nabla_x^2\Phi = \frac{3H_0^2\Omega_\mathrm{m}}{2a}\delta\,. \tag{2.18}$$

Here, $\mathbf{v}$ is the velocity field of the DM particles, and Φ is the comoving potential of the field.

These equations describe how small fluctuations evolve and create the DM clumps that host the large structures we see.

Looking at the link between the tiny inhomogeneities of the CMB and the large structures we see today can indicate they were created in a hierarchical way, small structures formed first and merged to create larger objects. This hierarchical process is mainly driven by Cold Dark Matter (CDM), which means that the DM particles have low velocities compared to the speed of light.

Halo formalism

The model of spherical collapse predicts virialized halos given an initial density perturbation following a Gaussian random field (Press & Schechter 1974). In order to analytically describe such halos, Navarro et al. (1995) and Navarro et al. (1997) used a universal radial profile (Navarro, Frenk and White, or NFW profile) for DM halos,

$$\rho(r) = \frac{\rho_{\rm cr}\delta_{\rm char}}{r/r_{\rm s}(1+r/r_{\rm s})^2}\,, \tag{2.19}$$

with $\rho_{\rm cr}$ the critical density of the Universe and the parameters of the profile which are the characteristic overdensity, $\delta_{\rm char}$, and the scale radius, $r_{\rm s}$. Due to this simple form for the DM halos, the creation of DM-only simulations and their comparison with real observations can indicate if CDM is a good model and help distinguish between alternative DM scenarios. Furthermore, the study of real halos will provide insight on the disturbances introduced by the baryons. To date we still find discrepancies between simulations and observations which indicate some processes are not well understood. This can be seen e.g. in de Blok (2010) or Munari et al. (2016). One particular aspect which can also be studied is the abundance of DM halos as a function of their redshift and mass. If we compare it with the predictions of the Press Schechter formalism (Press & Schechter 1974) it provides insight on the value of the cosmological parameters. Another issue is caused by the fact that the DM halos cannot be directly observed and instead we need to look at the objects that populate them. This is not a simple comparison as we need to understand the relation between mass and the observable mass proxies, such as richness.

We can formally define a halo as a roughly spherical region with a mean density ≥ 200 times larger than the critical density of the Universe at the time ($\rho_{\rm cr}$) and parametrize it with the radius (r_{200}) of the region with such density. The mass of the halos can be obtained with

$$M_{200} = \frac{4\pi}{3} r_{200}^3 200\rho_{\rm cr}(z) = \frac{100 r_{200}^3 H^2(z)}{G}\,. \tag{2.20}$$

We can also have an alternative definition if we select an overdensity which is 500 times larger than $\rho_{\rm cr}$, and similarly define r_{500} and M_{500}. The abundance of halos is smaller for higher redshift and for more massive halos. For a fixed mass, r_{200} decreases with redshift. In general, there are fewer massive halos as compared to less massive ones and at earlier times clusters were fewer and smaller.

The halo model assumes all matter is contained in halos, which is a good approximation, according to simulations (Press & Schechter 1974, White et al. 2001). So the total density of the Universe is just the sum of the density in all halos

$$\rho(\mathbf{x}) = \sum_i \rho_h(|\mathbf{x} - \mathbf{x}_i|; M_i)\,, \tag{2.21}$$

where $\mathbf{x}_i$ is the position of each halo and M_i the corresponding mass. This model assumes that halos are populated by a central galaxy and some satellite galaxies following an NFW profile. The mass in the inner parts of halos can be obtained by looking at the velocity dispersion of the galaxies that are located there. In the outer parts, however, there are no luminous tracers and it is only with weak lensing that we can estimate the mass of these regions (see Sect. 2.3.2).

To describe the internal distribution of the matter, we can use the concentration index which indicates how concentrated the mass is at the center of the halo,

$$c_{200} = \frac{r_{200}}{r_\mathrm{s}}\,, \tag{2.22}$$

where r_s is the characteristic radius in the NFW profile. The NFW profile can be parametrized by c_{200} and r_{200} or the mass of the halo. We can define the total mass of a halo depending on the concentration parameter (see Eq. 2.22). This is the so-called concentration-mass (c-M) relation, which comes from a parametrization of the NFW profile and reads

$$M_{200} = 4\pi\rho_\mathrm{s} r_\mathrm{s}^3 \left(\ln(1 + c_{200}) - \frac{c_{200}}{1 + c_{200}}\right)\,. \tag{2.23}$$

An empirical determination of the c-M relation can be found in Merten et al. (2015) which correlates the concentration for relaxed halos with the mass of the halo and the redshift. It approximately follows

$$c_{200} \approx 6.7 \left(\frac{M_{200}}{2\times 10^{12} h^{-1} M_\odot}\right)^{-0.1} (1+z)^{-0.5}\,. \tag{2.24}$$

This was obtained empirically through a lensing analysis of 19 X-ray selected galaxy clusters from the Cluster Lensing and Supernova Survey with Hubble (CLASH, Postman et al. 2012), for a redshift range $z = [0.19 - 0.89]$. However, we should point out that empirical measurements have shown discrepancies to numerical simulations (see Merten et al. 2015). Current studies including N-body simulations have found small deviations from the self-similarity of NFW models (e.g. Ramos-Ceja et al. 2015, Hill et al. 2018). For a more accurate representation of halos, some studies found that a slightly better model is an Einasto profile (Merritt et al. 2006)

$$\rho(r) = \rho_s \exp\left(\frac{-2}{\alpha}\left[\left(\frac{r}{r_s}\right)^\alpha - 1\right]\right)\,, \tag{2.25}$$

where r_s is, again, the characteristic radius, ρ_s is the density at that radius and α is a parameter determining the shape, which is currently assumed to be $\alpha \sim 0.17$.

However, this is not the full story. So far we have assumed DM-only and due to this, only gravitational interactions. The presence and interactions of baryonic matter can disrupt these smooth profiles via effects such as baryonic feedback, AGNs or mergers. In particular, dissipative processes can change the gravitational potential which will also affect the DM distribution. This is important for smaller scales comparable to the size of galaxies, where the baryonic influence becomes important. Currently, these disruptions are not considered a major influence on the matter distribution within clusters of galaxies.

2.2 Galaxy clusters

Galaxy clusters are one of the most massive gravitationally bound objects in the Universe so the knowledge of their mass is of great importance to Cosmology. They populate the DM halos and serve as tracers of their mass. An example image of a galaxy cluster can be seen in Fig. 2.3. They are made up of galaxies, hot intracluster medium (ICM, with a temperature of $\sim 10^7 K$) and the DM halo. They have around 100 to 1,000 galaxies, masses of $10^{14} - 10^{15}\, M_\odot$ and their sizes are $2 - 10$ Mpc. The central galaxies of many clusters host Active Galactic Nuclei (AGN) which play an important role heating up the ICM. Each different observational regime will probe one of the different components of the cluster, providing us with valuable astrophysical information. Using X-rays we can observe the ICM (due to thermal Bremsstrahlung), in radio we can study the presence of cosmic rays and magnetic fields in the ICM (van Weeren et al. 2019), in the optical regime we can observe the stars and with gravitational lensing (discussed in the next section, Sect. 2.3), we are able to measure the total mass, including the dark matter.

Clusters can be detected through inverse Compton scattering of the CMB caused by hot electrons in the ICM. This is known as the Sunyaev Zel'dovich effect (Sunyaev & Zeldovich 1969). The CMB spectrum locally deviates from a Planck spectrum at the cluster positions causing a signature shift in the spectra as shown in Fig. 2.4. In this process there is no creation or destruction of photons but only a transfer from the low-energy end of the spectrum to the high-energy part. The SZ effect does not depend on redshift, allowing us to obtain nearly mass-limited samples (instead of e.g. flux-limited in X-rays). However, clusters found through this effect need follow-up observations to measure the cluster redshift. Another method to detect clusters is using the colour-magnitude diagram. When plotting their colour (difference in magnitude between two observed bands) against their magnitude in one band, the early-type galaxies will be situated in a nearly horizontal line, known as red sequence (Gladders & Yee 2000). The position of this line will be different, depending on cluster redshift. Fitting the sequence to templates, we can obtain a rough estimate of the redshift. However, the most reliable method for determining cluster redshift is through spectroscopic measurements (e.g. Dressler et al. 1999, Bayliss et al. 2011, Khullar et al. 2019).

One of the applications of large cluster surveys is, for example, studying the cluster mass function and its evolution with redshift, which allows us to constrain the cosmological

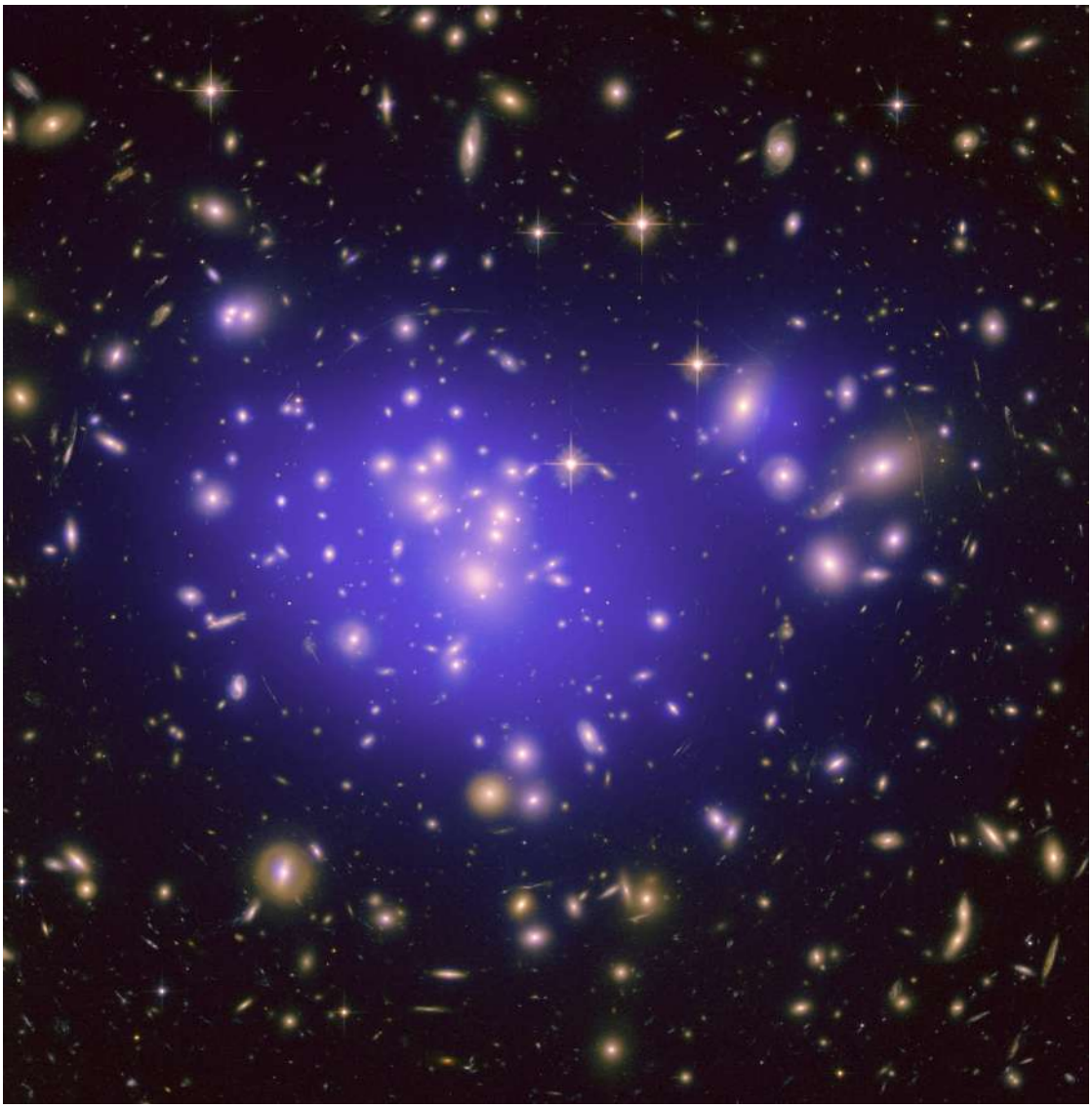

Figure 2.3: Cluster Abell 1689 observed with the Hubble Space Telescope. This is a combined image where we see the galaxy light observed in the optical, but also the Dark Matter estimation from weak lensing overlayed in blue. Credits: NASA/ESA/JPL-Caltech/Yale/CNRS

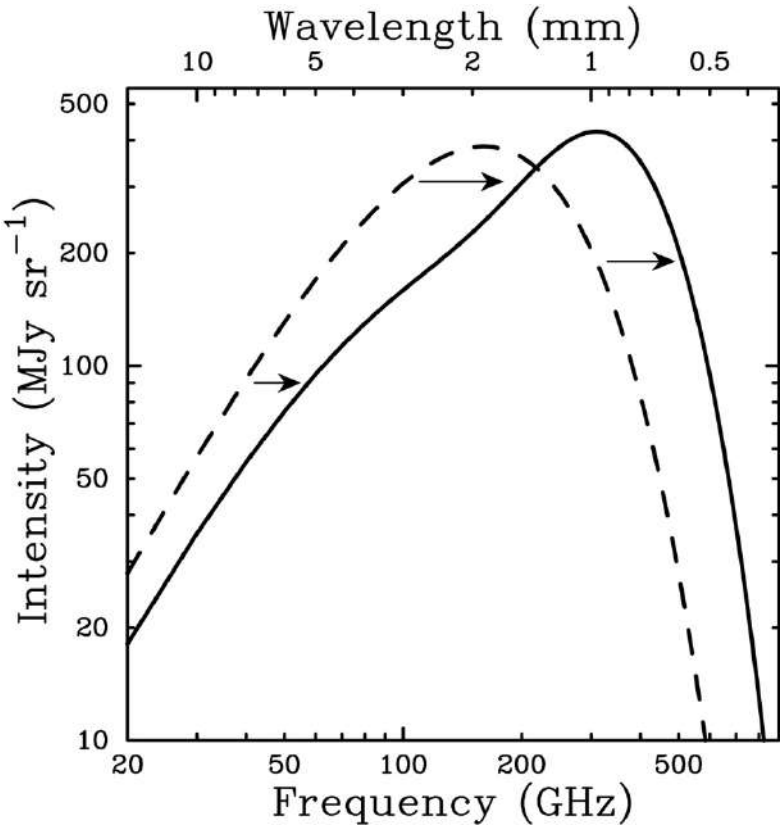

Figure 2.4: Frequency shift due to the Sunyaev-Zel'dovich effect. The shown effect is highly exaggerated for illustration purposes. Figure from Carlstrom et al. (2002).

parameters (Allen et al. 2011). The comparison e.g. between the X-ray and lensing mass estimates helps with the understanding of the cluster structure. In addition, it is believed that the matter content of rich clusters of galaxies is representative of the matter content of the whole Universe (White et al. 1993) so a detailed study of clusters provides information also on the Universe as a whole. The cluster abundance can be compared to theoretical predictions from cosmology (Bahcall & Cen 1993) which provides a good test for our general cosmological understanding.

There are multiple ways to estimate cluster masses, such as through lensing, mass reconstruction from X-ray observations, SZ mass estimates or richness-based mass estimates. Each of the different mass determination methods is valid only within a certain radial regime and under some particular assumptions so we benefit from their joint use to have a global analysis. In particular, lensing (see Sect. 2.3) is the only method which allows for a direct measurement of the total projected mass inside a cluster. X-ray estimates often assume virial equilibrium. With lensing, however, we can constrain the total projected mass distribution without any equilibrium assumptions. Clusters are dark matter dominated outside of the central regions so it is important to use lensing estimates in those regions as other methods

do not directly probe the DM. Opposed to this, weak lensing cannot reach within $\sim$ 100kpc of the cores, so an alternative approach needs to be used there. Strong lensing can be helpful there for massive clusters. Masses are often estimated using scaling relations, which need accurate weak lensing mass estimates as a calibration to find the link between cluster mass and observables such as X-ray luminosity or temperature, optical richness or SZ decrement. These observables derived from the hot gas or the stars act as mass proxies, which cannot directly measure the DM. However, once the scaling relations are calibrated, they are easily applied to other clusters as a first estimate of their mass which is generally easier to obtain than their full lensing analysis. Furthermore, some of the mass proxies (e.g. $M_{\rm gas}$) have a low scatter with the true mass, so if the scaling relations have been accurately and precisely calibrated, these proxies can provide a more precise mass estimate. Because of this, they are a useful tool despite not being a direct measurement.

In Chapter 5 of this work, we measure the mass of three clusters, which are selected from the 2,500 deg^2 South Pole Telescope Sunyaev-Zel'dovich (SPT-SZ) Survey (Bleem et al. 2015). This survey was completed in 2011 and it was designed to discover a large number of high-z clusters through the SZ effect. Observations of the CMB were taken at 95, 150, and 220 GHz. They used different sized profiles to filter the images and then cluster candidates are extracted via a peak detection algorithm. For more details on this see Bleem et al. (2015). Some of these clusters were followed-up by WL analyses (see Schrabback et al. 2018a, hereafter known as S18a) and the results of the cosmological constraints obtained from them are presented in Bocquet et al. (2019). From the SPT-SZ Survey we have selected the three most relaxed clusters, which will better serve as a test to measure cluster mass including the inner cluster regime which has been excluded up to now.

Relaxed clusters

Dynamically relaxed clusters are those which have not suffered any recent mergers or disturbances and present a uniform temperature and density profile because they are in dynamical equilibrium. These profiles are symmetric and regular. Alternatively, the relaxation criteria can be defined based on the smooth distribution of their member galaxies (e.g., Carlberg et al. 1997; Wen & Han 2013; Old et al. 2018). In particular, these clusters tend to have a very massive galaxy really close to their center, known as the Brightest Cluster Galaxy (BCG) which normally host AGNs and is very bright in the radio regime. In relaxed clusters, the second brightest galaxy typically has a large luminosity gap with respect to the BCG.

Relaxed clusters often feature 'cool cores' with a strong drop in the temperature profile at the center of the cluster, which coincides with an increase of the density profile. Because of their smooth distributions, their mass can generally be constrained with low biases and high precision, which has made them the centre of multiple studies (e.g. Mantz et al. 2015). Relaxed clusters contain mostly early-type galaxies which have quite uniform colours. These galaxies are concentrated towards the centre, with a high central galaxy density. In these clusters, mass estimates from X-rays and lensing generally agree quite well as opposed to clusters which are not in hydrostatic equilibrium where the discrepancy between mass

estimates is much larger. When estimating the cluster centre, we have a similar situation. For relaxed clusters, the X-ray, SZ and optical centers are generally located close to each other, which is not true for the general cluster population. This reduces the influence that miscentering can have in the mass reconstruction for relaxed clusters and it allows for a more robust weak lensing mass determination. Furthermore, the shape of the mass profile typically follows the distribution of galaxies. The relaxation criteria followed to determine relaxed clusters in the SPT-SZ Survey was the presence of a bright cool core of X-ray emitting gas centered on the X-ray centroid and having isophotal ellipses after follow up observations with *Chandra* (see Mantz et al. 2015 and McDonald et al. 2019).

In general, X-ray surveys are biased in favor of finding relaxed clusters due to the larger surface brightness of these objects caused by their cool cores. In order to systematically identify them, there have been mainly two methods. The first is measuring bulk asymmetries (e.g. Mohr et al. 1993, Buote & Tsai 1995), and the second is quantifying the presence of a cool core (e.g. Santos et al. 2008, Böhringer et al. 2010).

A useful study on clusters for Cosmology is the measured gas fraction ($f_{\rm gas}$), which provides constraints on the cosmic expansion and cosmology via the $f_{\rm gas}$ test (Allen et al. 2011). The gas fraction is

$$f_{\rm gas}(z) = \Upsilon(z)\frac{\Omega_{\rm b}}{\Omega_{\rm m}}\,, \tag{2.26}$$

where $\Upsilon(z)$ accounts for the baryon effects that occur at that redshift and it is expected to be small in the regions where the ICM is the main source of baryons. $\Omega_{\rm b}$ is the baryon density.

Assuming fair matter samples, the measurements of $f_{\rm gas}$ allow us to break the degeneracy between $\Omega_{\rm m}$ and the dark energy equation of state, w. Because of the tight Big Bang Nucleosynthesis constraints on $\Omega_{\rm b}$, $f_{\rm gas}$ measurements provide a strong evidence of $\Omega_{\rm m} \ll 1$ (White et al. 1993). Since cosmological constraints are obtained from $f_{\rm gas}$ measurements as a function of redshift, we need to ensure that the mass estimates are robust for different z. The mass estimation of the selected high-z clusters discussed in this work (see Sect. 5) will contribute to improve the constraints of the $f_{\rm gas}$ measurements for higher redshifts.

2.3 Gravitational lensing

The light rays coming from far away objects are deflected as described by General Relativity within the gravitational potential of massive foreground objects (known as lenses). This effect provides us with a useful tool, allowing for the measurement of the changes of the observed position, flux and shape of the source images due to this so-called gravitational lensing. This effect allows us to measure the mass of the lenses by observing the apparent changes in background objects. Since lensing only depends on the gravitational potential, we can estimate the total mass, from both baryonic matter and DM.

2.3.1 The lensing theory

To understand the lensing effect, we present in Fig. 2.5 a sketch of the lens and source planes. In the figure, the lens and source distances and the different angles describing all the positions are illustrated, which are related through the lens equation

$$\boldsymbol{\beta} = \boldsymbol{\theta} - \boldsymbol{\alpha}(\boldsymbol{\theta}) \,, \tag{2.27}$$

where $\boldsymbol{\beta}$ is the angular position of the source (unlensed) with respect to the optical axis, $\boldsymbol{\theta}$ is the angular position of the image and $\boldsymbol{\alpha}(\boldsymbol{\theta})$ is the scaled deflection angle, which is related to the true deflection angle (depicted in Fig. 2.5) as

$$\boldsymbol{\alpha}(\boldsymbol{\theta}) = \frac{D_{\rm LS}}{D_S}\tilde{\boldsymbol{\alpha}}(\boldsymbol{\theta}) \,, \tag{2.28}$$

where D_S and $D_{\rm LS}$ are the angular diameter distances from the observer to the source and from the lens to the source, respectively. $\boldsymbol{\eta}$ are the coordinates of the source in the source plane and $\boldsymbol{\xi}$ is the projection of the position of the image onto the lens plane. All this is true assuming small angles $|\boldsymbol{\beta}|, |\boldsymbol{\theta}|, |\tilde{\boldsymbol{\alpha}}| \ll 1$. We also assume that the distances are much larger than the size of the lens and that the light rays travel in straight paths and are only deflected in the lens plane, which is known as Born approximation.

We can define the convergence κ as

$$\kappa(\boldsymbol{\theta}) = \frac{\Sigma(D_{\rm L}\boldsymbol{\theta})}{\Sigma_{\rm cr}} \,, \tag{2.29}$$

where the surface mass density $\Sigma(D_{\rm L}\boldsymbol{\theta})$ and the critical surface mass density $\Sigma_{\rm cr}$ are defined as

$$\Sigma(D_{\rm L}\boldsymbol{\theta}) = \int {\rm d}z\, \rho(\xi_1, \xi_2, z) \,, \tag{2.30}$$

$$\Sigma_{\rm cr} = \frac{c^2 D_{\rm S}}{4\pi G D_{\rm L} D_{\rm LS}} \,. \tag{2.31}$$

Here, $D_{\rm L}$ is the distance to the lens and z is the redshift.

The definition of κ allows us to differentiate between two cases. When $\kappa \geq 1$ we have multiple images and we are in the strong lensing regime. This means the distortion is large and can be seen by eye. There are luminous arcs, and in some particular configurations even a ring around the cluster centre. This only occurs in the innermost parts of clusters (around $50h^{-1}$kpc), which means we do not generally get information on the properties of the outskirts through strong lensing. For $\kappa \ll 1$ we are in the weak lensing regime, which is what is used in this work. For weak lensing, we can only use statistical methods, since the distortion on one galaxy caused by lensing is too small to provide any meaningful information based on just that one galaxy.

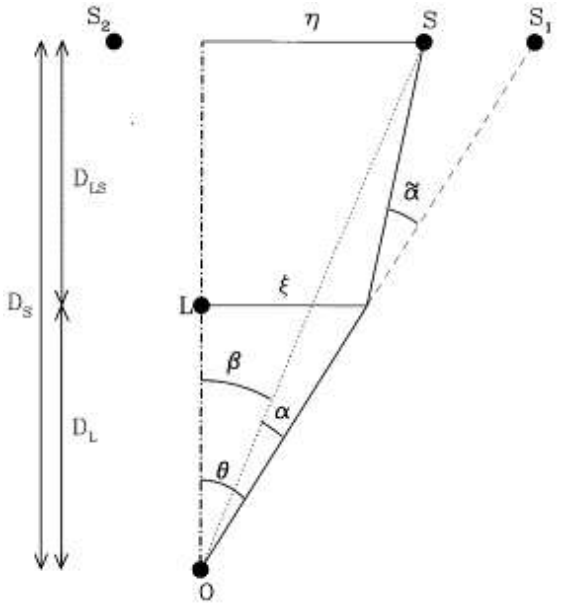

Figure 2.5: Sketch of the lens and source plane. $\boldsymbol{\eta}$ is the position of the source, $\boldsymbol{\xi}$ is the projected position of the image on the lensing plane. $\boldsymbol{\beta}$ is the angular position of the unlensed source, $\boldsymbol{\theta}$ is the angular position of the image and $\boldsymbol{\alpha}(\boldsymbol{\theta})$ is the scaled deflection angle. D_{S} is the angular diameter distance to the source, D_{L} to the lens, and D_{LS} the distance from lens to source. Figure taken from Wambsganss (1999).

The distortion of images is described by the Jacobian matrix,

$$\mathcal{A}_{ij} = \frac{\partial \beta_i}{\partial \theta_j} = \left(\delta_{ij} - \frac{\partial^2 \psi(\boldsymbol{\theta})}{\partial \theta_i \partial \theta_j} \right) , \tag{2.32}$$

where the deflection potential is defined as

$$\psi(\boldsymbol{\theta}) = \frac{1}{\pi} \int_{\mathbb{R}^2} \mathrm{d}^2\theta' \kappa(\boldsymbol{\theta}') \ln |\boldsymbol{\theta} - \boldsymbol{\theta}'| \, . \tag{2.33}$$

The deflection potential satisfies the Poisson equation $\nabla^2 \psi = 2\kappa$ and its gradient is the scaled deflection angle $\boldsymbol{\alpha} = \nabla \psi$ which indicates the strength of the deflection. The magnification indicates the ratio of the lensed and the unlensed flux and it is defined as

$$\mu(\boldsymbol{\theta}) = \frac{1}{\det \mathcal{A}(\boldsymbol{\theta})} \, . \tag{2.34}$$

For an idealised galaxy, with elliptical isophotes, we can define ellipticity as

$$|e| = \frac{a - b}{a + b} \, , \tag{2.35}$$

where a and b are the sizes of the semi-major and semi-minor axis, respectively. The two ellipticity components are

$$e_1 = |e| \cos 2\phi \,, \tag{2.36}$$

$$e_2 = |e| \sin 2\phi \,. \tag{2.37}$$

ϕ indicates the angle between the semi-major axis of the ellipse and the x-axis.

If we define the shear as

$$\gamma_1 = \frac{1}{2}\left(\frac{\partial^2\psi(\boldsymbol{\theta})}{\partial\theta_1\partial\theta_1} - \frac{\partial^2\psi(\boldsymbol{\theta})}{\partial\theta_2\partial\theta_2}\right), \tag{2.38}$$

$$\gamma_2 = \frac{\partial^2\psi(\boldsymbol{\theta})}{\partial\theta_1\partial\theta_2}, \tag{2.39}$$

this indicates the distortion in the ellipticity of the object due to the lens.

The reduced shear can be expressed as

$$g = \frac{\gamma}{1-\kappa}, \tag{2.40}$$

which is important in weak lensing. This allows us to redefine the Jacobian as

$$\mathcal{A}_{ij} = (1-\kappa)\begin{pmatrix} 1-g_1 & -g_2 \\ -g_2 & 1+g_1 \end{pmatrix}, \tag{2.41}$$

which separates the contribution of the isotropic magnification due to the convergence and the anisotropic distortion caused by the shear. A sketch is presented in Fig. 2.6 to illustrate this distinction. The surface brightness stays invariant under lensing effects.

2.3.2 Weak lensing

Weak lensing (WL) happens when $\kappa \ll 1$. Here, the lensing distortion is small compared to the intrinsic ellipticity of galaxies. This means that we cannot study the resulting effect on individual galaxies but we require a statistical analysis of a large number of them. It relies on the assumption that galaxies are randomly oriented in the Universe and thus their intrinsic ellipticity does not follow a preferential direction. Opposed to this, the distortion coming from lensing will have a preferential direction according to the position of the galaxies with respect to the lens. Averaging over many galaxies we can disentangle intrinsic ellipticity and shear.

The observed ellipticity is the sum of the intrinsic ellipticity and the shear (for $\kappa \ll 1$),

$$e_{\rm obs} = e_{\rm int} + \gamma \,, \tag{2.42}$$

which means that, assuming random intrinsic ellipticity orientation and averaging over a

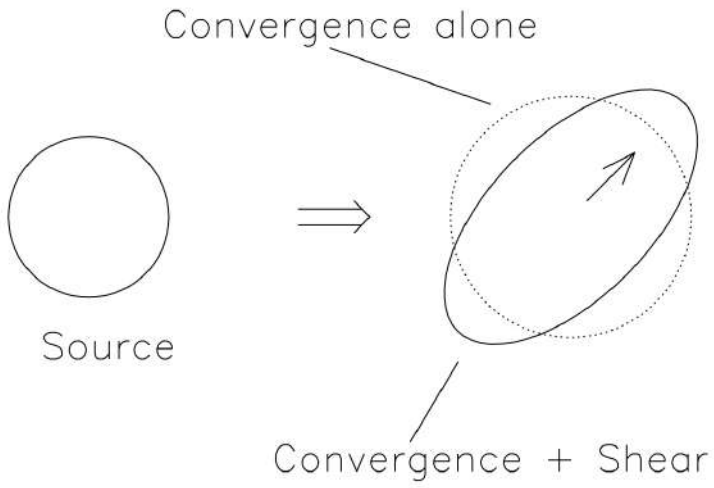

Figure 2.6: Sketch of the convergence and shear distortion. Figure from Narayan & Bartelmann (1996).

large enough number of galaxies we have

$$\left\langle e_{\rm obs} \right\rangle = \langle \gamma \rangle \ , \tag{2.43}$$

since $\left\langle e_{\rm int} \right\rangle = 0$. For more general brightness distributions, the ellipticity can also be defined using the quadrupole moments of the brightness distribution

$$Q_{ij} = \frac{\int \mathrm{d}^2\theta \, q_I\left[I(\boldsymbol{\theta})\right] I(\boldsymbol{\theta}) \, (\theta_i - \bar{\theta}_i) \, (\theta_j - \bar{\theta}_j)}{\int \mathrm{d}^2\theta \, q_I\left[I(\boldsymbol{\theta})\right] I(\boldsymbol{\theta})} \, , \tag{2.44}$$

where $q_I\left[I(\boldsymbol{\theta})\right]$ is a chosen weight function and $\bar{\theta}$ indicates the center of the image, which can be calculated by

$$\bar{\boldsymbol{\theta}} = \frac{\int \mathrm{d}^2\theta \, q_I\left[I(\boldsymbol{\theta})\right] I(\boldsymbol{\theta}) \boldsymbol{\theta}}{\int \mathrm{d}^2\theta \, q_I\left[I(\boldsymbol{\theta})\right] I(\boldsymbol{\theta})} \, . \tag{2.45}$$

We can now define ellipticity depending on the quadrupole moments as

$$e = \frac{Q_{11} - Q_{22} + 2iQ_{12}}{Q_{11} + Q_{22} + 2(Q_{11}Q_{22} - Q_{12}^2)^{1/2}} \, . \tag{2.46}$$

The conversion between the lensed and unlensed ellipticities can be done by using

$$\mathrm{d}^2\beta = \det \mathcal{A} \, \mathrm{d}^2\theta \, , \tag{2.47}$$

$$\boldsymbol{\beta} - \bar{\boldsymbol{\beta}} = \mathcal{A}(\boldsymbol{\theta} - \bar{\boldsymbol{\theta}}) \, . \tag{2.48}$$

2.3.3 Shear estimate method (KSB+)

To determine the mass of an object through WL we need to estimate the distortion caused by the lens in the background galaxies (shear). Several different methods have been developed to measure this shear. There has historically been a distinction between two types of algorithms to measure shear: model-fitting and moment-based algorithms. However, this distinction is not necessarily complete or a strong division. We use the Kaiser-Squires and Broadhurst (KSB) algorithm (Kaiser et al. 1995, Luppino & Kaiser 1997, Hoekstra et al. 1998), which is a moment-based algorithm to determine the shape of galaxies, performing a correction for the Point-Spread Function (PSF) using the stars in the field. New, more modern methods, have been developed for cosmic shear applications which require tighter constrains. However, for our study, we use an extension to the classical KSB, called KSB+, which has been widely used in previous cluster work (e.g S18a). It performs well for our requirements and allows us to compare to what has been done so far in other cluster studies. Details of this particular implementation can be found in Schrabback et al. (2007), Schrabback et al. (2010) (hereafter S10) and Erben et al. (2001) but are also explained here.

This method is based on the measurement of the moments of the galaxy light distribution, applying a correction for the PSF influence. The correction is obtained by measuring the brightness moments of the stars in the same image (or in a starfield obtained with the same PSF).

The ellipticity of each background galaxy is measured individually, using the weighted quadrupole moments Q_{ij} of the light in the form of (which is a rewritten form of Eq. 2.44)

$$Q_{ij} = \frac{\int d^2\boldsymbol{\theta}\, W(\boldsymbol{\theta})\, I(\boldsymbol{\theta})\, \theta_i\, \theta_j}{\int d^2\boldsymbol{\theta}\, W(\boldsymbol{\theta})\, I(\boldsymbol{\theta})}\,, \tag{2.49}$$

where $I(\boldsymbol{\theta})$ is the surface brightness and $W(\boldsymbol{\theta})$ is a weight function which in our case is a Gaussian function with scale length r_g. This scale length can be arbitrarily chosen. We selected it for our analysis as the `SExtractor` (Bertin & Arnouts 1996) FLUX_RADIUS (which approximately maximises the measurement signal-to-noise ratio). Unweighted second moments would not provide accurate results due to photon noise, so instead we use a Gaussian weight function. For our KSB+ implementation, we assume that Q has a zero trace, so we can describe the two polarization parameters e_α as

$$\begin{aligned} e_1 &= \frac{1}{Q_{11}+Q_{22}}(Q_{11}-Q_{22}), \\ e_2 &= \frac{1}{Q_{11}+Q_{22}}(2Q_{12})\,. \end{aligned} \tag{2.50}$$

The two components correspond to the two axis on which the ellipticity is measured. The first component, e_1, is aligned with the direction of the pixel and the second, e_2, is diagonal to the pixel. This will cause an effectively smaller sampling in the first component, which is not critical but has a marginal effect on the results presented later. We can treat these two

components as independent, even though in practice, they could influence each other.

In KSB+, the PSF effects on the ellipticity of a galaxy are approximated as a convolution with a circularly smeared PSF and an anisotropic kernel. This is not fully true for many realistic PSFs, in particular, the HST PSF used in Chapter 3. But it can be used as an approximation (Hoekstra et al. 1998) and we can test how this affects the results using simulations (see Sect. 3.1.7).

We can define p_μ, which characterises the PSF anisotropy contribution, and can only be estimated using the stars. For it, we use the measured ellipticity of stars $e^{*\,\mathrm{obs}}_\alpha$ (hence the overscript *) and obtain

$$p_\mu = (P^{\mathrm{sm}\,*})^{-1}_{\mu\alpha} e^{*\,\mathrm{obs}}_\alpha \,. \tag{2.51}$$

$P^{\mathrm{sm}\,*}$ is the smear polarisability tensor of the stars. In the case of stars, the weight function for the moment computation in Eq. (2.49) is adjusted to match the object size (Hoekstra et al. 1998) and will be computed for different values of the size and later matched to the galaxy as well.

The PSF anisotropy-corrected ellipticity of galaxies can then be defined as

$$e^{\mathrm{cor}}_\alpha = e^{\mathrm{obs}}_\alpha - P^{\mathrm{sm}}_{\alpha\beta} p_\beta \,, \tag{2.52}$$

where $P^{\mathrm{sm}}_{\alpha\beta}$ is the smear polarisability tensor which describes the sensitivity of the galaxy to the smearing caused by the PSF.

Alternatively, we can account for the isotropic effect of the atmosphere and weight function using the intrinsic ellipticity e^{s} and the gravitational shear γ by

$$e^{\mathrm{cor}}_\alpha = e^{\mathrm{s}}_\alpha + P^{g}_{\alpha\beta} \gamma_\beta \,. \tag{2.53}$$

This uses the pre-seeing shear polarisability tensor P^g, defined as

$$P^{g}_{\alpha\beta} = P^{\mathrm{sh}}_{\alpha\beta} - P^{\mathrm{sm}}_{\alpha\mu} (P^{\mathrm{sm}*})^{-1}_{\mu\delta} P^{\mathrm{sh}*}_{\delta\beta} \,, \tag{2.54}$$

where P^{sh} is the shear polarisability tensor from Hoekstra et al. (1998), which measures the response of galaxy ellipticity to shear in the absence of PSF effects, and $P^{\mathrm{sm}*}$ and $P^{\mathrm{sh}*}$ are the stellar smear and shear polarisability tensors, respectively.

Putting everything together, we can now define the fully corrected ellipticity which is our KSB+ shear estimator as:

$$e_\alpha = (P^g)^{-1}_{\alpha\beta} [e^{\mathrm{obs}}_\beta - P^{\mathrm{sm}}_{\alpha\mu} p_\mu] \,. \tag{2.55}$$

When $\kappa \ll 1$, we have:

$$\langle e_\alpha \rangle = g \simeq \gamma \,, \tag{2.56}$$

which allows for the estimation of the shear by averaging the fully corrected galaxy ellipticities.

$g(\boldsymbol{\theta})$ is the reduced gravitational shear, which relates to the shear $\gamma(\boldsymbol{\theta})$ as

$$g(\boldsymbol{\theta}) = \frac{\gamma(\boldsymbol{\theta})}{1 - \kappa(\boldsymbol{\theta})} \,. \tag{2.57}$$

For the cases where $\kappa(\boldsymbol{\theta}) \ll 1$, both are equivalent. In our implementation, we make the approximations

$$(P^g)^{-1} = \frac{2}{\mathrm{Tr}[P^g]}, \tag{2.58}$$

$$\left[(P^{\mathrm{sm}*})^{-1} P^{\mathrm{sh}*}\right] = \frac{\mathrm{Tr}\left[P^{\mathrm{sh}*}\right]}{\mathrm{Tr}\left[P^{\mathrm{sm}*}\right]}, \tag{2.59}$$

to reduce noise following Erben et al. (2001). To find the galaxies in the image we use `SExtractor` object detection, and for the moment measurement the code analyseldac (Erben et al. 2001).

Also following Erben et al. (2001), we define the KSB signal-to-noise ratio as

$$S/N_{\mathrm{KSB}} = \frac{\sum_i W_i \, I_i}{\sigma \sqrt{\sum_i W_i^2}}, \tag{2.60}$$

where we have a sum over the pixels i. W_i is the same weight function used for the moment computation (Eq. 2.49), I_i is the surface brightness, and σ is the sky background dispersion. This indicates how bright our objects are with respect to the noise level of the background. It is however, a particular way of measuring a signal-to-noise ratio for our shear estimator and cannot be easily generalized for other methods. It is useful, nonetheless, to compare to previous work using the same KSB+ method.

We apply similar selection cuts as in S10 for the galaxies which we use when computing the average in our analysis, such as $r_{\mathrm{g}} < 10$. We also require $r_{\mathrm{h}} > 1.2\, r_{\mathrm{h}}^*$, where r_{h} and r_{h}^* are the half-light radius of the galaxies and the stars in the field, respectively, and consider $\mathrm{Tr}\, P^g/2 > 0.1$.

The theoretical derivation of this shear measurement method assumes noise-free data, which is not the situation in real images. This is not a problem for galaxies with high signal-to-noise ratio, but the assumptions break down at low S/N. Because of this, KSB+ is highly affected by the biasing at low signal-to-noise ratio, which was corrected for in S10, reducing the bias. It was computed using the STEP2 simulations (Massey et al. 2007) of ground-based images and also tested for ACS-like simulations. It follows a power law

$$m_{\mathrm{corr}} = -0.078 \left(\frac{S/N_{\mathrm{ksb}}}{2}\right)^{-0.38} \,. \tag{2.61}$$

This correction depends on the KSB+ signal-to-noise ratio which is defined in Eq. (2.60) and we will use it as a base to compute our own correction using the same functional form in

Chapter 3.

We can define weights to perform a weighted average in order to modify the contribution of the ellipticity of each galaxy and how confident we are on its measurement. In particular, we down-weight objects according to their magnitude-dependent RMS ellipticities (S18a). This simple weighting scheme avoids the introduction of artificial biases due to weights which directly depend on the ellipticity.

Using KSB+, we obtain a catalog with the positions, magnitudes, and measured ellipticities of all objects in the image. With it, we can compute the average ellipticity of galaxies with similar shears. This can be done in two ways; for the case of simulations with constant shear values we know the true input values so we can simply select galaxies with the same shear and average over them. This is not so simple for the real images which have a varying shear depending on their position. There we need to find the center of the cluster and tangentially average in radial annuli which should approximately have the same shear value.

2.3.4 Photometric redshift

For measuring the shear caused by a lens, we need to use galaxies situated behind such a lens, since they will be the ones which get affected by the lensing distortions. The inclusion of cluster members and foreground galaxies which are not lensed, dilutes the signal and hence will provide biased mass estimates if not accounted for. This selection of background galaxies requires knowing the redshift of the cluster and the galaxies in our image. Determining their redshift should be done spectroscopically, but that requires long exposures and it is impractical for most cases with large numbers of galaxies. To solve this problem, we can use photometric redshifts which compare the flux of an object in different bands to model predictions and obtain a redshift estimate. Depending on the redshift and the light spectrum of the objects, the magnitude differences between the different bands (called colour) will be different. This is particularly useful for objects with a clear break in their spectra, such as the 4000Å break, which is typically found in galaxies with a metal-rich population of stars and an old stellar population (Kauffmann et al. 2003). This break will cause a sharp change in the flux registered using two filters which bridge the break. Knowing the rest-frame wavelength of the break, we can compare this to the wavelengths we observe it in and estimate a redshift. This effectively means that in the colour-magnitude plane galaxies will have a different colour according to their redshift and we can perform a specific cut and preferentially select background galaxies, removing most of the cluster members and the foreground. An example of this, used in S18a is shown in Fig. 2.7 where we can see that galaxies near the redshifts of our clusters have larger $V - I$ colours. This indicates that a cut on $V - I < 0.3$ will preferentially select background galaxies with a small foreground contamination. The study of which specific cuts select a better sample for the lensing estimates, with a low foreground contamination, depends on the population and the redshift of the cluster.

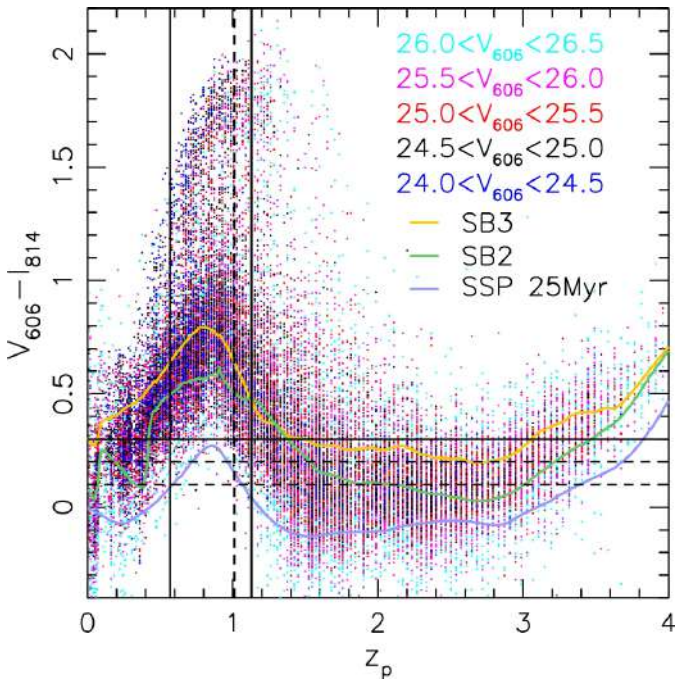

Figure 2.7: Plot of the V-I colour of galaxies in the CANDELS fields as a function of their photometric redshift (from S18a).

2.3.5 Modelling cluster shears

Using the ellipticity catalog of individual background galaxies obtained using the KSB+ algorithm, as explained in Sect. 2.3.3, we can determine the tangential (reduced) shear profile of a cluster. Assuming an NFW model, this allows us to estimate the mass of the lens. The tangential and cross shear are defined from the two shear components as

$$\begin{aligned} g_t &= -(g_1 \cos(2\Phi) + g_2 \sin(2\Phi)) \,, \\ g_x &= -g_1 \sin(2\Phi) + g_2 \cos(2\Phi) \,, \end{aligned} \tag{2.62}$$

with Φ being their angular position with respect to the center. The tangential shear values will depend on the distance to the cluster center, typically being stronger closer to the center. In our analysis we use HST/ACS optical (V_{606}) observations of three relaxed clusters and compute shear profiles using 14 bins with a bin size of 100 kpc each, between 300 kpc and 1.7 Mpc. These scales are selected to avoid miscentering issues or the influence of central substructure on the smallest scales and due to the edges of the image, the lack of proper coverage in all directions at larger scales. When modelling shear profiles we assume that they follow NFW profiles, which depend on M_{200} and the concentration. Assuming e.g. the mass-concentration relation in Diemer & Joyce (2019) we can perform a fit to M_{200} which will provide us with an estimate of the total mass (at r_{200}). Defining $x = r/r_s$, the radial

dependence of the shear is given by

$$\gamma_{\rm NFW}(x) = \begin{cases} \frac{r_{\rm s}\delta_{\rm c}\rho_{\rm c}}{\Sigma_{\rm cr}} g_<(x) & (x<1) \\ \frac{r_{\rm s}\delta_{\rm c}\rho_{\rm c}}{\Sigma_{\rm cr}} \left[\frac{10}{3} + 4\ln\left(\frac{1}{2}\right)\right] & (x=1) \\ \frac{r_{\rm s}\delta_{\rm c}\rho_{\rm c}}{\Sigma_{\rm cr}} g_>(x) & (x>1) \end{cases}, \tag{2.63}$$

(Bartelmann 1996, Wright & Brainerd 2000). The functions $g_{<,>}$ are independent of cosmology and are defined as

$$\begin{aligned} g_<(x) = & \frac{8\,\mathrm{arctanh}\sqrt{\frac{1-x}{1+x}}}{x^2\sqrt{1-x^2}} + \frac{4}{x^2}\ln\left(\frac{x}{2}\right) - \frac{2}{x^2-1} + \frac{4\,\mathrm{arctanh}\sqrt{\frac{1-x}{1+x}}}{(x^2-1)(1-x^2)^{1/2}}, \\ g_>(x) = & \frac{8\arctan\sqrt{\frac{x-1}{1+x}}}{x^2\sqrt{x^2-1}} + \frac{4}{x^2}\ln\left(\frac{x}{2}\right) - \frac{2}{x^2-1} + \frac{4\arctan\sqrt{\frac{x-1}{1+x}}}{(x^2-1)^{3/2}}. \end{aligned} \tag{2.64}$$

Since Eq. (2.64) only depends on x, which is the normalized radius, we can fit Eq. (2.63) in radial bins and the only free parameter will be the mass (since we assume a mass-concentration relation). Considering that $\Sigma_{\rm cr}$, which is defined in Eq. (2.31), depends on the distances, we need to estimate this value for each galaxy. If we define the geometric lensing efficiency β as

$$\beta(z_i) = \frac{D_{\rm LS}}{D_{\rm S}}, \tag{2.65}$$

then $\Sigma_{\rm cr}$ will depend on it. β will be different for each galaxy as it depends on its distances with respect to the lens and to us. We can then define the shear and the convergence as a function of β

$$\gamma = \beta_{\rm s}(z_i)\gamma_\infty, \tag{2.66}$$
$$\kappa = \beta_{\rm s}(z_i)\kappa_\infty, \tag{2.67}$$

where we define the values of the convergence and the shear for a source at infinite redshift and $\beta_{\rm s}(z_i) = \beta(z_i)/\beta_\infty$. However, we do not know the distances of all sources and that means we do not compute β individually for all galaxies. Instead, we only obtain the average of this quantity for an ensemble of galaxies. For this, we can compute

$$\langle\beta_s\rangle = \frac{\sum \beta_s(z_i) w_i}{\sum w_i}, \tag{2.68}$$

$$\langle\beta_s^2\rangle = \frac{\sum \beta_s^2(z_i) w_i}{\sum w_i}, \tag{2.69}$$

which are weighted by the shape weights $w_i = 1/\sigma_{e,i}$. Here, $\sigma_{e,i}$ is the dispersion of the galaxy ellipticity and includes the contributions both from the measurement noise and the

intrinsic shape distribution. Using the average β effectively causes an overestimation of the shear since we obtain the average lensing distortion as

$$\langle g \rangle = \frac{\langle \beta_s \rangle \gamma_\infty}{1 - \langle \beta_s \rangle \kappa_\infty}\,, \tag{2.70}$$

rather than

$$\langle g \rangle = \left\langle \frac{\beta_s \gamma_\infty}{1 - \beta_s \kappa_\infty} \right\rangle. \tag{2.71}$$

In order to correct for this, we need to include a factor derived in Hoekstra et al. (2000) (and used in S18a) which is

$$g_{\rm correction} = 1 + \left(\frac{\langle \beta_s^2 \rangle}{\langle \beta_s \rangle^2} - 1 \right) \kappa\,. \tag{2.72}$$

A 3D mass reconstruction can also be done where we can see the inner structure of the mass distribution, rather than the total mass inside a certain radius. This is not done in the work so no further details are included here.

Issues in mass estimations

Here we mention some of the issues that need to be considered when trying to find the mass of clusters.

In order to obtain good mass estimates, we require a robust estimation of the source and lens redshift distributions which can be done through photo-z on the images or in our case using the CANDELS fields. A detailed analysis of the influence of inaccuracies on these estimates can be seen in Raihan et al. (2020). Accurate photometry is needed to remove the cluster members and as much of the foreground as possible since those galaxies will dilute the lensing signal and reduce the amplitude of the profile, leading to a smaller mass estimate. The different populations towards the center and the outskirts of clusters can also lead to a different fraction of cluster members present in those areas of the analysis and hence a flattening of the mass profile. For this, an accurate photometric redshift estimate is key. Removal of these cluster members is not as important as having a way to characterize any remaining contamination and include them in the calculation of β.

We also need to select the correct center when we fit the shear profile, which is not trivial. The cluster centers can be defined as the peaks of the density distributions, but they will vary according to what observations we are using. In relaxed clusters the SZ-, X-ray- and WL-determined centers will be very close to each other so it is not a main source of uncertainty for this work. This can be different a different scenario for other types of clusters. The estimates presented in this work are obtained using the X-ray center.

Furthermore, we have the issue of the mass projection: we cannot directly observe the 3D mass distribution, unless we have the knowledge of the redshift of all galaxies. The only available observation is the projected mass in a cylinder of a certain radius, not a sphere. However, knowing the redshift of the galaxies partially helps.

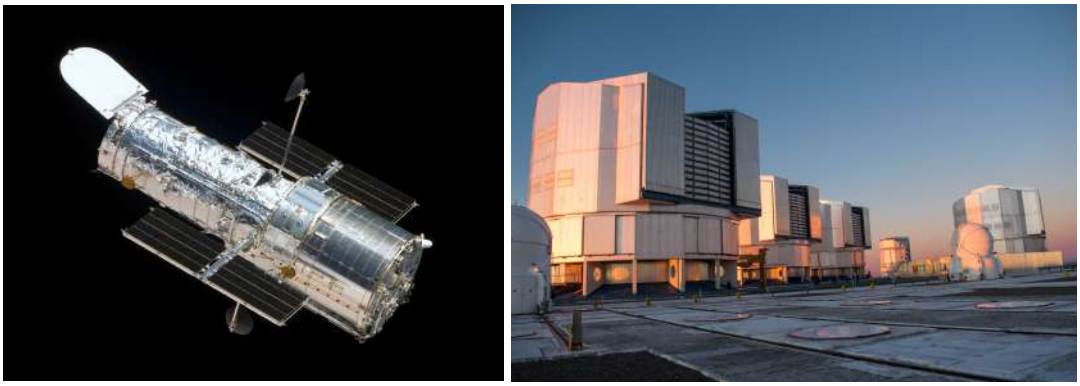

Figure 2.8: *Left*: Image of the Hubble Space Telescope taken during the 2009 servicing mission. Credits: NASA. *Right*: The 4 VLT telescopes at Cerro Paranal (Chile), hosting FORS2 in one of the telescopes (UT1) and HAWK-I in another (UT4). Credit: B. Hernandez-Martin.

2.4 Observational basics

In this work, we use real images from different telescopes, as well as simulated images, which try to reflect the real properties of the images as closely as possible. For this, a brief introduction to important concepts of the observations of galaxy clusters in the optical bands is needed.

The images used to study galaxy clusters through WL normally require two things: deep observations to obtain enough signal-to-noise ratios for galaxies further from us than the cluster, and sufficiently resolved images to allow the study of shapes of such galaxies. For this, the ideal candidate is the Hubble Space Telescope (HST), which due to its placement outside of our atmosphere, provides very sharp images. However, the use of this telescope is normally very expensive and only a few orbits can be obtained for each cluster. It is for this reason that alternatives using ground-based telescopes are also used.

To accurately select the background galaxies and properly remove cluster members, we need to do a colour selection. For this, complementary ground-based images are normally used. In our case, for the clusters in Sect. 5, we performed a $V - I$ colour selection using HST/ACS (pictured in Fig. 2.8) images for the V-band (F606W) for shapes and additional HST/ACS I-band (F814W) or VLT/FORS2 I-band for the colour selection. If HST observations are not available, measurements can also be attempted using best-seeing ground-based images, leading however to a smaller fraction of sufficiently resolved galaxies for weak lensing shape measurements. In the case of Sect. 4.2, we mimick images from the Subaru/Hyper Supreme-Cam (image in Fig. 2.9) for both shape determination and colour selection. For clusters which are further away, we can also use images obtained in the near-infrared, using the VLT/HAWK-I camera (telescope pictured also in Fig. 2.8). In this case, discussed in Sect. 4.1, the images will be sharper due to the lower interference of the atmosphere at these wavelengths.

Several concepts worth mentioning here which are important in observations are:

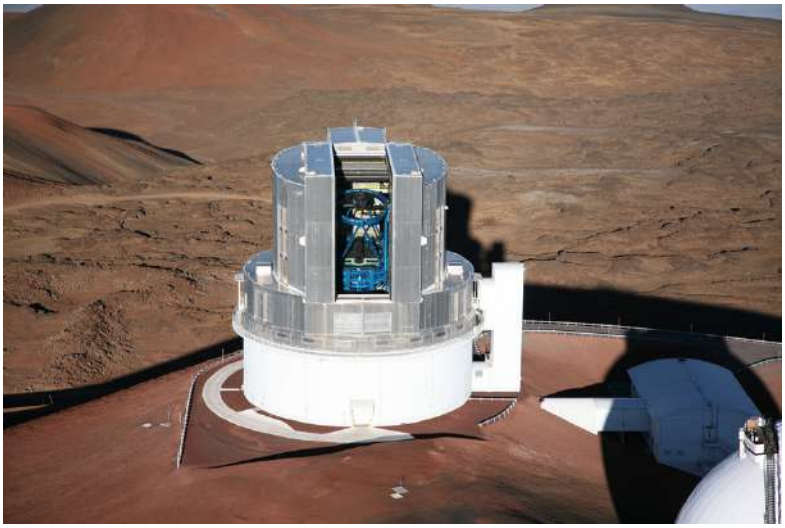

Figure 2.9: Image of the Subaru telescope in Mauna Kea (Hawaii, USA). Courtesy of NAOJ.

- CCD's: The use of Charged Coupled Devices (CCD's) has been one of the major advances of modern astronomy. It is based on the photoelectric effect, gathering the electrons in potential wells, called pixels which then are converted to a digital signal, using the Analog-Digital Unit (ADU).

- Pixel scale: Depending on the optical setup, pixels in each particular CCD will cover a different area on the sky. The number of arcseconds that corresponds to one pixel is the pixel scale of that detector.

- Point-Spread Function (PSF): Objects in the sky are observed through the atmosphere and the optical system, which causes certain distortions. Point-like sources, like stars, should only cover one pixel under perfect resolution, but they appear in the images as a smeared profile. We can approximate it with a Gaussian or a Moffat profile[1] in many cases and we can use the stars to model it. An indication of how big this effect is, is given by the Full-Width at Half Maximum (FWHM) of the profile. The use of space-based images will reduce the FWHM of the PSF due to the lack of atmospheric distortions. The seeing is the FWHM of the PSF in the V-band that indicates how the sky conditions were at the moment of the observations.

- Magnitudes: Astronomers use magnitudes as a measure of brightness. It is a logarithmic scale which requires a reference flux. In this work, we use the AB magnitude system, which follows

$$m_{\mathrm{AB}} = -2.5 \log_{10} \left(\frac{f}{3631\,\mathrm{Jy}} \right), \tag{2.73}$$

[1] The Moffat profile for a radius r has two parameters α and β and follows: $f(r, \alpha, \beta) = 2\frac{\beta-1}{\alpha^2} \left[1 + \frac{r^2}{\alpha^2}\right]^{-\beta}$

where f is the flux of the object, and $1\text{Jy} = 10^{-26}\text{W Hz}^{-1}\text{m}^{-2} = 10^{-23}\text{erg s}^{-1}\text{Hz}^{-1}\text{cm}^{-2}$

- Parsecs (pc): They are distance units, used in astrophysics. $1\text{pc} = 3.26\,\text{ly} = 3.0857 \cdot 10^{16}\text{m}$.

2.5 Calibrating shear estimates with simulations

The main part of this work deals with the creation of simulations of the background population of galaxies to calibrate the KSB+ algorithm. Any shear measurement method needs to be calibrated through simulations to test for differences between the input and the recovered shear that might be present. Correcting for the bias that arises is the only way to obtain trustworthy shear measurements and mass estimates.

Knowing the input shear (g^{true}) in our simulations we can run our pipeline and compare it to the recovered values (g^{obs}) assuming the relation

$$g^{\text{obs}} = (1 + m)\, g^{\text{true}} + c\,. \tag{2.74}$$

This linear relation has been extensively used in the literature (e.g. Heymans et al. 2006, Applegate et al. 2014, Fenech Conti et al. 2017). Alternatively we also tested a quadratic dependence, which was found to be negligible even for the stronger regimes used in this work. In the case of cosmic shear the additive bias (c) is important, but for cluster analyses it cancels out to leading order for the azimuthally-averaged tangential shear profiles. In Chapter 3 and 4 we will therefore mostly concentrate the analysis in the multiplicative bias (m), which is the most relevant for cluster analysis. An alternative signal-to-noise ratio to S/N_{KSB} (Eq. 2.60) can be defined using `SExtractor` parameters. This definition is more widely used since it does not depend of the particulars of the shape measurement implementation:

$$S/N_{\text{flux}} = \frac{\text{FLUX\_AUTO}}{\text{FLUX\_AUTO\_ERR}}. \tag{2.75}$$

We used this definition primarily to perform signal-to-noise cuts on the galaxies and to allow for a wider comparison with other weak lensing methods. The signal-to-noise ratio definition S/N_{KSB} in Eq. (2.60) is used for internal calibrations.

We create customized simulations matched for each camera and telescope setup, which also allow us to test cluster specific issues such as stronger shears ($|g| < 0.4$) and increased blending (Sect. 3.2). We simulate images from different telescopes by changing the input parameters in our simulations that correspond to the telescope properties, in particular the pixel scale and the PSF model. The properties of the mock galaxies also need to be modified according to the population of galaxies as observed by each telescope and for each science objective, which can be drastically different. This means that we need to tune the magnitudes, sizes, light profiles and ellipticities of our mock galaxies. An example cut-out of a simulated image can be seen in Fig. 2.10, where the galaxies are placed on a grid for the setup in Chapter 3. They each have a random intrinsic ellipticity following a choice of distributions. They

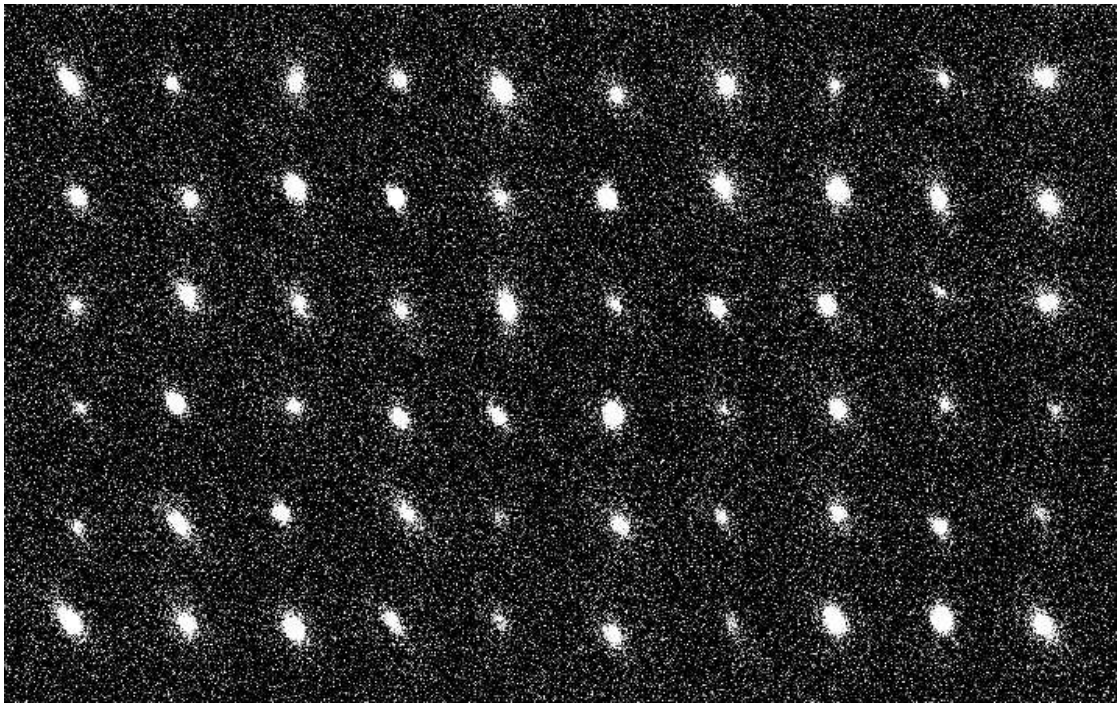

Figure 2.10: Cut-out of a simulation image.

have been sheared with the same value in each image, convolved with the PSF and have a low Gaussian noise added. An interesting problem that we investigate extensively in this work is the question of how sensitive the results are to the choices we make in the creation of the simulations. It is important to understand how a choice regarding the inputs changes the bias (see Chapter 3), and how realistic our choices are.

The simulations were created with the python package `GALSIM`[2] (Rowe et al. 2015), which was specifically created for simulations of galaxies including the influence from weak lensing. `GALSIM` provides the option to create a simple galaxy by assuming a Sersic brightness profile with a specified Sersic index and size:

$$I(R) = I_e \exp\left(-b_n[(R/R_e)^{1/n} - 1]\right), \tag{2.76}$$

with the half-light radius R_e, the intensity at that radius I_e and the parameter $b_n \approx 2n - 1/3$ with n being the so-called Sersic index. `GALSIM` has multiple options for the simulation creation, including the use of a real image catalog from COSMOS (Scoville et al. 2007). For most of our simulations (except Sect. 4.2) we employ parametric fits to these galaxy images, which can then be used as input for the Sersic index and the ellipticity of our simulated galaxies. This allows us to employ a more realistic input shape distribution for the creation of our galaxies than selecting all of them as a De Vaucouleurs ($n = 4$) or exponential ($n = 1$)

[2] `https://github.com/GalSim-developers/GalSim`

galaxy type. The influence of this choice is tested in Sect. 3.1.5. The input distributions that were used do not exactly match the distributions that we obtain when we measure the galaxy properties on the final mock images, due to the PSF convolution and pixelation. For this reason, we can only compare measured distributions of the mock galaxies with the real galaxies, which can help us understand how "realistic" our simulations are. In Sect. 4.2, for the Hyper Suprime-Cam simulations, we use real images from COSMOS directly as input, which removes the need to assume the input distributions of the parameters. The magnitude, signal-to-noise ratio and size distribution of the mock galaxies in each telescope setup is compared to real observations with the depth and colour selection used for the real weak lensing analysis. We aim to have similar distributions between real and mock galaxies. Small discrepancies can be due to the fact that the S/N, magnitude and size distributions depend on each other and are correlated. For example, bright galaxies will normally be larger and with a higher S/N, but we draw from the magnitude and size distributions independently and this can introduce small differences between the real and mock galaxies. Kannawadi et al. (2019) found that the correlation of input distributions can be quite important. However, they also found that for higher redshift galaxies, such as the subject of this work, it is not as critical.

The simulated galaxy can then be rotated, sheared or otherwise transformed. We shear our synthetic galaxies and convolve them with a simulated PSF. This emulates the final image of the galaxy as it would look in the real images. The PSF can be either an analytical function (i.e. Gaussian or Moffat profiles) or an image which captures further irregularities in the PSF. We add random Gaussian noise at a level that allows us to match the S/N distributions of the mock and real galaxies. Our synthetic galaxies were placed on a grid for most of this work, as was done in previous studies (e.g. GREAT3 challenge in Mandelbaum et al. 2014) to avoid contamination from neighbours or blending effects. This is not the most realistic scenario but allows us to study the bias from unblended and isolated galaxies. In order to study a more realistic scenario where galaxies are not isolated, we created simulations with varying shear, following the real cluster situation in Sect. 3.2 and with the positions and magnitudes of real catalogs in Sect. 3.3.

To compute the bias, galaxies are grouped with the same input shear which means the average of all galaxy ellipticities in that group of galaxies should suppress the noise caused by the intrinsic ellipticities and provide an estimate of their shear. This allows us to measure the bias from the discrepancy between the input and the measured shear. In order to further reduce shape noise we created a second set of galaxies, which are identical except for a 90 degree rotation of the input intrinsic ellipticity (Massey et al. 2007). The profile of each galaxy is created and rotated before adding the shear. The resulting image pairs will have the same shear but rotated intrinsic ellipticities. This makes sure that the mean intrinsic ellipticity of the input population is 0. For our purposes, it is sufficient to just use pairs, but multiple copies of the galaxies, rotated by 45 degrees have been used in other works (e.g. Fenech Conti et al. 2017). In our case, due to the faintness of the galaxies, the noise is dominating and the inclusion of further rotated simulations does not lead to a significant improvement, which is why we chose to only implement pairs. In general, we require that galaxies in both simulation pairs are detected in order to be used in the analysis as this is what reduces the noise. However, this also means that we do not include any selection bias in

our bias estimates. Selection bias is the preferential selection of galaxies in our analysis due to their shape. This means that we do not effectively have a homogeneous sample and some of the measured bias comes from the intrinsic ellipticity of the galaxies that are detected and not from the shear measurement itself. In Sect. 3.3.1, we study this effect and we include it in the final bias estimates for all telescopes by not requiring the matched galaxy pairs.

Once these simulations are created, they are run through the same pipeline used for the real images in order to obtain catalogs with their ellipticity. We can then compare their behaviour and better understand not only our algorithm and pipeline, but also the impact of the choices we made when creating the mock images.

CHAPTER 3

HST/ACS-like simulations

Creating simulated images of galaxies which resemble the real images is a challenging task. Reproducing the observed galaxies requires careful consideration of the distortions caused by the light travelling through the Universe, and interacting with the telescope optics. The intrinsic values of the galaxy properties, such as their size or ellipticity, are unknown as we can only recover the observed properties. We do not have an exact idea of how the galaxies actually look like and the best we can do is use very deep observations to try and estimate their intrinsic properties as accurately as possible. For this reason, simulations are a very useful tool for the understanding of how our methods behave, as we know the intrinsic properties of simulated galaxies and we can see how small changes affect the weak lensing analysis.

Weak lensing mass estimates of clusters found with the 2,500 deg^2 SPT-SZ Survey (Bleem et al. 2015) have already shown to provide successful results (S18a, Bocquet et al. 2019, Schrabback et al. in prep., hereafter known as S20). These large samples at different redshifts are very valuable in order to have a better general understanding of clusters. However, this also increases the need to better control the systematic of our methods as the statistical uncertainties are getting smaller. Earlier related work, aimed to calibrate the shear measurement algorithm, using a bias correction dependent on the signal-to-noise ratio of the galaxies (presented in Eq. 2.61) which was obtained in S10 and has been used for the mass estimates of clusters in HST/ACS in S18a. This correction was computed using modified ground-based simulations which can have a substantially different bias to sky-based observations with HST/ACS. To further understand and control the systematics in the KSB+ method used for our mass determination, we created new sets of simulations which are presented in this work. The aims of creating these specific ACS-like simulations are:
1. Obtaining an updated signal-to-noise dependent correction that can further reduce the remaining multiplicative bias and allow us to obtain more accurate mass estimates.
2. Testing how the algorithm behaves with larger values of the shear, since most previous work was based on $|g| < 0.1$.
3. Understanding the limits of simulated images and the influence that the assumptions we made have in the bias determination.

4. Studying the effect of neighbours, blends and cluster galaxy members on the estimated bias.

In this chapter we start by presenting a simplified setup with isolated galaxies on a grid. This allows us to understand the impact that the choices made for the creation of the simulations have in the bias. In the following sections, more realistic situations are introduced. In Sect. 3.2, we study the impact of the cluster members on the shear estimation of the source background galaxies used to estimate the cluster mass. In Sect. 3.3, a more realistic simulation is created, using real catalogues as inputs for the magnitudes and positions. This better reflects the real scenario and allows us to study the impact that neighbours have in the multiplicative bias. Furthermore, we looked at the selection bias which can also have a large effect. In order to fully account for the influence of faint undetected galaxies, we also compared the results with a similar setup which follows the work of Euclid Collaboration et al. (2019) and accounts or the full impact of faint galaxies in simulations. With all these ingredients we obtain a signal-to-noise dependent correction and a final estimation of the multiplicative bias.

3.1 Galaxies on a grid

In this section we present the results from simulated galaxies placed on a grid. This is useful to obtain bias estimates from isolated galaxies and understand how the choices on the galaxy properties modify the bias. We begin here by briefly explaining the creation of the grid 'reference' simulation and summarizing the simulation settings (see Table 3.1). More detailed information on the particular input choices is presented in the following subsections, where we vary some of the input parameters one at a time in order to investigate the sensitivities of our analysis to modelling details. Understanding the shortcomings and limits of our simulations is as important as obtaining a final value of the bias since it will provide us with valuable information about the behaviour of our algorithm. It also allows us to measure the robustness of the results by looking at how it behaves when slightly varying the input in the simulations, which allows for a more realistic estimation of the error budget. The aim of this section is to understand the main simulation parameters that change the bias estimation and restrict it to a tolerance level of around 1%. Here, we use a grid placement for our galaxies in order to speed up the computation, to test how the input choices alone (without the impact of neighbours) affect the bias and for easier comparison to previous work. A more realistic approach, where we look at the effect of neighbours and selection bias is used in the next sections, obtaining the final correction and residual multiplicative bias used for the weak lensing mass determination on the more realistic simulations in Sect. 3.4. This section focuses on the impact the input choices have on the bias rather than obtaining a proper correction for the shear measurement.

We simulate HST/ACS F606W images of background galaxies which are affected by the shear coming from a foreground galaxy cluster. The mock galaxies are created to have similar properties to the colour-selected galaxies used for the real cluster analysis in S18a. The simulations were created using the python package `GALSIM` following the process that was

Table 3.1: Summary of the input parameters used for the creation of the mock galaxies of the reference simulation. * Drawn from parametric fits to individual COSMOS galaxies.

Parameter	Type	Values
PSF model	HST/ACS-like	FWHM= $0\farcs1$
PSF ellipticity	HST/ACS-like	$\|e\| = 0.072$
Noise	Gaussian	$\sigma = 0.14\, e^-/\mathrm{s}$
Light distribution	Parametric fit to COSMOS*	Sersic index: 0.3 – 6
Ellipticity distribution	Parametric fit to COSMOS*	$\|\epsilon\| = 0 - 1$
Half-light radius	Fit to CANDELS	$0\farcs05 - 0\farcs3$
Magnitudes	Fit to CANDELS	21.7 – 28.1
Pixel scale	HST-like	$0\farcs05$/pixel

explained in Sect. 2.5. In order to mimic the real observations as closely as possible, we try to reproduce the basic properties of the telescope. This includes an ACS-like pixel scale of $0\farcs05$ /pix and the presence of Gaussian noise. In order to reduce shape noise we created a second set of galaxies, which are identical except for a 90 degree rotation of the input intrinsic ellipticity, as explained before, allowing us to constrain multiplicative biases to the few $\times 10^{-3}$ level. We created 50 pairs of simulated images with 10^4 galaxies with a constant input shear value. In this part of the analysis we only consider galaxies that provide shape estimates in both the normal and the rotated frame. By doing this, we effectively cancel the effects of selection bias, which can be quite important (Kannawadi et al. 2019). In this section, however, we concern ourselves only with the changes in the residual bias estimates due to the input choices for the creation of the simulations and using matched rotated pairs reduces the number of galaxies needed. Our study of selection biases will be presented in Sect. 3.3.1.

We created a grid of 100×100 stamps of size 100×100 pixels and applied a random shift with a uniform distribution from -0.5 to 0.5 at the sub-pixel level for the galaxy position to have a small displacement with respect to the pixel center. This will make sure that the galaxies are not always placed in the exact center of the pixel, which would not be the case for real galaxies and could introduce artificial biases.

The light profile used to create the galaxies is one of the key choices to create a realistic population of mock galaxies and can greatly influence the results. We created the galaxies following a Sérsic profile. This was already described in Sect. 2.5, with the formal expression for the Sérsic profile in Eq. (2.76). The selection of the values of Sérsic index for each galaxy is not trivial as it can produce very different bias if naive choices are made. We used parametric fits to real COSMOS galaxies in order to estimate the Sérsic index and ellipticity of the real galaxies. These catalogues are available inside of `GALSIM`. A more detailed discussion is found in Sect. 3.1.5. The main shortcoming of this approach is that the COSMOS catalogues are observed in a different filter (F814W instead of F606W which we are mimicking here), and with slightly brighter magnitudes (F814W$<$ 25.2). This can introduce slight discrepancies, but they are only marginal (see Sect. 3.1.5 for a detailed

discussion). These COSMOS catalogues were also used to determine the input ellipticity of our galaxies. The size distribution was originally computed from the COSMOS parametric fits as well. However, we found that due to the differences between the catalogue population and our source sample, sizes were larger in average. For this reason, we decided to use the CANDELS catalogues analysed with KSB+ as our input distribution for sizes. We measured the half-light radius distribution in the real catalogues and drew randomly from there for each of our mock galaxies. This means that we have independent distributions in magnitude, size and ellipticity for our mocks. Kannawadi et al. (2019) showed that the inclusion of correlation between input parameter distributions (which we do not include here) can change the shape estimates. Nevertheless, this is expected to not be as important in this work, as we have higher resolution data and use higher redshift galaxies, for which they show to have a lesser impact.

Another critical ingredient is the use of the correct PSF model which resembles the observed PSF. The most realistic model for the ACS-like PSF is obtained from the software `Tiny Tim` (Krist et al. 2011) which is discussed in more detail in Sect. 3.1.7. PSF models obtained from `Tiny Tim` have been successfully used in several papers for different astrophysical applications which use HST/ACS images such as Schroeder & Golimowski (1996), Falomo et al. (2000), Caraveo et al. (2001) and more. A modification to the parameters in the `Tiny Tim` model in Gillis et al. (in prep) was also applied in the creation of the PSF image. More details about the particulars of the PSF are presented in Sect. 3.1.7.

The simulations should aim to resemble the real galaxies as closely as possible to make sure that we are not introducing any artificial bias due to our choice of input parameters. In order to achieve this, we compared our measured distributions of the signal-to-noise ratio, size and magnitude with the ones obtained using data from the Cosmic Assembly Near-IR Deep Extragalactic Legacy Survey (CANDELS) fields (Grogin et al. 2011, Koekemoer et al. 2011) as analysed by S18a (see Fig. 3.1). In particular, we employ catalogues from S18a, which are based on ACS F606W stacks that approximately match the depth of our cluster field observations. S18a applied the same selection to these catalogues as to the cluster field observations in terms of galaxy shape parameters, magnitudes, signal-to-noise ratios and colours. Importantly, their colour selection was tuned to provide a robust cluster member removal, selecting mostly background galaxies at $z \gtrsim 1.4$. By matching the measured source properties of these catalogues with our simulations we therefore make sure to adequately resemble the source properties in the cluster field WL data. From these catalogues we estimate the magnitude of our input galaxies. For the calibration of the magnitude in our simulations, we used the magnitudes (MAG_AUTO key from `SExtractor`) in the F606W band CANDELS catalogues as reference. We then used these values to determine the magnitudes in our simulations, allowing us a direct comparison of the magnitudes between our simulations and the real images.

In order to achieve realistic galaxies, it is important to make sure we are implementing input parameter distributions which are comparable to the ones in the real data we use in the cluster studies for the galaxy size, magnitude and signal-to-noise ratios. Our population needs to resemble the real galaxies used in the mass determination analysis as closely as possible to make sure that we are not introducing any artificial bias due to our choice of

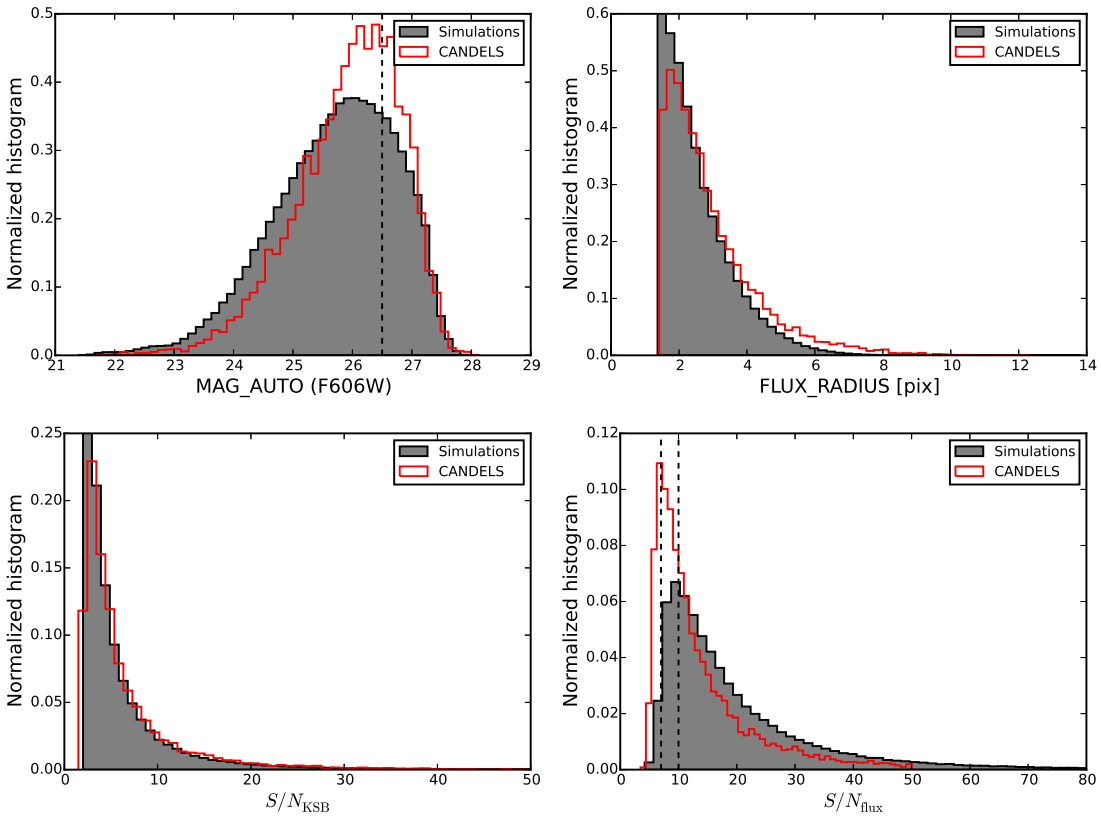

Figure 3.1: Comparisons between the measured distributions in our simulations and the CANDELS distribution for the F606W magnitudes, the flux radius, the KSB+ signal-to-noise ratio $S/N_{\rm KSB}$, and the `SExtractor` signal-to-noise ratio $S/N_{\rm flux}$.

input parameters. For this reason, we compared our measured signal-to-noise ratios, size and magnitude distributions with the ones obtained using the CANDELS catalogues. By matching the measured source properties of these catalogues with the observed properties of the galaxies in our simulations we therefore make sure to adequately resemble the source properties in our cluster field weak lensing data and are confident our corrections can be applied to the real observations. We should note that the noise level was adjusted to match the S/N distributions in the real data.

The comparison of real and mock catalogues is done at the end of our pipeline. This means that we compare our output measured half-light radius, magnitude, and signal-to-noise ratios distributions with the measured parameters in the real catalogues. This is the reason why we estimate the input parameters from CANDELS, and the COSMOS parametric fits. We should note that the input COSMOS catalogues used here are not as deep as our simulations, so the input galaxies are brighter than the galaxies we aim to simulate. Ideally, however, we should use even deeper catalogues that can more robustly represent the input parameters. This is an important issue in our case that does not appear as predominantly in simulations

of ground-based data (e.g. Kannawadi et al. 2019) which can use HST/ACS data as a fair representation of the input properties. Fortunately, since we modified the inputs slightly to match the CANDELS catalogues which have approximately the same depth as our real cluster catalogues this should not be a problem.

We compare the measured distributions for the galaxies in CANDELS and the simulations in Fig. 3.1. The resulting distributions in $S/N_{\rm KSB}$ and half-light radius are well matched but our simulations contain a slightly lower fraction of faint ($26 \leq$ MAG_AUTO ≤ 27) galaxies with a signal-to-noise ratio defined from the `SExtractor` parameters (defined in Eq. 2.75) $S/N_{\rm flux} < 10$. We expect that this slight mismatch is caused by incompleteness as we used the CANDELS magnitude distribution (which itself is incomplete) as an input. However, at faint magnitudes our simulation analysis recovers only an incomplete fraction of galaxies, causing the discrepancy. Nonetheless, these small differences between distributions do not critically impact the obtained bias. This was tested with a reweighting scheme by increasing the importance of those galaxies whose properties are underrepresented in our simulations when comparing to the real CANDELS catalogues. The opposite is true for galaxies which are overrepresented as they are assigned a lower weight. This gives a rough estimate of the importance of the small discrepancies in the matching between mock and real galaxies and gives us confidence on the results, making sure no artificial bias is added because of this. We obtained differences at a negligible level only ($\leq 0.3\%$), which indicates that the small discrepancies that can be seen in Fig. 3.1 are not critical for our work.

We included uncorrelated Gaussian noise, where the level is tuned to provide a good match in the measured $S/N_{\rm KSB}$ distributions between CANDELS and the simulations. Our simple assumptions regarding the noise plus the slight underrepresentation (overrepresentation) of galaxies with faint measured magnitudes (small measured half-light radii) in the simulation (see the top panels of Fig. 3.1) may be the reason for the lack of low $S/N_{\rm flux}$ galaxies seen in the lower right panel of Fig. 3.1.

We draw from independent magnitude and size distributions, which means we do not fully capture the correlation between galaxy parameters. The importance of these correlations was discussed in Kannawadi et al. (2019), who put emphasis on simulating galaxies with joint distributions. This is not as important in our analysis as we do not perform tomographic cuts and always average over our full population. Also, Kannawadi et al. (2019) show that it is especially important to account for such correlations for lower redshift sources, but that the impact becomes small for their highest redshift sources bin, which is the closest to the galaxies we are simulating. We suspect that this redshift dependence is caused by the fact that a broad range of different morphological types contribute to lower redshift source samples, while the highest-redshift sources are largely dominated by star-forming late-type galaxies.

All the particular information of the choices used for the inputs are targeting the creation of HST/ACS mock data and would be different for other setups. In Chapter 4, different input distributions, PSF models and comparison catalogues are used in order to mimic different population of galaxies as viewed by the VLT/HAWK-I and the Subaru/HSC instruments.

3.1.1 Updated $S/N_{\rm KSB}$ dependent correction

S10 established that the multiplicative bias of our KSB+ implementation shows a strong dependence on $S/N_{\rm KSB}$. This should be compensated for using a $S/N_{\rm KSB}$-dependent correction in order to weaken the requirements on how well the simulations have to match the real data. To compute this correction, S10 used the STEP 2 simulations of ground-based weak lensing data (Massey et al. 2007) which were not targeting the same galaxy population that we have in HST/ACS cluster images. This can likely affect the measured correction. We do a similar exercise here, but obtaining the correction with the more realistic HST/ACS simulations. We plotted the recovered bias in 20 $S/N_{\rm KSB}$ bins which all have the same number of galaxies in Fig. 3.2. This allows us to judge how well the correction matches and if there is a need for the computation of an updated correction. Indeed, Fig. 3.2 shows that our analysis of HST-like simulations with background-selected isolated galaxies yields a steeper dependence on $S/N_{\rm KSB}$, which is not well described by the S10 correction. In fact, using the correction from S10 we obtain a $\sim -0.0221 \pm 0.0042$ residual bias. They are particularly different at low signal-to-noise ratios where our simulations suffer from almost double the bias that the correction indicates. In our simulations the source property distribution is radically different to the simulated galaxies in STEP 2 which likely explains this difference in the dependency and justifies the need to obtain a new correction based on our more realistic HST-like simulations. We compute a correction on the simulations with isolated galaxies to use in this section, allowing us to reduce the residual multiplicative bias and facilitate the comparison between different setups. This correction needs to be tested in the more realistic simulations in Sect. 3.3 to see if it can be used in the real analysis of clusters.

To compute an updated correction we assumed, for simplicity, the same functional form as in S10, which seems to behave well according to the measured signal-to-noise. We performed a power-law fit to the binned measured bias to obtain the correction. The galaxies used to compute the bias here do not have any previous corrections applied. We obtained the following correction which will be used in the rest of this section:

$$\begin{aligned} m_{1\rm corr} &= -0.358 \left(S/N_{\rm KSB}\right)^{-1.145} , \\ m_{2\rm corr} &= -0.357 \left(S/N_{\rm KSB}\right)^{-1.298} . \end{aligned} \tag{3.1}$$

We computed the correction separately for each component of the shear. One single correction could be used for both, but as can be gathered from Eq. (3.1), the differences between the two components are small but are not necessarily negligible. For this reason, we decided to take the approach of analysing them separately. In Fig. 3.2 we overplot the new correction for both components, showing that it provides a much better match to the simulations than the old correction from S10. Our new correction is a steeper power law which better reflects the larger bias obtained at small $S/N_{\rm KSB}$.

The main conclusion we can draw from the differences between both corrections is that a better understanding of the bias dependencies will provide a better correction which will reduce the residual overall bias. But, going even further, it can also allow us to use fainter galaxies (which have less signal-to-noise ratios in the weak lensing analysis) and

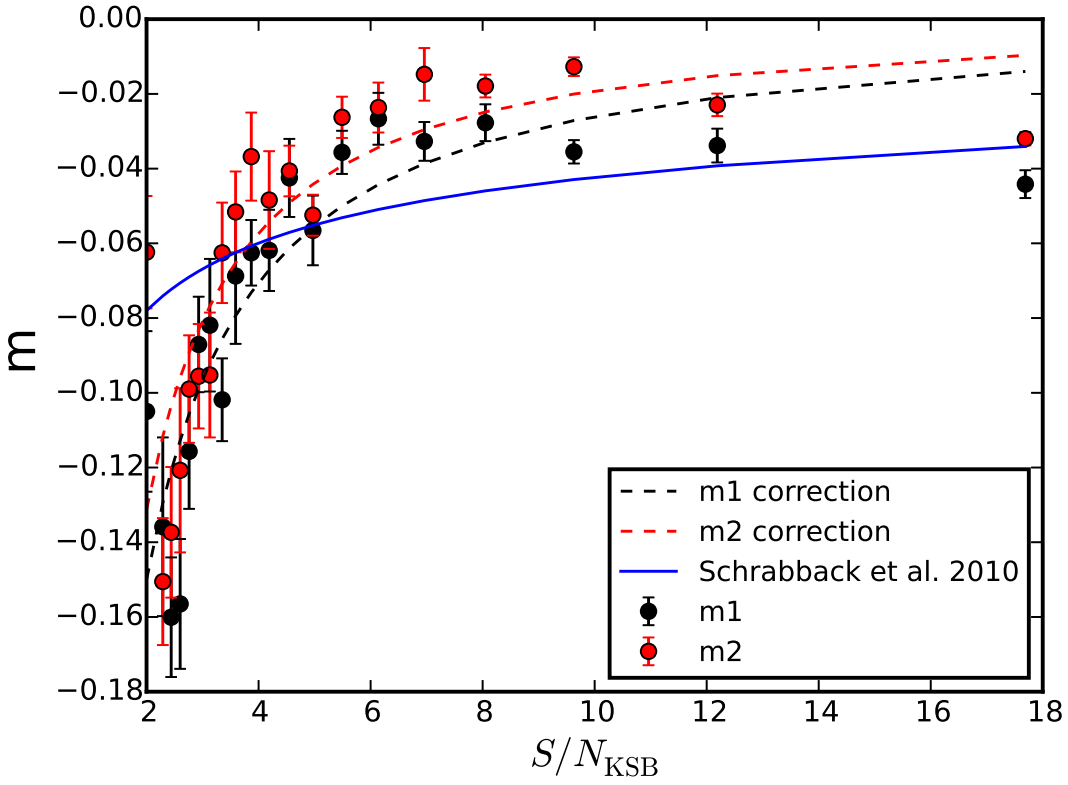

Figure 3.2: Dependence of the multiplicative bias on $S/N_{\rm KSB}$ and comparison between the $S/N_{\rm KSB}$ correction in S10 (shown in blue) and the new correction presented here. The red and black dashed lines show the correction for the two shear components.

still have similar systematic uncertainties. Because of the need to remove cluster member and foreground galaxies in order to avoid the dilution of the lensing signal, we reject many galaxies present in the images with the use of a colour selection cut. This reduces the number of galaxies that are used for the estimation of the shear. Weak lensing mass estimates benefit greatly with the inclusion of faint galaxies due to the increase of the total number of galaxies which can be used for the analysis, improving our mass constraints.

We apply this revised noise bias correction in the remaining analysis, where we always apply a correction on a galaxy by galaxy basis, scaling the KSB+ shear estimates by a factor $1/(1+m_{\alpha,\rm corr})$ depending on the $S/N_{\rm KSB}$ of the individual galaxy.

3.1.2 Bias estimates for the 'grid reference' simulations

In Table 3.2 we present the bias estimates obtained from the 'grid reference' simulations which indicates the residual bias computed for isolated galaxies. This is not the full story, as in the remainder of this chapter we estimate how confident we are in these results and add

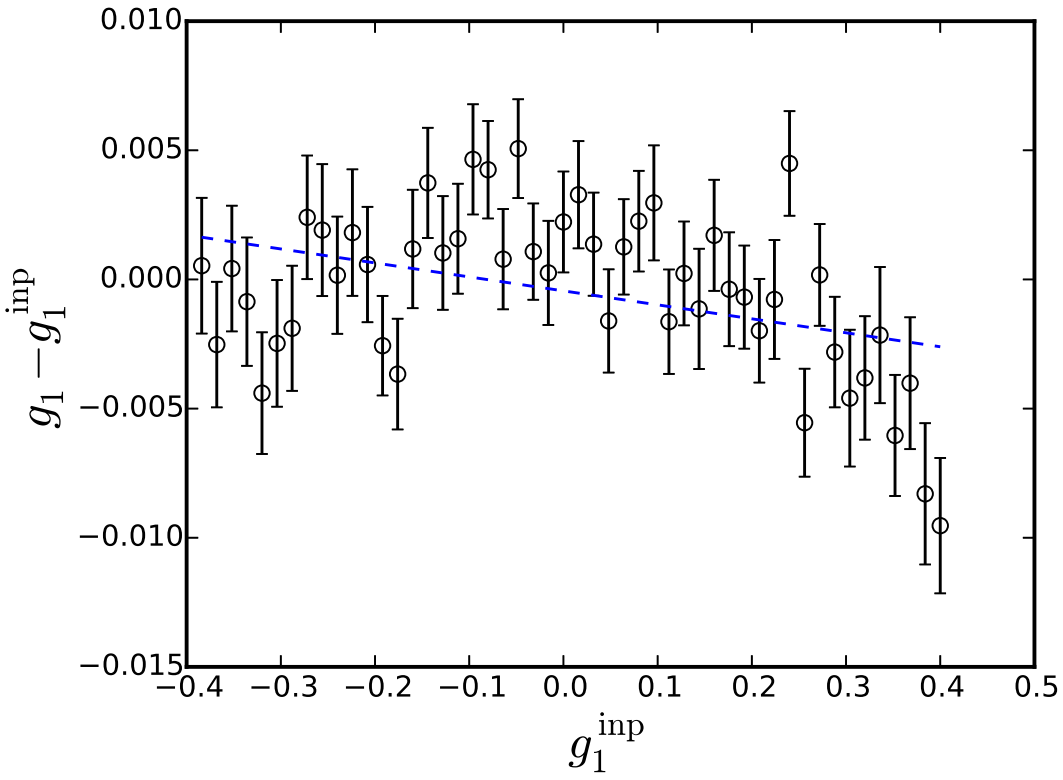

Figure 3.3: Dependency of the difference between input and measured shear as a function of the input shear. Here we applied the $S/N_{\rm KSB}$-dependent correction, and a cut on $S/N_{\rm flux} > 10$.

further biases coming from the selection bias, the presence of faint clustered galaxies and the presence of brighter cluster members. The final bias estimation is discussed in Sect. 3.4. But in this section we restrict ourselves to the analysis of the residual bias of the 'grid reference' simulation after the $S/N_{\rm KSB}$-dependent corrections presented in Eq. (3.1) in order to use it as a reference for the variation of inputs in the next subsections.

In these simulations, as was mentioned before, we also wanted to test stronger shear regimes. For this, we extended the typical range of shear values studied in simulations to the non-weak regime of $-0.4 < g < 0.4$. This is shown in Fig. 3.3. We can clearly see that there is a surprising effect for large shears, which is discussed in more detail in Sect. 3.1.7. In real analysis, we only use the $-0.2 < g < 0.2$ shear regime, which does not present this effect. The difference in multiplicative bias between both estimates is negligible, and only the additive bias changes in an important way (see Table 3.2). Throughout the rest of this work, we use the bias estimates of the $-0.2 < g < 0.2$ shear regime, but in many cases we plot the full range in order to have a more general understanding of the behaviour at strong shear regimes.

The residual multiplicative bias is smaller than 1% after applying the $S/N_{\rm KSB}$-dependent

Table 3.2: Multiplicative and additive bias for the reference simulation after a $S/N_{\rm flux} > 10$ and a $S/N_{\rm flux} > 7$ cut for the two shear regimes.

Cuts	Limits	$m_{1,\rm grid}$	$c_{1,\rm grid}$	$m_{2,\rm grid}$	$c_{2,\rm grid}$
		$[\times 10^3]$			
$S/N_{\rm flux} > 10$	$\lvert g\rvert < 0.4$	-7.3 ± 2.0	-1.2 ± 0.4	-6.7 ± 1.3	-4.3 ± 0.3
	$\lvert g\rvert < 0.2$	-8.1 ± 3.8	-1.0 ± 0.4	-5.1 ± 3.3	-3.5 ± 0.3
$S/N_{\rm flux} > 7$	$\lvert g\rvert < 0.4$	-10.8 ± 1.8	-0.7 ± 0.4	-11.8 ± 1.3	4.0 ± 0.3
	$\lvert g\rvert < 0.2$	-10.9 ± 3.5	-3.2 ± 0.4	-10.5 ± 3.3	-3.5 ± 0.3

corrections from Eq. (3.1) and a cut on $S/N_{\rm flux} > 10$. This reduces uncertainties compared to previous work. The errors were estimated by bootstrapping the galaxies in each image a 100 times and obtaining independent bias estimates for each bootstrap sample. The error will then be the squared root of the variance of the obtained bias in the 100 samples. We note a small difference between the bias in both shear components which can be explained by considering that the first component (m_1) has an effectively finer sampling along the pixel than the second (m_2). We include weights only depending on the galaxy magnitude-dependent RMS ellipticities. We use simple weights, thereby avoiding biases that can occur for ellipticity-dependent weights. The effect of this weighting on the bias is small ($\sim +0.3\%$). This indicates that most of the variation comes from the $S/N_{\rm KSB}$ which is already corrected for and not directly from the magnitude distribution which would affect the weights.

Even though our aim is to create simulations which are as realistic as possible, they are far from perfect. One of the effects that have not been included but could be important for the larger shear regime is flexion. The code we used, `GALSIM`, does not allow for the inclusion of flexion effects (Rowe et al. 2015) so the results may be slightly different if we were to account for this.

3.1.3 Residual dependence on $S/N_{\rm flux}$ and magnitude

Using the more general signal-to-noise expression defined in Eq. (2.75), we can study residual dependencies which are still present after the $S/N_{\rm KSB}$-dependent correction. This alternative definition is useful in order to perform signal-to-noise cuts, following the work in previous cluster work (S18a). It is interesting to understand how different this is from the $S/N_{\rm KSB}$ and in particular what is the residual multiplicative bias dependency on $S/N_{\rm flux}$ after the correction from Eq. (3.1) has been applied. The residual dependence we see in Fig. 3.4 is partly due to the different estimation of the two signal-to-noise ratios but also it is affected by the fact that the $S/N_{\rm KSB}$-dependent correction does not perfectly match the dependencies and does not fully correct for them. This is illustrated in Fig. 3.5 where we plot the bias in the same 20 $S/N_{\rm KSB}$ bins as in Fig. 3.2, but after the correction is applied. It shows that the residual dependence with $S/N_{\rm KSB}$ is also non-zero. The residual dependence comes from the fact that the $S/N_{\rm KSB}$-dependent correction over-corrects at $5 \leq S/N_{\rm KSB} \leq 8$, which corresponds with the positive bias at $10 \leq S/N_{\rm flux} \leq 20$. Similarly, the bias is slightly

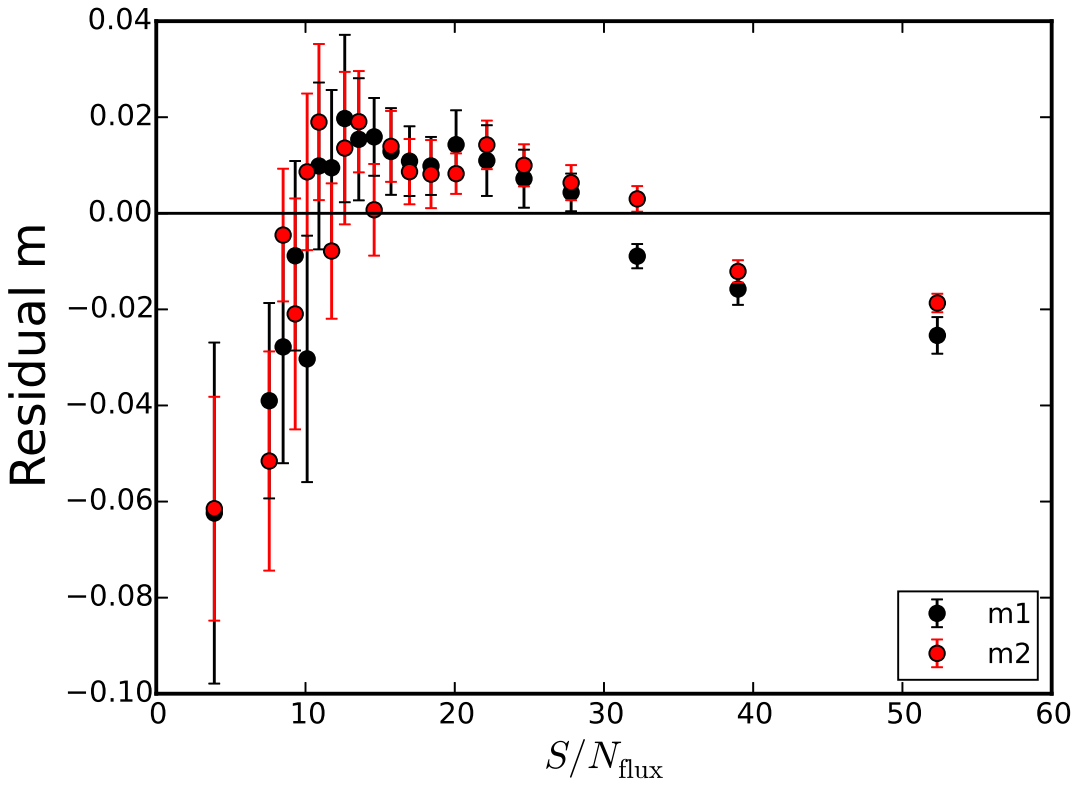

Figure 3.4: Dependence of the residual bias on the $S/N_{\rm flux}$, shown here after the $S/N_{\rm KSB}$-dependent correction is applied.

under-corrected at both very low and very high $S/N_{\rm KSB}$, which can also be seen in the $S/N_{\rm flux}$ dependence. The differences which appear in this analysis indicate that there could be other dependencies which are not accounted for, and a more detailed analysis could further reduce the residual bias. As an example, in Hoekstra et al. (2015), to properly account for the dependencies, they also employed a size-dependent correction, which is discussed for this work on Sect. 3.1.4. However, due to the distribution of our galaxies, they seem to counterbalance allowing us to still robustly determine the bias of the full population with our required constraints. If we use very different source populations for mass determination we may find that this effect is on a level which can be problematic.

As mentioned before, one of the uses of this signal-to-noise definition $S/N_{\rm flux}$ is to define quality cuts in order to select galaxies which behave robustly. This is very useful to restrict ourselves to galaxies with a controlled ellipticity estimation and obtain a good estimation of the shear. However, it can also remove large amounts of galaxies which will reduce our confidence on those estimates. In S18a, a conservative approach was used restricting the galaxies to $S/N_{\rm flux} > 10$. We tested the influence of different cuts by selecting the galaxies surviving each cut and performing an independent computation of the residual bias, which is

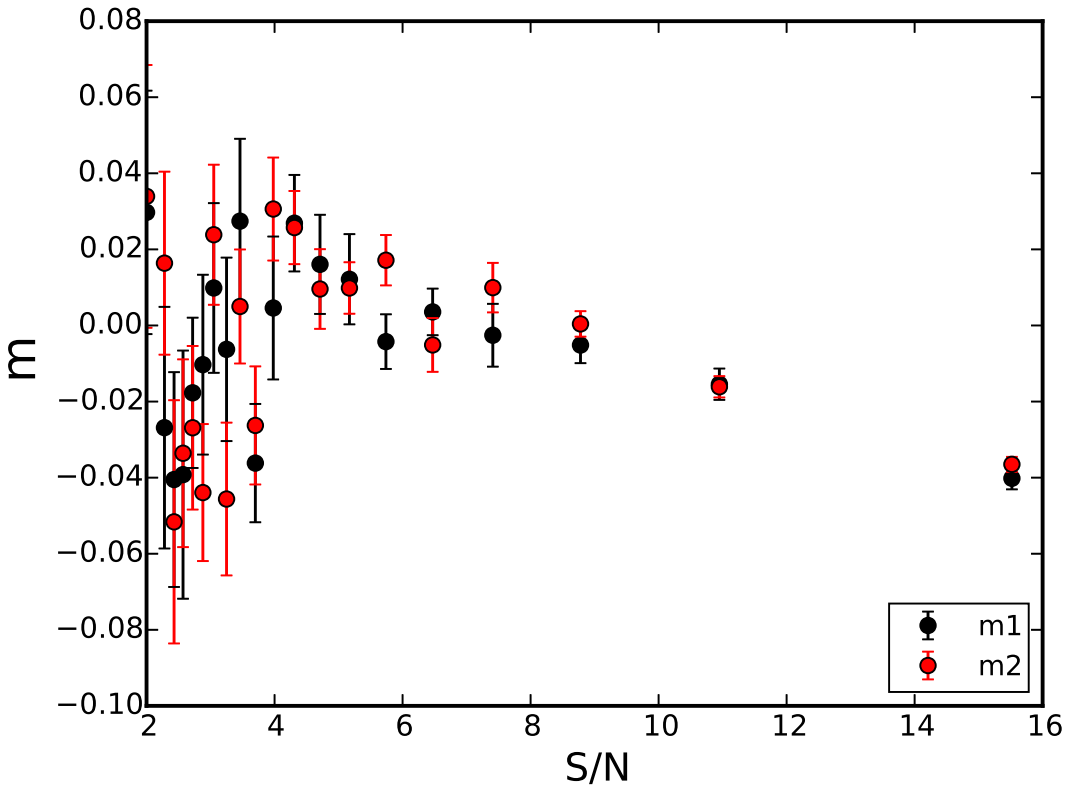

Figure 3.5: Dependence of the residual bias on the S/N_{KSB}, shown here after the S/N_{KSB}-dependent correction is applied.

Table 3.3: Multiplicative bias for the different S/N_{flux} cuts.

	m_1	m_2
$S/N_{\mathrm{flux}} > 10$	-0.0081 ± 0.0038	-0.0051 ± 0.0033
$S/N_{\mathrm{flux}} > 7$	-0.0101 ± 0.0022	-0.0112 ± 0.0025
$S/N_{\mathrm{flux}} > 5$	-0.0120 ± 0.0020	-0.0128 ± 0.0014

shown in Table 3.3.

For all cuts in Table 3.3, we have an absolute value of bias lower than 1.5%, which is still reasonable if it means that we can include more galaxies. A trade-off can be made where we lower the signal-to-noise cuts in order to have a larger background galaxy sample which is beneficial for the weak lensing analysis. For the reasonable $S/N_{\mathrm{flux}} > 7$ cut, we still maintain low bias, just above the $\sim 1\%$ regime in which we aim to control the systematics. For this reason, in the mass determination of the three relaxed clusters in Sect. 5.2 we use a $S/N_{\mathrm{flux}} > 7$. By lowering our S/N_{flux} cut from 10 to 7 we increase the number of galaxies by 15% which will provide more robust mass estimates. This analysis of the different cuts

indicates that it should be possible to use the current KSB+ shear determination methods in more extreme environment of the clusters, such as the inner parts in order to get more precise mass profiles. There, the galaxies generally have noisier estimates and lower signal-to-noise ratios due to contamination from the light of nearby cluster members which are more abundant in the central parts of the cluster. We should note that in the analysis of the impact of the different input parameters throughout the next few sections we present the estimates with a $S/N_{\rm flux} > 10$ cut only, for simplicity and following previous work. However, the final bias estimation in Sect. 3.4 is obtained for $S/N_{\rm flux} > 10$ and $S/N_{\rm flux} > 7$.

We also investigated the dependence of the bias on the magnitude of the galaxies, finding no significant trend after applying the $S/N_{\rm KSB}$-dependent correction (see Fig. 3.6, where we present the results of computing the bias over 20 magnitude bins containing the same number of galaxies). This is not surprising since magnitude and signal-to-noise ratios are strongly correlated. Brighter galaxies have smaller statistical errors when we measure their shapes as there is a larger contrast with the background. Fainter galaxies will be more noisy and increase the scatter in their measured ellipticities and hence in the bias. These galaxies are already corrected using Eq. (3.1). Fainter objects have a larger scatter, which comes from the lower signal-to-noise ratio of these galaxies. The scatter around zero and the large uncertainties indicate that the efforts to do a correction are unnecessary and will not greatly improve the results.

3.1.4 Radius-dependent bias correction

For the ACS-like simulation setup we also investigated the dependence of the multiplicative bias on the size of the galaxies, computing it in 20 different size bins from a little more than one pixel to 6, as can be seen in Fig. 3.7. The bias is computed after the $S/N_{\rm KSB}$-dependent correction was applied. We find a significant negative bias still present for small galaxies. The opposite is true for large sizes, where we find it over-corrects. This can happen because galaxies with the same magnitude that are larger have a lower signal-to-noise ratio, and our correction is based solely on the signal-to-noise ratio. Larger galaxies will then be over-corrected. One possible solution to this issue, that we tried, was fitting a logarithmic function to obtain an optional further correction of the size dependence of the bias, yielding

$$\begin{aligned} m_{1\rm size} &= 0.124 \log r\,[\text{arcsecs}] + 0.262\,, \\ m_{2\rm size} &= 0.083 \log r\,[\text{arcsecs}] + 0.185\,, \end{aligned} \tag{3.2}$$

where r is the FLUX_RADIUS. Since this correction was computed over estimates that were already corrected with Eq. (3.1), we aim to further reduce the residual dependence as a function of galaxy size. After applying both bias corrections as a function of $S/N_{\rm KSB}$ and size we obtained a $\sim -3\%$ bias. This indicates that the approach presented here of independently correcting for both $S/N_{\rm KSB}$ and size does not improve over our previous work. A possible reason for this is the large scatter in the bias as function of size (see Fig. 3.7).

As a logical next step, we performed a joint fitting both for $S/N_{\rm KSB}$ and size dependence

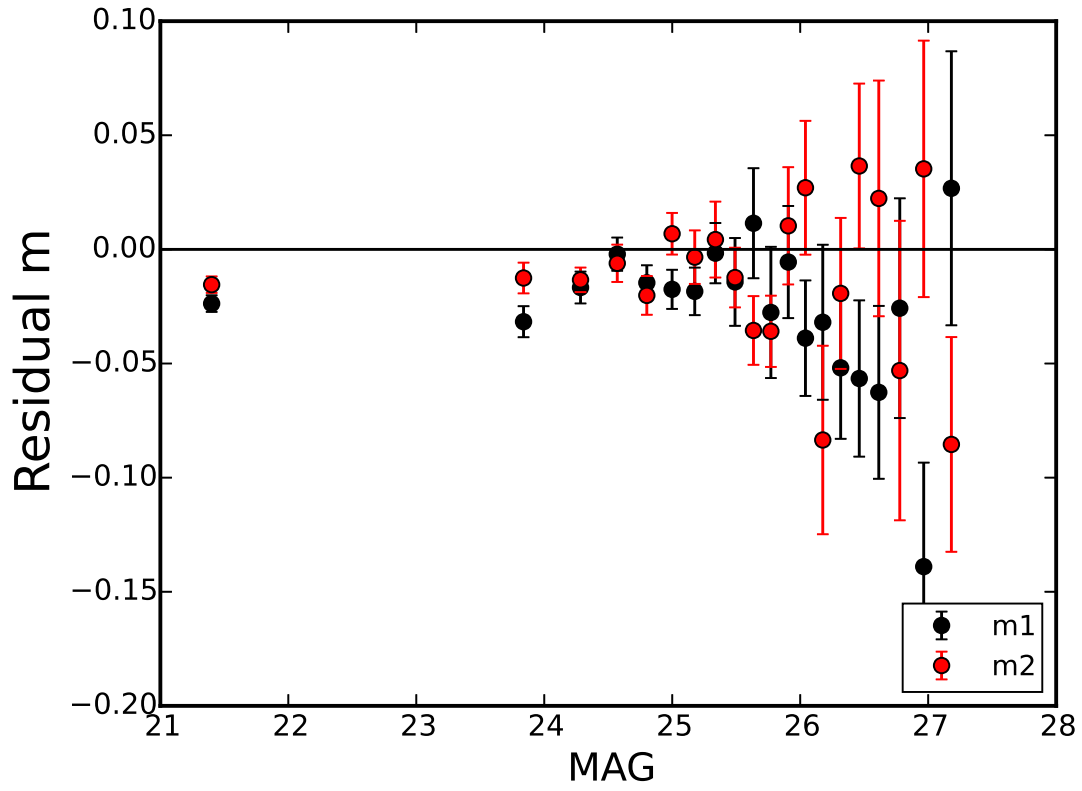

Figure 3.6: Dependence of the multiplicative bias on magnitude for the two ellipticity components. Here we have applied the $S/N_{\rm KSB}$-dependent correction and the cut $S/N_{\rm flux} > 10$. The bins are created to have the same number of galaxies but we have less galaxies for brighter magnitudes, which explains the different separation of points.

at the same time. For this, aiming to reduce the number of degrees of freedom of the fit, we use a simple linear dependency on the radius in order to avoid too many parameters added over the power-law behaviour of the $S/N_{\rm KSB}$ dependency. We obtained the correction

$$\begin{aligned} m_{1\rm corr} &= (-0.350\,(S/N_{\rm KSB})^{-0.611})\,(1 - 4.604\,r\,[\rm arcsecs])\,, \\ m_{2\rm corr} &= (-0.382\,(S/N_{\rm KSB})^{-0.735})\,(1 - 5.824\,r\,[\rm arcsecs])\,. \end{aligned} \tag{3.3}$$

The analysis with this correction gave us $\sim -2\%$ bias, only marginally better than the case of first applying a $S/N_{\rm KSB}$ correction and then the size dependence correction. As a result of this exercise, we decided not to implement this size correction for the remainder of the work presented here. But we note that in cases when the size of galaxies is more extreme, further work in this direction can help improve the bias estimates, or at the very least understand where the bias is coming from.

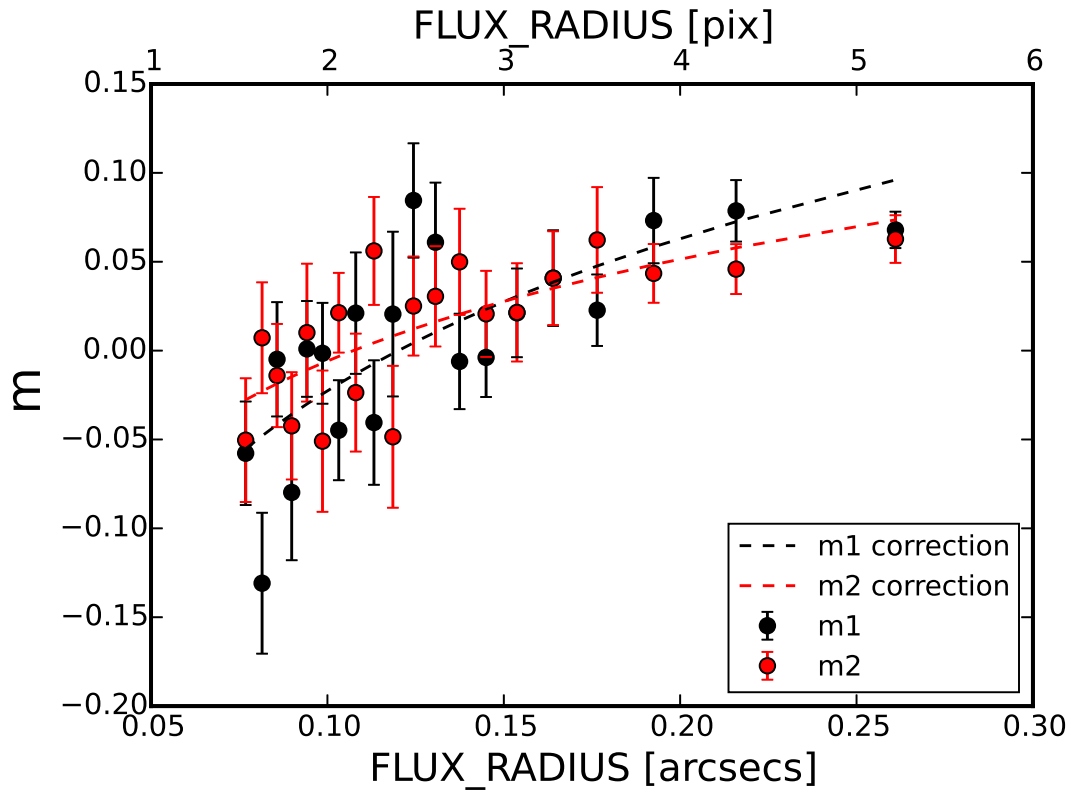

Figure 3.7: Multiplicative bias computed over 20 bins between 1 and 6 pixels of the FLUX_RADIUS parameter. The dashed lines show the fit in both components that we used for a size-dependent correction in Eq. (3.2).

3.1.5 Light profile

We found one of the input parameters in the simulations that influences the bias estimates the most is the light profile used for the creation of the galaxies. Depending on which choices are made, it can change the measured ellipticities and the bias in an important way. Since we obtain estimates on the changes in ellipticities caused by the lensing effect, the intrinsic shapes significantly affect our results. The ellipticity itself is not changed by the selected light distribution but the same cannot be said when measuring second-order moments since the different profiles will change the particulars of how concentrated the light profile is. For example, when using a Sérsic profile to describe the light distribution, (proportional to $r^{1/n}$) larger values of n describe a more centrally-concentrated profile. These differences in concentration can affect biases in the moment measurement, and PSF correction even if galaxies with the same ellipticity are simulated.

In order to test how this actually affects the bias, we generated four sets of simulations with different Sérsic index distributions, but maintaining all other parameters the same. Our

Table 3.4: Dependence of the noise-bias corrected multiplicative shear bias on the assumed galaxy light profile, applying the $S/N_{\rm KSB}$-dependent correction and standard $S/N_{\rm flux} > 10$ cuts. The residual bias estimates are obtained over the shear range $|g| < 0.2$.

Profile	m_1	m_2
De Vaucouleurs	-0.0506 ± 0.0040	-0.0513 ± 0.0033
Exponential	0.0010 ± 0.0026	0.0023 ± 0.0020
Flat distribution	-0.0032 ± 0.0022	-0.0097 ± 0.0032
Parametric	-0.0081 ± 0.0038	-0.0051 ± 0.0033

mock galaxies were simplified by using a Sérsic profile (see Eq. 2.76) as a general light profile so we only changed the index of the profile used. The Sérsic index changes the shape of the profile and allows us to create different kinds of galaxies to test the influence of the light distribution on the measured ellipticities. We created a set of pure exponentials ($n = 1$), a set of pure De Vaucouleurs ($n = 4$), a set using a flat distribution (uniform Sérsic index distribution between 0.3 and 6), and the more realistic setup employed in our reference simulation. For the two simplest cases, we have an unrealistic scenario where all galaxies have the exact same index. Elliptical galaxies generally follow a De Vaucouleurs profile, whereas spiral galaxies follow a flatter distribution on the center, such as the exponential profile, but we generally have a mixture of galaxies. The difference of the measured bias between these two cases is at the 7% level as is reflected in Table 3.4, which clearly shows it strongly impacts the bias results. We can also see in Fig. 3.8 the change in the recovered vs. the measured shear for the different cases as well as the linear fit for each of them. For all analyses we apply the noise bias correction calibrated on the reference simulation. The lines indicate the linear fits according to Eq. (2.74), where the offsets and slopes correspond to the additive and multiplicative biases. The large differences highlight the importance of accurately matching the light distribution between simulated and real galaxies since this will change the measured bias and hence, the mass measurements.

In our hopes of using more realistic inputs, we selected parametric fits to real galaxies which provide us with an estimation of the profiles of real galaxies to use as input. This should mimic the real data better than simply assuming the same profile for all galaxies. In order to do this, the simulation code we used, `GALSIM`, allows the use of a subsample of galaxies from the COSMOS sample (Mandelbaum et al. 2012; Rowe et al. 2015) with F814W<25.2 as base for our mock galaxies. This catalogue is colour-selected to follow the $V_{606} - I_{814} < 0.4$ to approximately match the selections applied in S18a and S20. A fit to a Sérsic profile was performed for each galaxy in the catalogue and the best fit Sérsic index was used to draw our mock galaxies from. To maintain a realistic approach, for each of our mock galaxies, we randomly selected a real galaxy from the catalogue and used their measured Sérsic index and ellipticity. In Fig. 3.9 we can see the index distribution of real galaxies obtained by the parametric fits. We should note that the excess in the last histogram bin is caused by the maximum allowed index in `GALSIM`. This is also seen in the first bin on a smaller scale, but is only a computational artefact which does not greatly affect the results. It can be seen that the

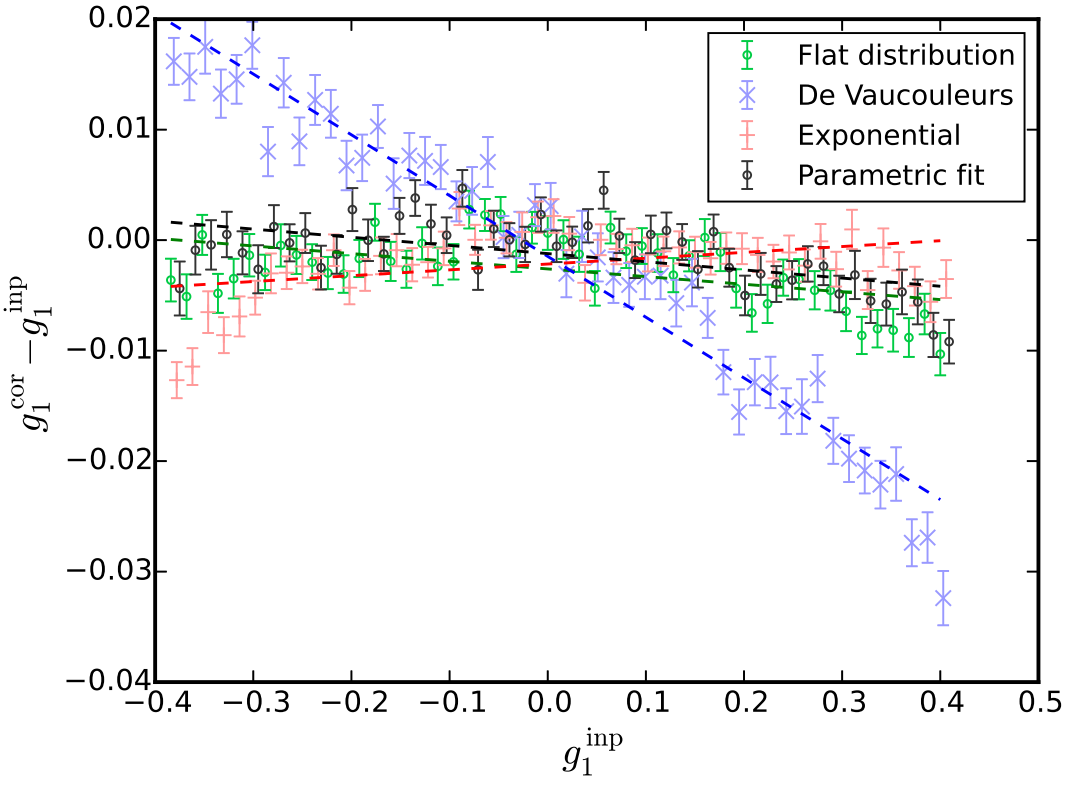

Figure 3.8: Dependence of the difference between the input and the recovered shear on the input shear for the first component. The different symbols correspond to the different light profiles used to create our mock galaxies. We show the cases of a flat Sérsic index distribution in green, a purely De Vaucouleurs profile in blue, a purely exponential in red, and the more realistic case of the parametric fit to the COSMOS galaxies in grey. For the result shown here the S/N_{KSB}-dependent correction and the $S/N_{\mathrm{flux}} > 10$ cut have been applied. Shown for the full $|g| < 0.4$. The causes of the deviation of some points at strong shear are discussed in Sect. 3.1.7

index distribution is skewed towards lower indices, with a median of 1.24. This is consistent if we look at the results in Fig. 3.8, where the estimated bias of the parametric fit is similar to the exponential (with $n = 1$). It is also understandable if we consider the types of galaxies we generally have in the observations. Late-type galaxies constitute the majority of our expected background source population. The careful consideration of the properties of the galaxies observed with a different filter and with a different selection is important as it has been shown here that it modifies the measured bias. The multiplicative bias differences are relatively small except for the simulation containing only De Vaucouleurs profiles, which exhibits a substantial residual multiplicative bias of $\sim -5\%$. From this we conclude that the input galaxy light profiles can play a relevant role, but that minor differences do not have a major impact. We note that the COSMOS Sérsic index distribution was also derived from a slightly

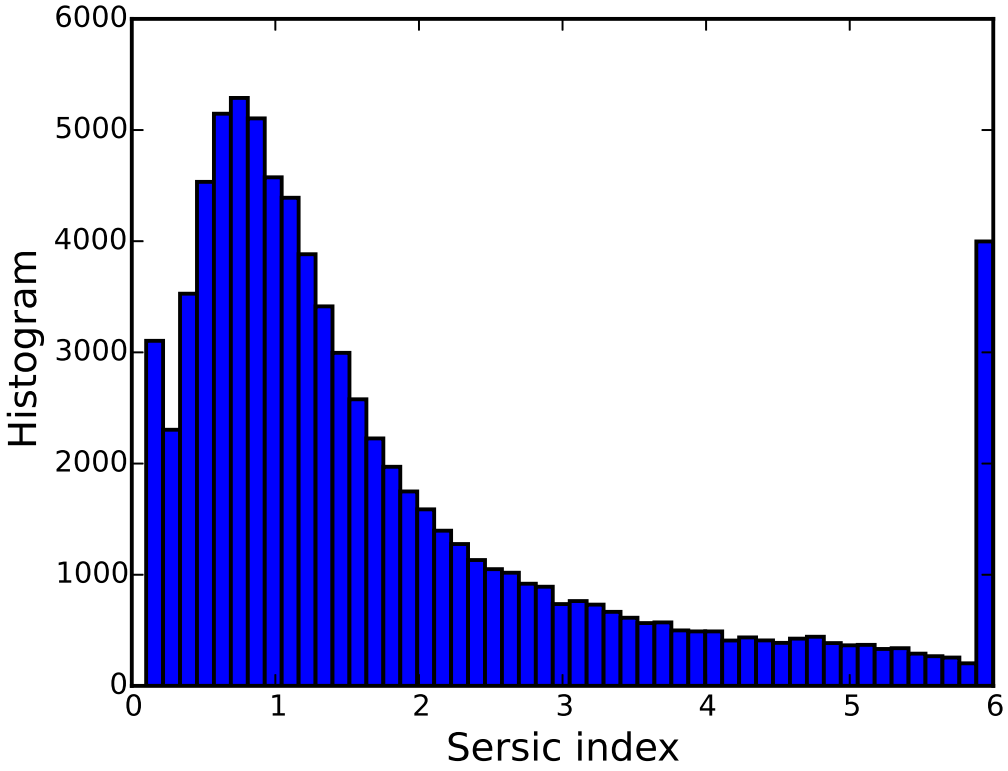

Figure 3.9: Distribution of Sérsic indices in the parametric fit to real COSMOS galaxies. The peak in the last bin is due to the limits in the index allowed by `GALSIM`. Everything larger than 6 is added in that bin.

brighter galaxy sample. Accordingly, it might not exactly match the distribution of our fainter galaxies. Nevertheless we expect that both populations are dominated by late-type galaxies and the differences to be negligible. As an extreme sensitivity test we also investigated the unrealistic case of a flat distribution (uniform Sérsic index distribution between 0.3 and 6). We use the bias difference $|\Delta m| \simeq 0.5\%$ between the fairly realistic simulation employing the parametric fits and the fairly unrealistic simulation using a flat distribution as a conservative estimate for the systematic uncertainty associated with the galaxy light profile assumptions (see Sect. 3.4).

When creating the mock galaxies with different light profiles we obtained slightly different distributions of the parameters shown in Fig. 3.1, especially for the size distribution. Performing a reweighting of the size distribution to match it to our CANDELS reference did not change the bias significantly, so the differences shown in Fig. 3.8 are not caused by these minor differences.

We should note that `GALSIM` also offers the option of using real image cut-out as input for the mock galaxies. This would be the most realistic approach as it captures the irregularities

Table 3.5: Dependence of the noise-bias-corrected multiplicative shear bias on the intrinsic ellipticity RMS, applying the $S/N_{\rm KSB}$-dependent correction and standard $S/N_{\rm flux} > 10$ cuts. The residual bias estimates are obtained over the shear range $|g| < 0.2$.

RMS	m_1	m_2
0.20	-0.0019 ± 0.0020	-0.0025 ± 0.0025
0.25	-0.0052 ± 0.0037	-0.0058 ± 0.0033
0.30	-0.0070 ± 0.0035	-0.0065 ± 0.0029
0.35	-0.0075 ± 0.0030	-0.0040 ± 0.0022

in the light profile. However, the best images we can use come from the HST telescope itself. This means that the PSF sizes are comparable to our mock PSF and the computational processes required to deconvolve the galaxies, shear them and reconvolve them with the same size PSF creates artificial effects that makes it not usable. However, this was the approach taken in Sect. 4.2, where we are dealing with a larger PSF.

3.1.6 Intrinsic ellipticity

The intrinsic ellipticity of a galaxy, is the real ellipticity it has, before any light distortion happened. In weak lensing we are dealing with very small changes in the ellipticity of a galaxy due to the gravitational potential of the lens. This becomes a problem since galaxies themselves are not perfectly circular, but rather have a certain intrinsic ellipticity which is generally larger than the shear introduced with lensing. Because of such small changes in an already elliptical galaxy, we cannot have estimations of weak lensing shear of individual galaxies and we need to perform a statistical analysis of large amounts of galaxies. Also due to this, the selection of the intrinsic ellipticity distribution of the galaxies in the simulated images can play a significant role for the estimation of the bias (Viola et al. 2014). In order to test how important the particular choices become, we set up 4 sets of simulations with the same parameters, except for the intrinsic ellipticity. Each one had an input Gaussian ellipticity distribution for each component ϵ_α, with different RMS modulus $\sigma(|\epsilon|)$ values ranging from 0.2 to 0.35 (computed from both ellipticity components together). We then draw the elliptiticity of each galaxy randomly from such distributions. This should allow us to test how the bias measurements change due to this effect.

Comparing the bias obtained with the 4 different sets in Table 3.5, we see only minor ($< 0.5\%$) differences. These results are also consistent with the ones obtained for the reference simulation (which has a $\sigma(|\epsilon|) = 0.28$), so we conclude this choice does not play a big role in the bias determination. This means that we do not expect this choice to have any important effect in our analysis and the particular $\sigma(|\epsilon|)$ we select during the simulation creation will not change the obtain bias within the uncertainties we currently have in the analysis. For the rest of this section, we used the ellipticity distribution from the parametric fits from COSMOS, which is different than the ellipticities used here. However, as we showed, the changes due to this choice are negligible.

3.1.7 PSF modelling and deviation at stronger shears

The KSB+ formalism makes the simplifying assumption that the PSF can be described as an isotropic function convolved with a small anisotropic kernel, which is not strictly met for many realistic PSFs. In fact, the Tiny Tim PSF we use here has an ellipticity $e = 0.072$. Therefore, we investigate how sensitively our bias estimates depend on the details of the PSF model that is employed in the simulation. To obtain a realistic model for our PSF we used `Tiny Tim` (Krist et al. 2011). This tool was created to accurately match the observed PSF in real HST images for some of its cameras, including ACS. We selected the PSF model parameters according to the best fit to real HST/ACS starfield images obtained by Gillis et al. (2019). They use models from `Tiny Tim` and modify them in order to fit the real PSFs better and found an important deviation between the default setup and their modified one, so we use the coefficients provided in their work. In particular, we selected an ACS-like PSF for the filter F606W with a subsampling of 3. This means that the pixel scale of the input PSF image will be $0.''0165$/pixel, 3 times smaller than the PSF of the final simulated image ($0.''05$/pixel). This is critical to avoid pixelation issues when convolving with the mock galaxies and adding the pixelation for our images. Other parameters that also needed to be chosen, include the pixel position, for which we selected $x = 1000$, $y = 1000$ in chip 1, and the focus value for which we chose a typical average value of $-1\,\mu m$. This leads to a PSF with ellipticity e_1 =0.018, e_2 =0.063 (when measured with a weight function scale $r_g = 2.0$ pixels). We tested the variation of the PSF in the field and in the chip which is only a lower-order correction in our analysis. The light profile of our object was also required, which we chose as $F(\lambda) = \lambda^{-1}$, which is a good approximation to the behaviour of our galaxies. One of the main problems when it comes to the ACS PSF is the fact that because of its placement in space, the PSF changes in time due to focus variations caused by the thermal fluctuations that happen in orbit (Heymans et al. 2005; Rhodes et al. 2007; Schrabback et al. 2007). A distribution of focus values for the HST/ACS observation of the COSMOS field was shown in Rhodes et al. (2007) and is reproduced here in Fig. 3.10. We tested the influence of this in our analysis, finding that the bias varies less than 1% within the typically expected focus, ranges and spatial PSF variations across the field of view. As mentioned before, as a default value we choose a focus of $-1\,\mu m$, which is a central value in the expected distribution and should provide us with a rough estimate of the general PSF in ACS images.

Charge diffusion and comparison with other profiles

The ACS PSF suffers from charge diffusion (Krist 2003). This means that electrons near the edges of pixels have a chance to travel to neighbouring pixels, effectively creating a blurring effect which needs to be accounted for in our models. While testing different PSF models, we found that excluding this effect in the simulations PSF increased the bias to $\sim -4\%$. In our analysis, this effect is mimicked by using a Gaussian kernel which will slightly smooth the PSF accounting for the charge diffusion blurring. An example of how our subsampled PSF with and without charge diffusion looks is shown in Fig. 3.11. The PSF without charge diffusion has sharper features that are very different from a Gaussian PSF and

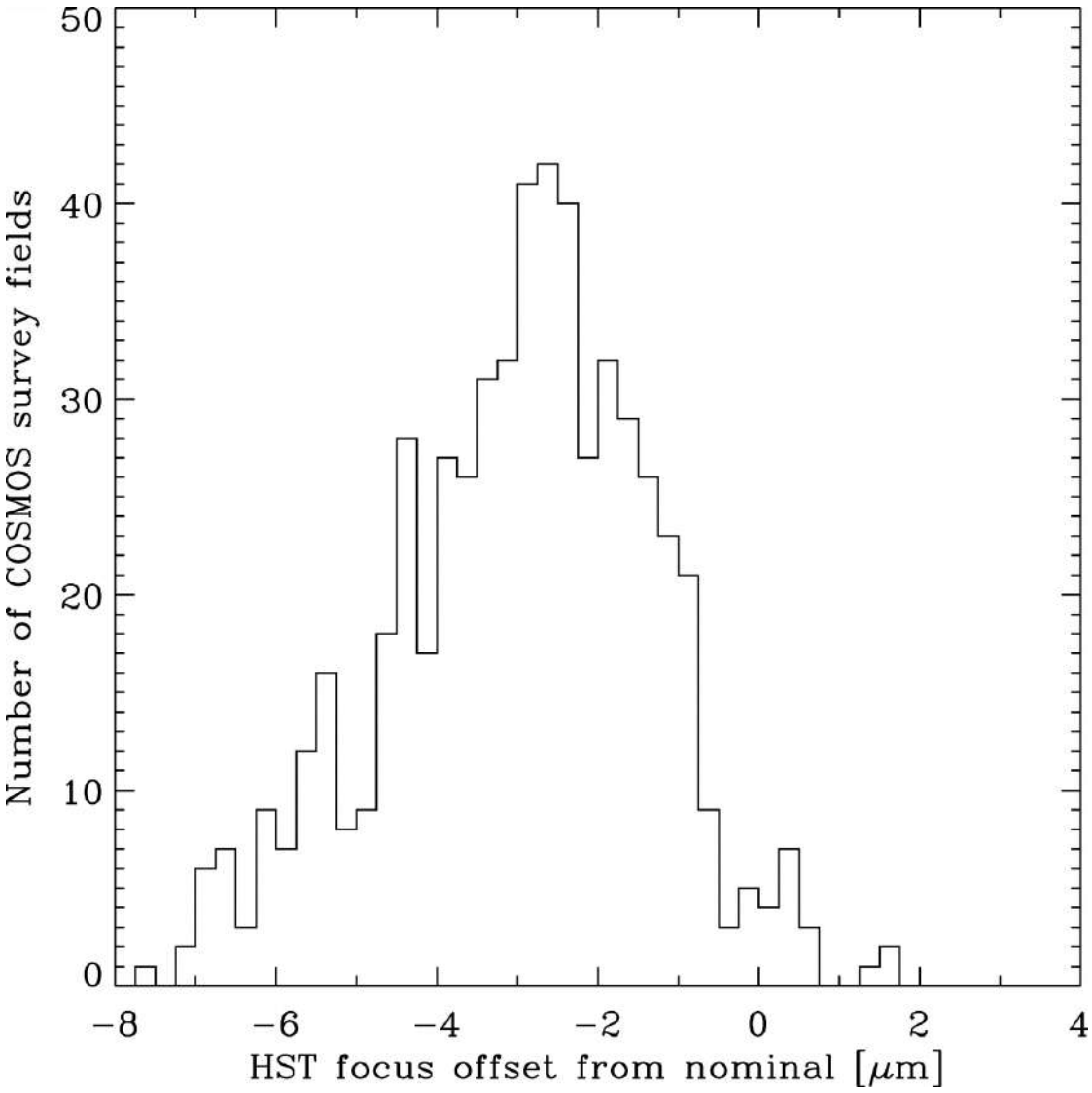

Figure 3.10: Focus values that the HST/ACS PSF can take and their frequency on the COSMOS observations. Credit: Rhodes et al. (2007)

might be the cause of the large differences we see. The results in Table 3.6 show a $\sim 4\%$ difference in the bias when considering the charge diffusion. It should be noted here that the signal-to-noise dependent correction applied to the galaxies in both simulations is the one obtained in Sect. 3.1.1 which uses the charge diffusion-corrected PSF. With a correction based on each set of simulations we could obviously reduce the bias. However, here we do not aim to show which bias is more "correct" but simply how the results change with the particulars of the implementation of the simulation code so for consistency we use the same correction in all cases. We choose the PSF with charge diffusion as more realistic since that

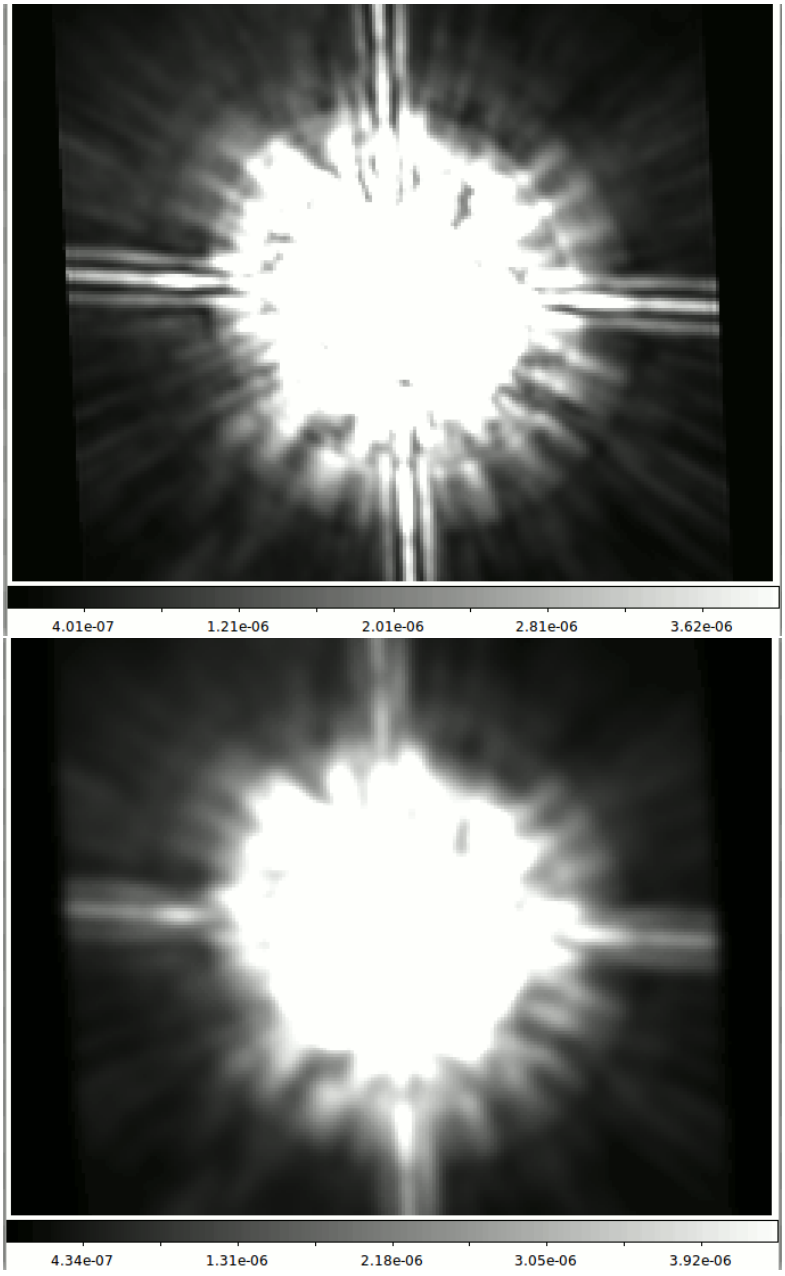

Figure 3.11: Realistic PSF created by `Tiny Tim` without charge diffusion on top and with it on the bottom.

is what happens in real data images and it will better resemble the real PSF so it is used in the rest of this work.

Even though, it would be naive to use a Gaussian profile in our simulations as it is vastly different to the real PSF, we created a set of simulations using such PSF. We obtained a large

Table 3.6: Table with the values for the bias depending on the PSF implementation with the S/N_{KSB}-dependent correction from Eq. (3.1). The residual bias estimates are obtained over the shear range $|g| < 0.2$.

PSF	m_1	m_2
Gaussian	0.0400 ± 0.0066	0.0456 ± 0.0050
Moffat	0.0103 ± 0.0029	0.0125 ± 0.0030
`Tiny Tim`	-0.0081 ± 0.0038	-0.0051 ± 0.0033
No charge diffusion	-0.0460 ± 0.0040	-0.0501 ± 0.0039

positive bias which is shown in Table 3.6 which is most likely caused by the over correction due to our signal-to-noise dependent correction. In any case this is a very unrealistic scenario which was only tested in order to illustrate the importance of choosing a good PSF model.

A Moffat profile is a better model in the case when we do not have a tool such as `Tiny Tim`, so we might be more tempted to use it. To test how this wrong assumption would influence the measured bias, we modified the simulations to use a Moffat profile and matched the half-light radius of the PSF to be the same as for the `Tiny Tim` model ($0\farcs07$). The estimation of the bias for this case is shown in Table 3.6. The Moffat PSF also gives a positive bias, which we again assume it is caused by the S/N_{KSB}-dependence correction whose behaviour can depend on the PSF implementation used and was calibrated on the HST/ACS-like PSF. The changes are of the order of 2% which indicates that a good PSF model is needed in order to obtain trustworthy bias estimates.

Ellipticity and orientation of the PSF

Because of the complexity of the PSF and the large ellipticity it has ($\sim 7\%$), we wanted to better understand some of its possible shortcomings as we found some indication of a deviation from the linear behaviour we use to compute the bias already mentioned before. To test the cause of this, we also generated a set of simulations in which the PSF has been rotated by 90 degrees compared to the default reference simulation. For both setups the shear recovery is compared in the top panel of Fig. 3.12. All other inputs were kept the same, but we rotated the PSF model before convolving it with the galaxy profiles. This would not have any effects if the PSF was point-symmetric but it can have some impact for more complex and elliptical PSFs. The residual bias obtained from the simulation with a rotated PSF, after the S/N_{KSB}-dependent correction was applied, can be seen in Table 3.7. We can see similar multiplicative bias but a change in sign for the additive bias between the reference simulations and the rotated ones. This is slightly worrying for the cases when the additive bias plays an important role, but not so much for the cluster work that is our main focus.

Inspecting Fig. 3.12 we see the behaviour does not follow a linear relation. We should note here that these findings do not mean a quadratic response of the bias in the case of stronger shears. For a quadratic shear response we would expect the dependency to be symmetric for negative and positive shear values due to the sign of the shear simply being the orientation

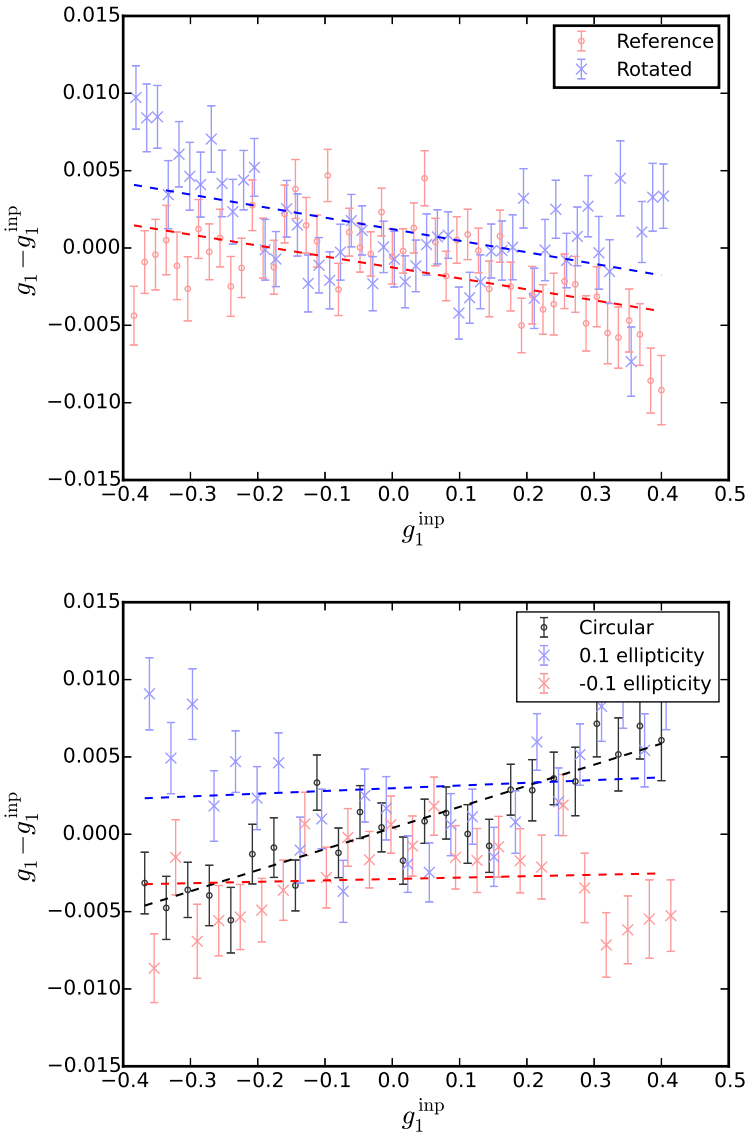

Figure 3.12: *Upper*: Comparison of the residual bias from the reference and the rotated simulation with ACS-like PSF. The red points refer to the reference simulations whereas the blue come from the 90 degree-rotated simulation. *Lower*: Comparison of the residual bias obtained for a circular Moffat PSF in grey, a modified Moffat with a $e_1 = 0.1$ ellipticity in blue and with $e_1 = -0.1$ ellipticity in red.

(parallel or perpendicular) with respect to the component axis. For example, if the difference between the recovered and input shear is positive for positive shear values, then we should find a negative difference for negative shear. However, in Fig. 3.12 the difference for the reference simulation is negative both for positive and negative shear values. This indicates that it is not a quadratic response but rather a dependency of the additive bias with the input

Table 3.7: Residual multiplicative and additive bias for the 90-degree rotated simulation after a $S/N_{\rm flux} > 10$ cut. These estimates come from the shear regime $|g| < 0.4$ as we are studying the behaviour at large shears.

	m	c
e_1	-0.0076 ± 0.0023	0.0012 ± 0.0003
e_2	-0.0069 ± 0.0013	0.0045 ± 0.0003

shear. To test the origin of this effect, we set up 3 sets of simulations using a Moffat PSF with ellipticities 0.1, 0 and -0.1. We used a Moffat profile, despite not being a realistic model for the HST/ACS data due to its intrinsic circular symmetry with no ellipticity. This way, we can modify its shape and test the difference in the shear estimations. From Fig. 3.12 we conclude that the deviation from the linear behaviour has a dependency with the ellipticity of the PSF, being non-existent for the circular PSF and having a different sign for -0.1 and 0.1 ellipticities. The response of our KSB+ algorithm seems to depend on the ellipticity of the PSF. This effect has not been seen in previous similar work. It seems to arise in our particular implementation of the shear measurement algorithm. One of the possible reasons why it appears may be the approximation $(P^g)^{-1} = \frac{2}{\mathrm{Tr}[P^g]}$. However, as long as this ellipticity is well reproduced in our simulations, the bias derived from them is comparable to what is found in real images. Nevertheless, further work on this topic would improve the understanding of the bias and could be important for next generation surveys which require tighter constraints.

3.2 Cluster galaxy blending

In the previous section, we have simulated isolated galaxies which do not suffer from any neighbour effects. However, real images suffer from contamination coming from nearby galaxies. In order to increase the realism of our simulations, we take a first step by studying the impact that the presence of bright cluster members has on the bias estimation. E.g., the wings of their extended light profiles might contaminate the light distribution of nearby sources, potentially leading to biased shape estimates. This is a cluster-specific issue that is not generally studied in this kind of work. Different to bright foreground galaxies, which are randomly positioned, cluster galaxies have a higher number density in the cluster cores where shears are stronger, following an NFW profile. This can impact the shear estimates of the background galaxies. For this analysis, we created two sets of simulations, one containing only lensed background galaxies, and one that also contains cluster member galaxies and other foreground galaxies. For the background galaxies we use the same galaxy properties as in Sect. 3.1, but placed randomly in the image rather than on a grid. Note that this is not yet a fully realistic scenario, since the simulations are still missing the clustering of source galaxies, as well as very faint galaxies below the detection threshold. These effects will be studied in Sect. 3.3, but are not needed for the current step, where we are investigating the impact of bright cluster and foreground galaxies. This simplifies the creation of multiple

realizations by randomly placing our galaxies, since we only have limited cluster catalogues. The aim in this section is to study the difference between the background-only and with the presence of cluster members, so this choice is not critical to understand the obtained results. The $S/N_{\rm KSB}$-dependent correction as well as the $S/N_{\rm flux} > 10$ cut are implemented in the analysis, although we alternatively repeat the same analysis with $S/N_{\rm flux} > 7$, which changes the results only marginally (the final bias estimation is presented later in Table 3.12).

Instead of images with constant shear, we used background galaxies that were placed randomly in the image and sheared according to their relative position to the center of the cluster assuming an NFW profile (see Eq. 2.19). A particular mass and concentration needs to be assumed in order to know the strength of the shear as a function of the position. We chose $M_{200c} = 5 \times 10^{14} M_{\odot}$, $c_{200c} = 4$, a redshift of the cluster of $z_{\rm lens} = 0.3$ and of the source of $z_{\rm source} = 0.6$ to obtain the shear values of the background galaxies. This configuration corresponds to typical measurements of low-redshift clusters using ground-based weak lensing data, but the resulting level of shears is in fact comparable to typical HST measurements for high-redshift clusters. This setup provides a more realistic scenario for measuring the shear than the grid placement of galaxies since the ellipticity of the galaxies needs to be averaged in radial bins instead of being constant for the full image. This also means that not all galaxies in a bin will have the exact same shear as opposed to the situation in Sect. 3.1 where all galaxies in one image had the same input shear. We again created an identical image with a 90 degree rotation of the intrinsic ellipticity of each galaxy before the shear was applied. Before averaging their ellipticities, rotated galaxies are matched in order to reduce shape noise. The same random seed was used for the creation of the simulations with and without cluster members in order to have the exact same background galaxies with the same properties and in the same position. This allows for a direct comparison of the obtained bias.

The cluster members will be a different galaxy population with respect to the background galaxies. These cluster galaxies do not contribute to the shear estimates and hence the analysis is not as sensitive to particular shapes or sizes as for the case of the creation of background galaxies. It is enough for us to have a rough idea of their properties to obtain enough information to determine how important their light contamination is in our estimates. For the determination of the properties of the cluster member galaxies we used catalogues from the MAGELLAN/PISCO (Stalder et al. 2014) follow-up of SPT clusters of various redshifts (z = 0.28 - 1.1). The cluster redshifts used as reference for this analysis were obtained from Bocquet et al. (2019). This can roughly represent the properties of clusters we would also see in HST/ACS images, with minor differences which are not critical to the analysis presented here. The cluster galaxies have magnitudes from $18 < r < 24$ which are a few magnitudes brighter than our background galaxies (which go to $V_{606} = 26.5$). We used the positions and magnitudes of the real catalogues, but we assumed for them a De Vaucouleurs profile and a random ellipticity drawn from a ellipticity distribution with $\sigma(|\epsilon|) = 0.2$.

If we just take the cluster catalogue and use the galaxy positions as input for our mock cluster members, we only have one catalogue per redshift, which might lead to picking up particular features of that galaxy configuration. To avoid this, we modified their position with respect to each other, but maintaining their distance to the cluster centre. This was

done by placing them in a random position along a circle at their original distance to the center. We created multiple images with different realizations of background galaxies and different cluster catalogues in order to stack the profiles and obtain a more significant result, independent of the particulars of each cluster. Once both sets of simulations were created, we can compare their recovered shear profiles. Because we know the input galaxy properties and their shear, we can easily compare how the estimated shear changes when introducing cluster members.

Following the analysis in real cluster images, we created masks around the bright (mostly stars which we do not have in our simulations) and extended objects, which will mostly remove cluster members. This is the situation we have in real images, so it is important to follow the same approach here to avoid the introduction of artificial biases. For the mask creation, we perform a `SExtractor` object detection with a large detection threshold. The minimum number of pixels for it to be detected (DETECT_MINAREA) has to be 2000 pix for the extended objects and 100 pix for the bright ones. We then extend the radius of the object by 3 pixels to create the masked area. For the brightest objects we include objects brighter than magnitude 20 in our images. This will exclude from our shear estimates the areas around the brightest and most extended objects, which reduces the light contamination coming from those galaxies and should provide us with less biased shear estimates. This is also done for the real cluster images, so their creation here comes from our intent to mimick the whole process that the real images go through.

We present two examples of simulated images for two of the clusters which are at different redshifts ($z = 0.28$ and $z = 0.72$) in Fig. 3.13 and Fig. 3.14. Each image shows the full cluster image (background+cluster members), a cut-out of the center, the same region for the background only simulated image, and the corresponding mask. The lower redshift cluster has a larger number of bright galaxies.

Fig. 3.15 shows the mean input and recovered shear profiles for the two simulation setups (with and without bright galaxies) averaged over all clusters with $z > 0.7$ in the top panel. The differences between the input and the measured shear are consistent with the general bias estimated in Sect. 3.1. The bottom panel shows the relative difference between the two recovered profiles, which corresponds to the change in the multiplicative bias caused by the presence of the bright foreground and cluster galaxies. There are no clear trends in this case. We also computed an estimate of the differences in the tangential shear as a function of the redshift of the clusters (Fig. 3.16). We have four distance bins in order to test the different behaviour for the inner galaxies and the ones further away. We also do a separate analysis for clusters $z < 0.7$ and $z > 0.7$. We generally find that adding the bright foreground and cluster members only has a minor impact on the shear recovery. The biggest impact is detected for lower redshift clusters ($z < 0.7$) at scales $70 - 100$ arcsec, amounting to a $1.13\% \pm 0.33\%$ positive multiplicative bias. We expect that the impact decreases for higher redshift clusters given the stronger cosmological dimming of their cluster members. Indeed, computed over one bin between 70-165 arcsecs we find a very minor bias of $0.48\% \pm 0.38\%$ for the simulated $z > 0.7$ clusters, which approximately corresponds to the scales and redshifts used in S18a. A detailed list of the different bias in all cases can be seen in Table 3.8. The global estimate of the bias for all clusters and all distances was computed for a general estimation

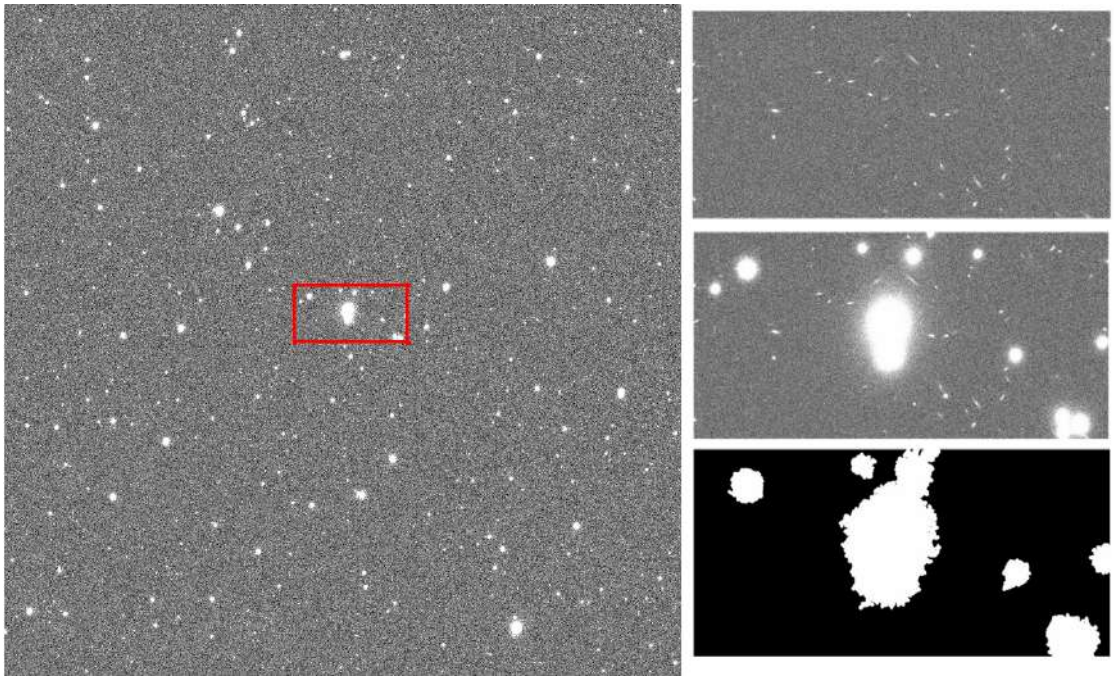

Figure 3.13: Example image of a simulated cluster at $z = 0.28$. A cut-out of the full image, shown in red, can be seen in the right for the simulations with background galaxies only (top), with added cluster members (middle) and showing the mask used to remove bright objects (bottom). The full image and cut outs spans $300'' \times 300''$ and $50'' \times 25''$, respectively.

Table 3.8: Detailed estimate of the bias due to the presence of bright galaxies for the different cluster-centric distance and in two redshift bins.

Distance	**Cluster redshift**	**Bias estimate**
$40''$-$70''$	$z < 0.7$	0.0021 ± 0.0033
$40''$-$70''$	$z > 0.7$	0.0044 ± 0.0039
$70''$-$100''$	$z < 0.7$	0.0113 ± 0.0033
$70''$-$100''$	$z > 0.7$	0.0052 ± 0.0039
$100''$-$135''$	$z < 0.7$	0.0054 ± 0.0035
$100''$-$135''$	$z > 0.7$	0.0020 ± 0.0042
$135''$-$165''$	$z < 0.7$	-0.0058 ± 0.0043
$135''$-$165''$	$z > 0.7$	0.0003 ± 0.0053

of the contribution. We computed a similar analysis for $S/N_{\rm flux} > 7$ obtaining a bias of $0.25\% \pm 0.40\%$ for clusters $z > 0.7$, which is included in the final bias estimation in Sect. 3.4.

This analysis indicates that there is no significant change in the bias obtained with and without the presence of cluster member galaxies. This is partially due to the masking and the removal process performed in the KSB+ pipeline.

Given the redshift dependence of the bias caused by cluster galaxies, we decided to treat

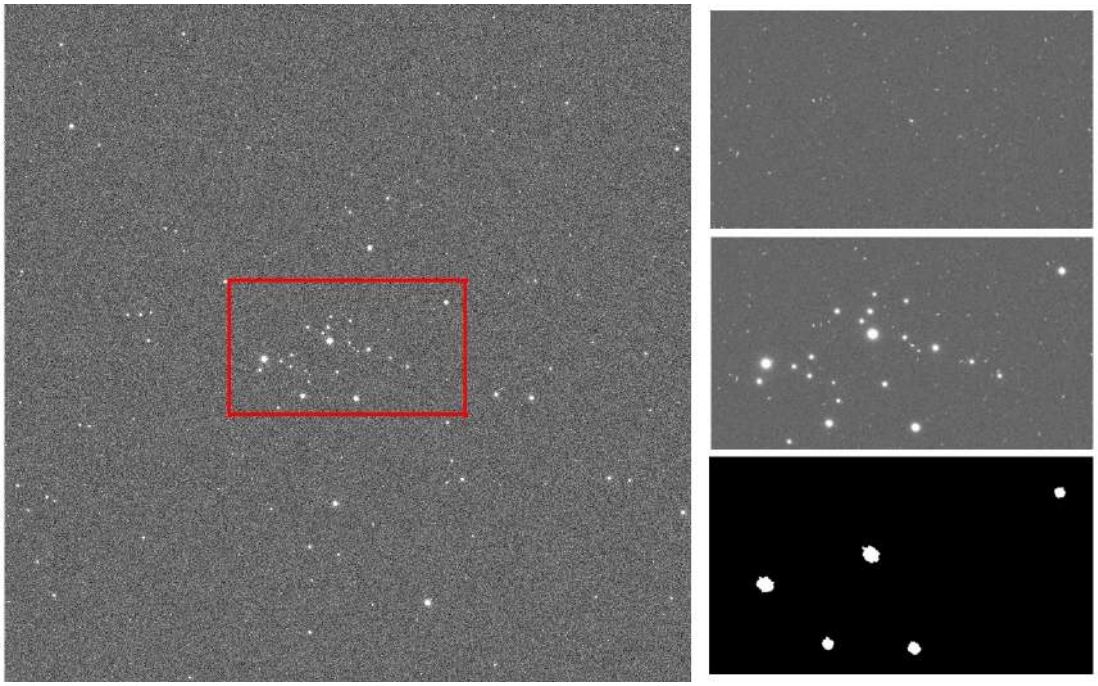

Figure 3.14: Example image of a simulated cluster at $z = 0.72$. A cut-out of the full image, shown in red, can be seen in the right for the simulations with background galaxies only (top), with added cluster members (middle) and showing the mask used to remove bright objects (bottom). The full image and cut outs spans $300'' \times 300''$ and $100'' \times 55''$, respectively.

them separately, and not include them in the simulations that are used in Sect. 3.3.2 to investigate the impact of nearby fainter galaxies and selection effects. Note that we verified that the presence of bright galaxies does not lead to a significant shift in the estimates of selection bias for our method. We do account for it, however, as a nuisance parameter in the final summary of the bias in Sect. 3.4.

3.3 Impact of faint galaxies

In Sect. 3.1 the analysis was obtained with isolated galaxies, situated on a grid. For a slightly more realistic scenario in Sect. 3.2, we discussed the addition of bright cluster members to the simulations. But in both cases, no light contamination from faint neighbours was accounted for. When two galaxies are completely blended in our images they are fully removed from the analysis (if the PSF convolution does not make them look like just one galaxy) and should not impact the results. Neighbouring galaxies (cluster or field) which are not blended but close to the background galaxies, are generally not selected when computing our shear estimates to avoid lensing dilution through the colour selection that was explained in Sect. 2.3.4. However, even when removed from the source sample, they can introduce some light contamination that may affect shape measurements for our faint source population which are present in

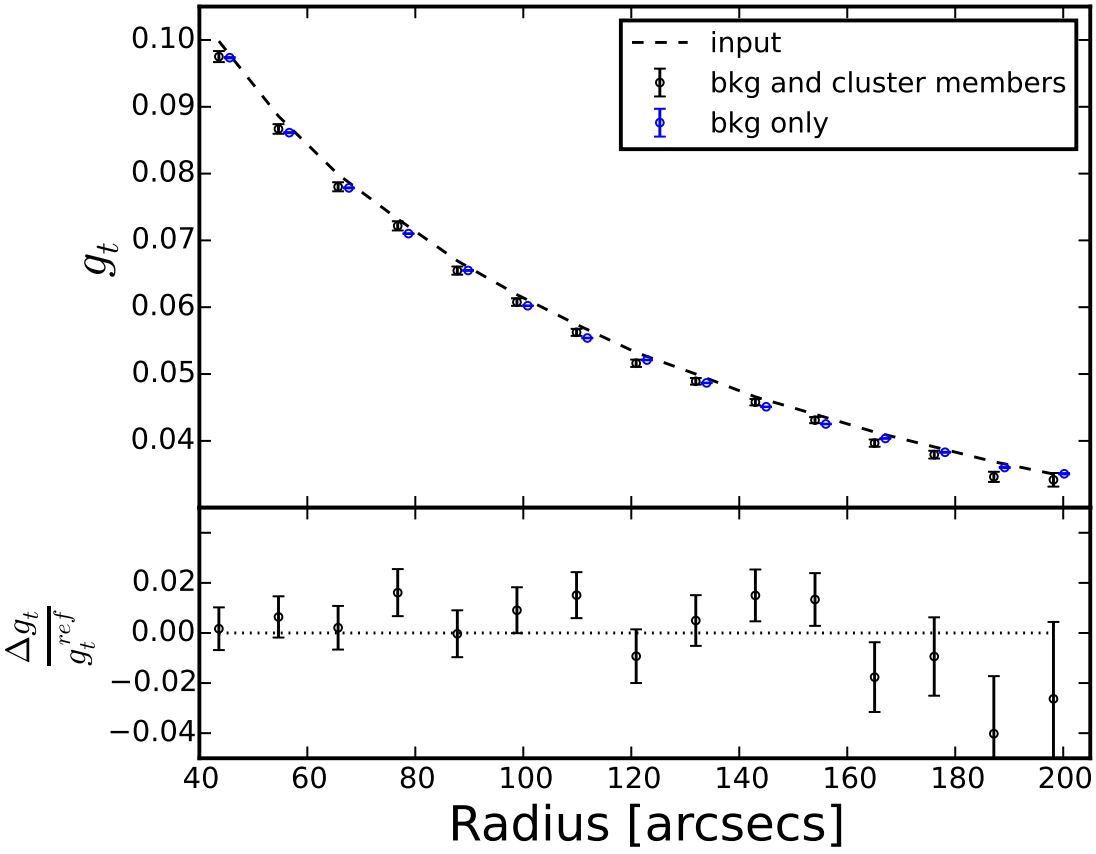

Figure 3.15: Measured clustering of multiple simulations of background galaxies sheared following an NFW profile with (in black) and without (in blue) the presence of cluster member galaxies for all stacked clusters which are $z > 0.7$. The dashed line represents the input profile. On the bottom panel we see the difference between the tangential shear of the simulations with and without cluster member galaxies as a function of radius.

the analysis. Hoekstra et al. (2017) and Euclid Collaboration et al. (2019) demonstrate that faint sources below the selection threshold affect shape measurements. Using a Euclid-like setup selecting galaxies with $i < 24.5$ and accounting for realistic galaxy and clustering properties calibrated using Hubble Ultra Deep Field data (HUDF, Beckwith et al. 2006), Euclid Collaboration et al. (2019) show that these faint sources cause an additional shape measurement multiplicative bias for our KSB+ implementation of $\Delta m = -0.0149 \pm 0.0002$. As another example, for deep optical data with ground-based resolution Mandelbaum et al. (2018a) found that the impact of nearby galaxies may affect the shape calibration at the $\sim 10\%$ level. Similarly, for the Dark Energy Survey Samuroff et al. (2018) found that neighbours can affect multiplicative biases by $3 - 9\%$. In our pipeline, to be conservative, we use masks to remove bright and extended objects and additionally apply a neighbour rejection which reduces the impact of neighbours. If two galaxies are detected in the catalogue with a

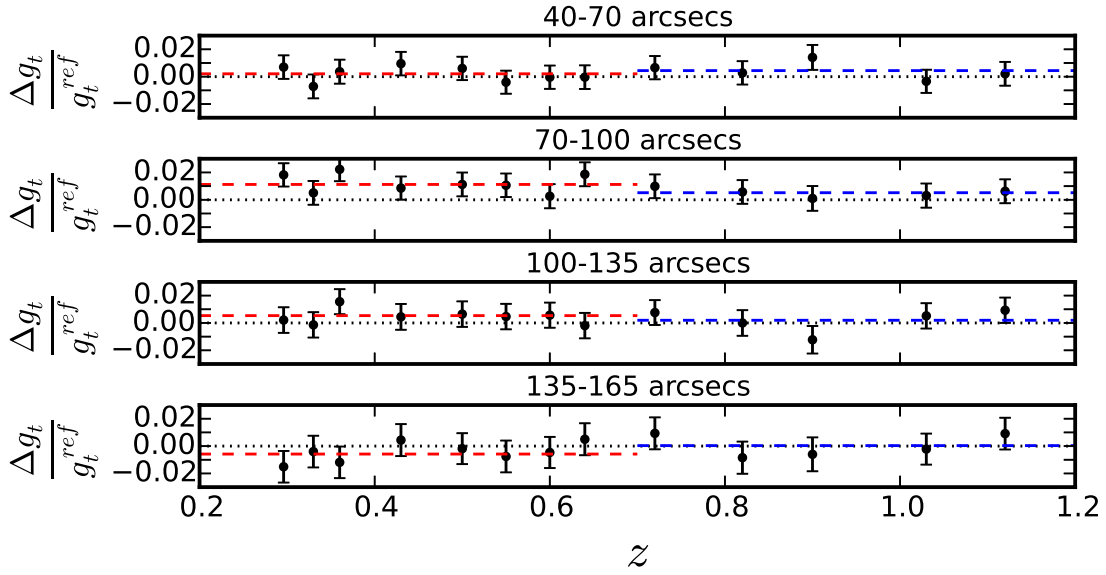

Figure 3.16: Difference of the tangential shear of the simulations with and without cluster member galaxies as a function of cluster redshift in three cluster-centric distance bins. The four panels show the values at different distance bins. The dotted black line represents the zero for reference and the dashed lines shows the mean of the points. Red is for clusters $z < 0.7$ and blue for $z > 0.7$.

separation $< 0.''75$ we only keep the brighter one. We expect that this, together with the fact that we are simulating high resolution data, reduces the impact of neighbours, compared to previous works, but we test it here nevertheless.

In order to study a more realistic scenario where galaxies suffer from blending and neighbouring effects, we created simulations using the real position and magnitudes of the galaxies. We used catalogues from the CANDELS fields (Skelton et al. 2014), which are complete up to just below 27.5 in the F606W filter, which is roughly one magnitude deeper than our mock galaxies. This allows for a estimation of the impact of faint galaxies, which are undetected but still present in the images. Following their real positions, as opposed to randomly placing galaxies is important as it captures the clustering which happens in the Universe. We used different patches of each CANDELS field to act as a different realization of the positions and magnitudes. An example of a cut-out of the same region of the GOODS North field in the real images and in our simulations is shown in Fig. 3.17. The sizes and ellipticities differ, but the positions and magnitudes are comparable. Some objects vary since we use a NIR-detected catalogue (in the F160W filter), but we are simulating F606W images. This means that some of the galaxies will be missing from our simulations as they are not detected in the F160W images. When creating the mock images, for the galaxies that are within our colour cuts ($V_{606} - I_{814} < 0.4$) and magnitude range ($V_{606} < 26.5$), we store their positions in order to later select them for our analysis. This guarantees that the galaxies used for the shear estimation are indeed similar to what is used in real images. Fainter

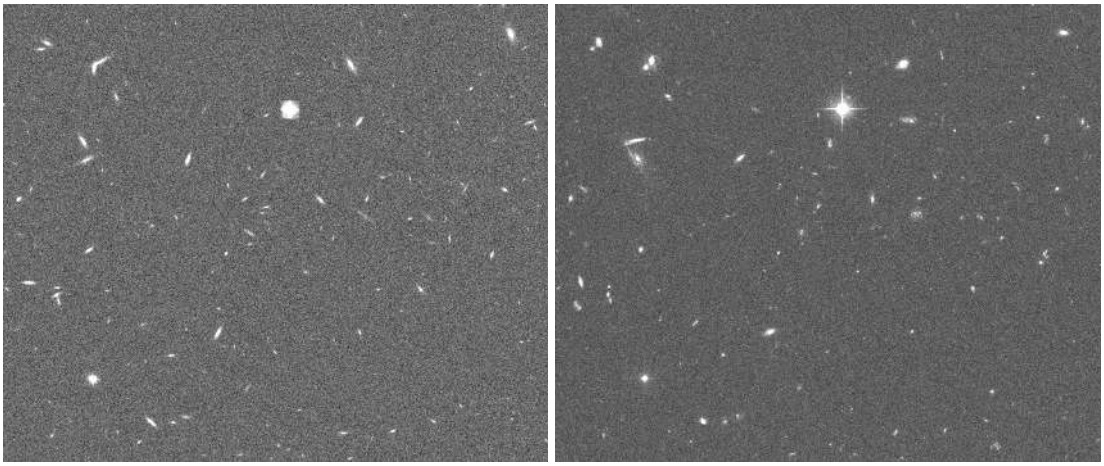

Figure 3.17: Comparison between the simulated images from GOODS North (left) and the real images (right). The sizes and ellipticities are different between them as we use a different catalogue for them in the simulations. The missing galaxies are caused by the CANDELS detection band, which is not F606W, but F160W.

galaxies are also included in the simulation as present in the Skelton et al. (2014) catalogue. Importantly this catalogue is deeper than the single-orbit depth shape catalogue from S18a, which was used to define the inputs for the simulations described in Sect. 3.1. As a result, this reduces the incompleteness in the input catalogue, leading to a better match in the recovered distributions between the simulation analysis and the CANDELS analysis, especially in terms of $S/N_{\rm flux}$ (compare Figs. 3.1 and 3.20). The rest of the galaxy properties follows the same procedure described before in Sect. 3.1, so any changes come from the blending effect. As mentioned before, we do not include here the effect of bright galaxies from Sect. 3.2 given the dependence on cluster redshift. Instead, we will compute the resulting net bias for the correction of the real data in Sect. 3.4, adding all the different contributions.

With this analysis setup we find a small $\sim -0.7\%$ shift in the multiplicative bias due to the use of realistic positions compared to the grid-based analysis, which is consistent with what was found in Kannawadi et al. (2019). They found around a 1% change when including the proper clustering of galaxies. This however still lacks the impact of selection bias and very faint $V_{606} > 27.5$ galaxies, which are accounted for in the following subsections.

While the effect of neighbours has a relevant impact on our analysis, its impact is at a much smaller level than what was found in previous work (Mandelbaum et al. 2018a) for ground-based images. This is likely due to the better resolution of the HST images, leading to a weaker impact of the blending and neighbours or to the more stringent neighbour rejection.

3.3.1 Selection bias

Weak lensing is based on the assumption that the orientation of the intrinsic ellipticity of the galaxies is random and any preferential direction we find for the galaxy ellipticity is caused

by lensing. If this assumption is broken because we preferentially select galaxies aligned with, or orthogonally to, the shear direction, we introduce a selection bias into our measured sample. This means that we measure a different value for the shear simply because of the galaxies that are selected for the analysis. It modifies the measured shear (Heymans et al. 2006) and subsequently the mass estimation so it is important to understand this effect in order to obtain accurate results.

The selection bias can come from different sources and in this section we aim to disentangle the different steps in the shape analysis and their impact in the bias determination. In the previous sections the selection bias has been neglected as we required matched pairs with opposite intrinsic ellipticities, which artificially removed any preferential selection. This was acceptable for the previous sections as the selection bias for the galaxies placed on a grid is expected to be small due to the fact that the largest contribution comes from neighbouring galaxies. This is discussed at the end of this section where we compute selection bias for different simulation setups. However, selection bias can be important (e.g. Kannawadi et al. 2019). For this reason we present here a step-by-step analysis of the selection bias alone before obtaining in Sect. 3.3.2 a joint estimation of the residual bias and the selection bias, as well as their joint signal-to-noise ratio dependence. We estimated the impact of selection bias by computing the average intrinsic ellipticity for the galaxies that are present in the final catalogues. This can only be done when we are working with simulations since we know the input (or "true") ellipticity for each galaxy before they are sheared and we can use that to compute any preferential alignment that could arise. In the real images, we can only obtain the final measured ellipticity which is a combination of intrinsic ellipticity, shear and the measurement biases, so it is impossible to disentangle and know if any remaining ellipticity after averaging comes from the selection bias or from the weak lensing shear. This is why simulations are critical for this analysis. Any deviation on the mean intrinsic ellipticity from zero indicates a preferential selection of galaxies.

The process to test it is simple. We selected the galaxies that were used for the final computation of the average ellipticity in our simulation and look up their intrinsic ellipticities used as input in the simulation creation. If we treat the ellipticities as complex number (e) as well as the shear (g), the true intrinsic ellipticity for each galaxy is computed as (Bartelmann & Schneider 2001)

$$e_{\text{true}} = \frac{e - g}{1 - g^* e}, \tag{3.4}$$

where * indicates the complex conjugate. Unlike what we did when estimating the residual bias, we do not require detection in both the normal image and the rotated one, since this is not what happens in real images. Both normal and rotated images are still included in order to cancel shape noise for the galaxies detected in both (these galaxies do not contribute to the selection bias), tightening the constraints. We compared the average input ellipticity independently for each input shear and fitted a linear relation in order to constrain the shear dependence (see Fig. 3.18). This bias can be introduced in different parts of our analysis pipeline which motivated a measurement of the selection bias after each step of the pipeline. These are described below and summarized in Table 3.9.

Selection bias is heavily influenced by the neighbouring galaxies. In particular, the SExtractor selection bias is expected to depend on the galaxy blending and neighbour contamination. It is for this reason that we estimate the selection bias in this section with the more realistic galaxy positions.

SExtractor object detection

SExtractor is used for the object detection and creation of a catalogue. A Gaussian smoothing is used in its calculations, and we expect the shapes of galaxies to have a large impact in their likelihood to be selected. We note here the most important setting for our SExtractor detection, following the work in S18a, which are FILTER_NAME= gauss_2.5_5x5.conv, DETECT_THRESH=1.4, DETECT_MINAREA=8, DEBLEND_NTHRESH=32, and DEBLEND_MINCONT=0.01. Looking at the intrinsic input ellipticity of the galaxies that are present in our SExtractor catalogues, we can see which types of galaxies are rejected.

We find a large selection bias of

$$\begin{aligned} m_{1,\mathrm{sel}} &= -0.0291 \pm 0.0015, \\ m_{2,\mathrm{sel}} &= -0.0266 \pm 0.0018. \end{aligned} \tag{3.5}$$

This is comparable with what was found in Kannawadi et al. (2019), where they also found a large selection bias coming from SExtractor detection only. This effect does not depend on the actual shear measurement algorithm, since it happens before the shear is estimated, directly from the SExtractor object detection. It is therefore a more general issue that can be present in all shear calibration and weak lensing mass determination studies. The negative nature of this selection bias, indicates that round galaxies are more likely to be detected, most likely due to the isotropic kernel, with which the image is convolved during the SExtractor detection phase. However, other factors such as the deblending can also be part of the reason.

S/N_{flux} cut

We introduce a cut on signal-to-noise, in order to have robust bias estimations. Following previous work, it is typical to select galaxies with $S/N_{\mathrm{flux}} > 10$. The rejection of many galaxies according to their signal-to-noise, might also remove certain galaxy shapes more frequently. This preferential selection may introduce additional selection bias. We see a selection bias after the signal-to-noise ratio cuts of

$$\begin{aligned} m_{1,\mathrm{sel}} &= -0.0259 \pm 0.0020, \\ m_{2,\mathrm{sel}} &= -0.0259 \pm 0.0014. \end{aligned} \tag{3.6}$$

We should note that since the cuts are performed after the object detection, the selection bias is cumulative. It indicates that our signal-to-noise ratio cut actually has a positive bias which partially corrects from the bias in the SExtractor object detection. This change is marginal, however, which indicates that the exact cuts we apply will not change the selection

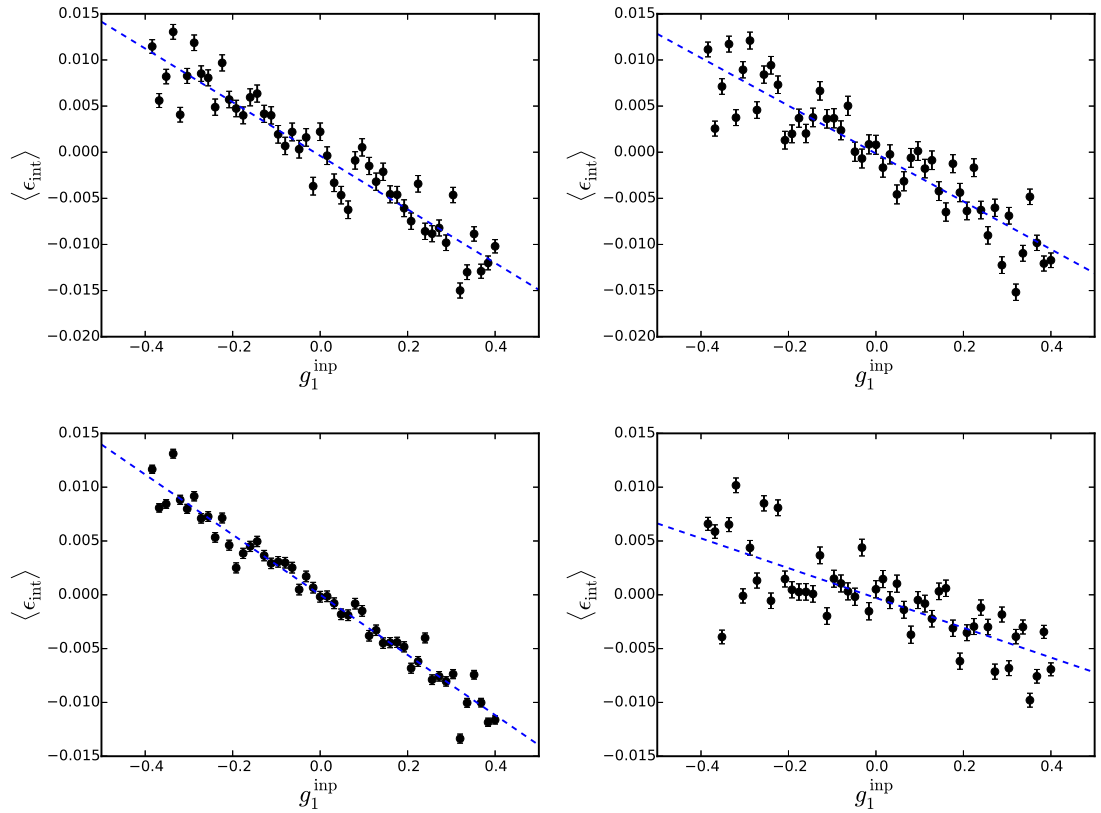

Figure 3.18: The selection bias for the first shear component. We compare the residual input ellipticity of the galaxies after every step in the pipeline. We see selection bias after the `SExtractor` object detection on the top left, after the $S/N_{\rm flux} > 10$ cuts in the top right, after the neighbour rejection in the lower left and after the final KSB+ catalogues in the lower right. The black points are the estimated bias as a function of shear and the blue dashed line is a linear fit, whose values can be seen in Table 3.9.

bias meaningfully. In fact, for the alternative cut of galaxies we also use in this work, of $S/N_{\rm flux} > 7$ we obtain

$$\begin{aligned} m_{1,\rm sel} &= -0.0279 \pm 0.0010, \\ m_{2,\rm sel} &= -0.0266 \pm 0.0010, \end{aligned} \tag{3.7}$$

which is only marginally different.

Rejection of very close neighbours

As part of the KSB+ shape measurement, we perform a selection of objects which do not have a bright close neighbour, in order to partially remove possible contamination coming

from the presence of neighbours. This means that we reject galaxies which have a bright object closer than $0\farcs75$. This, however, can also introduce an additional bias if the intrinsic ellipticity of the galaxies is aligned in the direction of their close neighbours. We measured this effect to be

$$\begin{aligned} m_{1,\mathrm{sel}} &= -0.0211 \pm 0.0071, \\ m_{2,\mathrm{sel}} &= -0.0194 \pm 0.0056, \end{aligned} \tag{3.8}$$

for the $S/N_{\mathrm{flux}} > 10$ and

$$\begin{aligned} m_{1,\mathrm{sel}} &= -0.0245 \pm 0.0062, \\ m_{2,\mathrm{sel}} &= -0.0239 \pm 0.0050, \end{aligned} \tag{3.9}$$

for the $S/N_{\mathrm{flux}} > 7$ galaxies. This means that this step also partially corrects for the original bias. However, it is important to note that the rejection of galaxies increases the uncertainty on the selection bias estimation.

Final catalogues after KSB+ cuts

Another step of the shape measurement algorithm introduces cuts such as $S/N_{\mathrm{KSB}} > 2$ and FLUX_RADIUS < 7, in order to robustly measure the shear. This can also modify the selection bias and is studied here.

The results show that there is a selection bias on the final catalogues of

$$\begin{aligned} m_{1,\mathrm{sel}} &= -0.0138 \pm 0.0021, \\ m_{2,\mathrm{sel}} &= -0.0174 \pm 0.0013, \end{aligned} \tag{3.10}$$

for a cut on $S/N_{\mathrm{flux}} > 10$. This is much smaller than the original `SExtractor` object detection bias, which means that the extra cuts and selections we apply to our galaxy population after the `SExtractor` detection actually partially correct for the preferential selection of galaxy shapes happening at the detection step. It is still important to account for it in our analysis, nevertheless so in the next section, we perform a joint analysis of the residual and selection bias to check how naive the independent study of both is.

For the case when $S/N_{\mathrm{flux}} > 7$ we obtain a final selection bias estimate of

$$\begin{aligned} m_{1,\mathrm{sel}} &= -0.0150 \pm 0.0018, \\ m_{2,\mathrm{sel}} &= -0.0180 \pm 0.0012, \end{aligned} \tag{3.11}$$

which, again, is only marginally larger. The signal-to-noise ratio cuts do not seem to play a large role in this effect.

Table 3.9: Selection bias after each step in the analysis pipeline for two $S/N_{\rm flux}$ cuts. Note that the first step is the pipeline happens before any signal-to-noise cuts and therefore the selection bias is the same in both cases.

	$S/N_{\rm flux} > 10$		$S/N_{\rm flux} > 7$	
Step	Δm_1	Δm_2	Δm_1	Δm_2
`SExtractor` detection	-0.0291 ± 0.0015	-0.0266 ± 0.0018	-0.0291 ± 0.0015	-0.0266 ± 0.0018
$S/N_{\rm flux}$ cuts	-0.0259 ± 0.0020	-0.0259 ± 0.0014	-0.0279 ± 0.0010	-0.0266 ± 0.0010
Neighbour rejection	-0.0211 ± 0.0071	-0.0194 ± 0.0056	-0.0245 ± 0.0062	-0.0239 ± 0.0050
Final KSB+ catalogues	-0.0138 ± 0.0020	-0.0174 ± 0.0013	-0.0150 ± 0.0018	-0.0180 ± 0.0012

Influence of galaxy position on selection bias

We studied and compared two more scenarios where we computed the selection bias: the grid, and an adjustment of positions with shear. These are introduced to improve our understanding of how the selection bias behaves.

For the grid, we used the same setup as for the simulations in Sect. 3.1, and estimated the selection bias as was done in the rest of this subsection. We found only a small selection bias of $-0.9\% \pm 0.2\%$.

For the corrected positions, we used the CANDELS mocks with the real galaxy positions (see the beginning of this section) and adjusted the galaxy positions to be stretched according to the input shear. This is only a small correction which was not implemented in the original CANDELS mock simulations, as magnification was also not included. For it, we simply modified the original positions of the catalogues by the shear value as this is closer to the situation in real images. We expect that the selection bias has a weak dependence with this effect as `SExtractor` detection can be influenced by the positions of close neighbours. In fact, with the corrected position CANDELS mocks we observe a $-1.1\% \pm 0.5\%$ effect for the `SExtractor` object detection selection bias, which is smaller that what was found for the CANDELS-like setup without this position correction.

Surprisingly, the final catalogues, after all cuts have been applied, present a comparable selection bias in all setups. This seems to indicate that the intermediate steps account for such bias differences and therefore, the use of the corrected positions is not critical in the determination of the total selection bias.

3.3.2 Joint correction for shape measurement and selection bias based on the CANDELS-like simulations

The results in Sect. 3.3.1 show that selection bias is an important effect that can also have a weak signal-to-noise dependence, as the estimation for different cuts in the previous section showed. This dependence is expected to be indeed weak as the change in selection bias between both signal-to-noise cuts is small, but, nevertheless, for a robust bias estimation we should measure the residual multiplicative bias in a joint manner with the effect of selection bias. Because of this, we need the most realistic simulations in order to obtain a robust estimation of the multiplicative bias that we use to correct the real analysis as well as its

signal-to-noise dependence since the distribution of the galaxy properties are affected by the addition of faint neighbours.

In this section we present a joint measurement of the multiplicative bias and the selection bias for our most realistic simulation using the CANDELS positions and magnitudes. These two effects should not be separated as they can interact with each other. This is done by not requiring any matched pairs for the analysis and just using all galaxies in the final obtained catalogues. This is the situation we have in the real images, as they do not have any rotated pairs. Furthermore, the $S/N_{\rm KSB}$ dependence of the two should be studied and compared to the dependence we showed in Fig. 3.2. A combined analysis of both effects in 10 $S/N_{\rm KSB}$ bins is shown in the upper panel of Fig. 3.19. The estimates are more noisy in this case, than the signal-to-noise dependence obtained in Sect. 3.1 since using matched pairs before reduced the shape noise, which is not done here. This is the reason that we reduced the number of bins here, compared to Fig. 3.2. We see a very similar behaviour on the $S/N_{\rm KSB}$ which indicates that we can simply maintain the same correction, applying a shift coming from the measured residual bias. In any case, any remaining discrepancies are not critical due to the good matching of the $S/N_{\rm KSB}$ between the simulations and the real data. Having a realistic galaxy population means that the same systematics we have in our mocks are also present in the real galaxy catalogues and it is not critical if the correction does not follow the dependence exactly, as the residual bias should account for it. This would not be the case for very different galaxy populations which may have a different distribution of signal-to-noise for the galaxies.

To understand how similar our mock galaxies are to the real objects, we again show a comparison between the measured properties of the real galaxies on CANDELS and the measured properties of our mock galaxies (this time following the real positions) in Fig. 3.20. Despite using the same inputs as in the grid simulations except the positions and magnitudes, the distributions are now slightly different. This can be partially explained because the use of the Skelton et al. (2014) catalogue for the magnitudes means that we have a deeper catalogue than the single-orbit depth shape catalogue from S18a used for the grid simulations in Sect. 3.1. This reduces the incompleteness in the input catalogue, which can explain the better match in the recovered distributions between the mock and real galaxies, especially in terms of $S/N_{\rm flux}$ (see Fig. 3.1). Furthermore, the real catalogues we are comparing to, have the effect of neighbours, which was removed in the grid simulation. The more realistic scenario now should give a better match to the real catalogues.

For the real image analysis we will then use the following correction (computed for $S/N_{\rm flux} > 7$ galaxies):

$$\begin{aligned} m_{\rm 1corr} &= -0.358 \left(S/N_{\rm KSB}\right)^{-1.145} - 0.042, \\ m_{\rm 2corr} &= -0.357 \left(S/N_{\rm KSB}\right)^{-1.298} - 0.039. \end{aligned} \tag{3.12}$$

Using this correction we obtained a small residual bias shown in Table 3.10, which contains the effect of the addition of faint galaxies as well as the selection bias.

In the lower panel of Fig. 3.19 we show the dependence of the bias on the FLUX_RADIUS

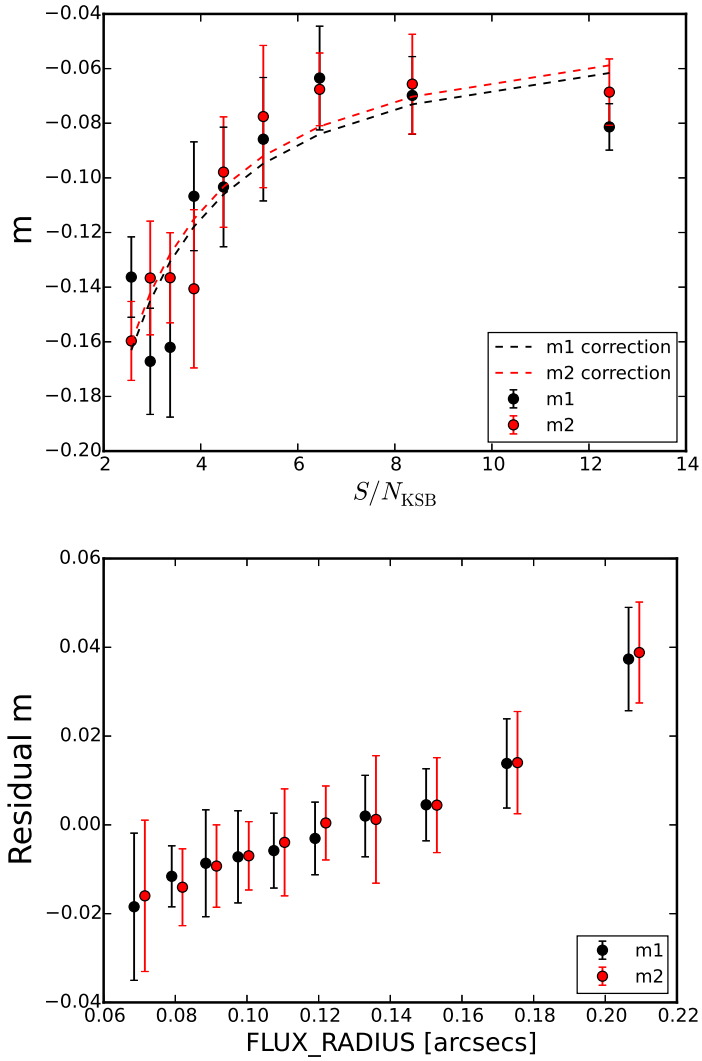

Figure 3.19: *Upper*: Dependence of the bias on $S/N_{\rm KSB}$ computed without correction or matching pairs on the CANDELS-like simulations which accounts for the selection bias. The dashed lines correspond to the correction from Eq. (3.12) for each component. *Lower*: Dependence of the residual bias on the FLUX_RADIUS estimated from the CANDELS-like simulations. We have applied the $S/N_{\rm KSB}$-dependent correction from Eq. (3.1) plus a constant offset that corresponds to the mean bias measured in the CANDELS-like simulations. The second component is slightly shifted for visualization purposes.

after the $S/N_{\rm KSB}$-dependent correction in Eq. (3.12). We find a stronger dependence on FLUX_RADIUS when they suffer from the addition of faint galaxies (compare Fig. 3.7). This strong dependence of the bias on the sizes of galaxies is a bit worrying, but should not be critical as long as we have a good representation of the real sizes of galaxies in our mocks.

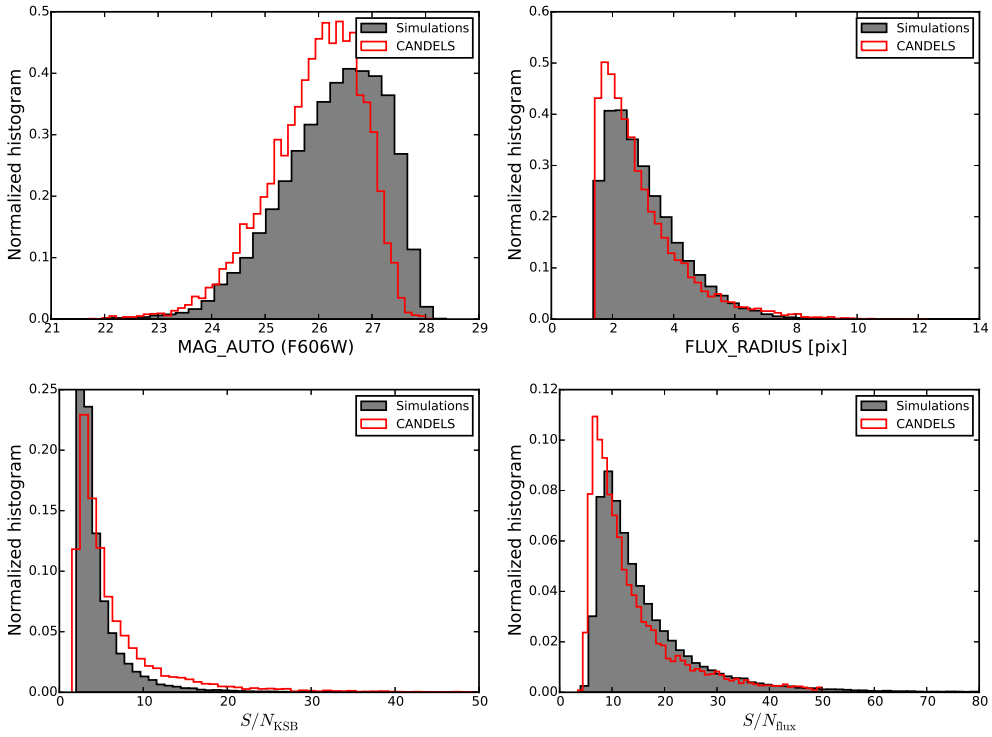

Figure 3.20: Comparisons between the measured distributions in our CANDELS-like simulations and the KSB+ CANDELS distribution for the F606W magnitudes, the half-light radius, the KSB signal-to-noise ratio $S/N_{\rm KSB}$, and the `SExtractor` signal-to-noise ratio $S/N_{\rm flux}$.

Table 3.10: Residual multiplicative bias for the different $S/N_{\rm flux}$ cuts in the CANDELS-like simulations after the correction from Eq. (3.12).

	m_1	m_2
$S/N_{\rm flux} > 10$	0.0010 ± 0.0040	-0.0023 ± 0.0043
$S/N_{\rm flux} > 7$	-0.0032 ± 0.0049	-0.0047 ± 0.0045

To make sure this is the case we remeasured the size distribution compared to the real data and performed a reweighting of the bias. We found that the small discrepancies on the size distribution only lead to a $\sim -0.3\%$ change in the bias.

We chose to consider the CANDELS-like setup as the most realistic simulations because it includes the real positions of galaxies. However, the catalogues come from field images, which do not have bright cluster members as we do in our cluster images. In Sect. 3.2, we studied this effect separately and found it to be almost negligible. Furthermore, the redshift dependence motivated us to not include it in our final simulations in order to not particularize the results too much as we would need simulations for each redshift that we want to apply the corrections to. We also studied the selection bias dependence on the addition of cluster

members and found it to be non-existent. All this, motivated us to keep that analysis separated from the results presented in this section. Nevertheless, in the final estimation of the bias, we include its impact (see Table 3.12) for the residual bias we use to correct the weak lensing analysis in Chapter 5.

3.3.3 Addition of faint galaxies following Euclid Collaboration et al. (2019)

Despite our consideration of the CANDELS-like simulations as the most realistic setup, Sect. 3.3.2 only accounts for galaxies that are 1 magnitude fainter than our source galaxies. In this section, we wanted to include a crude estimate of the full impact of faint galaxies for the grid simulations (from Sect. 3.1) that are undetected but present in the images following the setup discussed in Euclid Collaboration et al. (2019). They used a brighter population of galaxies than we have in this work ($i < 24.5$) and obtained $\Delta m = -0.0084 \pm 0.0002$ if source clustering is ignored, and $\Delta m = -0.0149 \pm 0.0002$ with the impact of source clustering. The introduction of a realistic clustering of galaxies can greatly change the bias and this setup serves as a test of the realism of the CANDELS-like simulations in the previous section. However the results in Euclid Collaboration et al. (2019) cannot be directly applied here so we used their same setup modifying it for the different galaxy population. Since we have deeper images for our cluster studies and the simulations presented here reach $i < 28$, we expect that the contribution of the clustering of galaxies of similar magnitude is more important than for brighter samples. In order to test this, we include the effect of faint neighbouring galaxies to our grid simulation using the Hubble Ultra Deep Field (HUDF, Beckwith et al. 2006) to obtain the faint galaxy properties.

We created two different simulation setups. Both have a population of bright galaxies with magnitude $V_{606} < 26.5$ and colours $V_{606} - i_{775} < 0.3$. This is a slightly different colour selection that what was used in Sect. 3.1, but the differences are not critical for the results presented here. A population of fainter galaxies which are clustered around the brighter galaxies is included. The difference between the two simulation setups is the magnitude up to which we include these faint galaxies. For the first case, we follow the work in Euclid Collaboration et al. (2019) and include up to two magnitudes deeper than the galaxies we use in our shear analysis, which should account for the full effect that faint neighbours have in the bias. This means that we simulate galaxies until $V_{606} = 28.5$. We find a $\sim -1.6\%$ change in the multiplicative bias when including this effect, if we compare it to the grid-only simulation.

The second setup, is almost identical, but we only include 1 magnitude fainter than our $V_{606} < 26.5$ cut. This allows us to already study the contribution of galaxies of similar magnitude to the galaxies we use in our shear estimates, and to compare to the results in Sect. 3.3.2. Since the CANDELS fields are only complete up to a roughly 1 magnitude deeper than our source population, the setup in Sect. 3.3.2 can be compared to the results from this section, with galaxies up to $V_{606} < 27.5$. We obtain a $\sim -1.1\%$ shift in bias compared to the grid only simulation and consistent results with what was obtained from the CANDELS-like

Table 3.11: Residual multiplicative and additive bias for the contribution of faint neighbours of the galaxies on a grid after a $S/N_{\rm flux} > 10$ cut and a $S/N_{\rm flux} > 7$ cut. We applied the $S/N_{\rm KSB}$-dependent correction from Eq. (3.12) and computed it over the unmatched pairs to account for selection bias. We show the results with the inclusion of faint galaxies with two different magnitude limits.

Cuts	Sample	m_1	c_1	m_2	c_2
			$[\times 10^3]$		
$S/N_{\rm flux} > 10$	$V_{606} < 27.5$	-3.8 ± 4.4	-2.7 ± 0.8	-2.2 ± 5.0	-3.0 ± 0.6
	$V_{606} < 28.5$	-7.5 ± 5.5	-2.9 ± 0.7	-8.2 ± 6.5	-2.9 ± 0.6
$S/N_{\rm flux} > 10$	$V_{606} < 27.5$	-6.6 ± 3.0	-4.0 ± 0.7	-7.8 ± 2.5	-4.4 ± 0.7
	$V_{606} < 28.5$	-12.7 ± 4.6	-3.9 ± 0.5	-14.8 ± 4.1	-3.1 ± 0.6

simulation. This is an indication that indeed the CANDELS-like setup partially accounts for the effect of faint undetected galaxies as we obtained comparable shifts in the bias.

In Table 3.11, we show the bias estimation of both setups, computed without the need for matched pairs in order to account for the selection bias. We have applied the final $S/N_{\rm KSB}$-dependent correction from Eq. (3.12), which already partially accounts for the effect of faint galaxies, hence why the residual bias is small. This serves as a comparison between the CANDELS-like simulations and the setup presented here following Euclid Collaboration et al. (2019). The main difference between both is the fact that here we have a very idealistic case. All bright galaxies are part of our source population, colour-selected and with the right sizes and signal-to-noise ratio. In the CANDELS mock simulations, we have a large number of galaxies which do not belong to our source population, due to their colour or magnitude, but can still contaminate the results. We find very consistent results for the setup with galaxies $V_{606} < 27.5$. The slightly smaller bias measured for the real positions and magnitudes in the CANDELS-like simulations can be because the completeness of the CANDELS catalogues is marginally below $V_{606} = 27.5$, but also from the contamination of other sources, which are not part of our source population or the faint background galaxies, which may introduce a positive bias. Assuming the most realistic galaxies as the CANDELS-like simulations in Sect. 3.3.2, we account for the full contribution of the faint galaxies (which is lacking on that setup) adding the difference between the simulations in this section with $V_{606} < 27.5$ and $V_{606} < 28.5$, in the final estimation of the bias in the next section.

Comparing the results with the work in Euclid Collaboration et al. (2019), we see that the results agree if we account for the difference in the source population. Both results indicate a large contribution to the shear bias comes from faint neighbouring sources. We also see that already the presence of galaxies with similar magnitudes to our source population have a large influence in the bias estimates and it is important to account for it. This is why it is not so critical to add the full contribution in the creation of the most realistic simulations, and only use the real CANDELS catalogues.

3.3.4 Selection bias caused by the addition of cluster members

We have seen the importance of including selection bias and how our bias estimates change when we neglect it due to the use of matched pairs. Because of this, in this section we revisit the analysis already discussed in Sect. 3.2 and study how much selection bias changes due to the addition of bright cluster members in our simulations. This is computed in a similar manner as in Sect. 3.3.1, for both the reference background-only simulation and the background+cluster members simulation. Fig. 3.21 shows the difference in the selection bias for the simulations with cluster members and the background-only simulations as a function of cluster-centric distance. This is shown for $S/N_{\rm flux} > 7$ galaxies and clusters $z > 0.7$. An average estimation of the selection bias change yields $0.85 \pm 0.24\%$ for clusters at all redshifts, which is reduced to $0.60 \pm 0.29\%$ when we consider $z > 0.7$ clusters only. These estimates are computed for $S/N_{\rm flux} > 7$ galaxies. For the more restrictive case of $S/N_{\rm flux} > 10$ galaxies, we obtain 0.0053 ± 0.0019 for clusters at $z > 0.7$. This contribution is significant, and is added to the total residual bias estimation in Sect. 3.4. However, please note that it is redshift dependence, which again, is the reason not to include this cluster effect in the most realistic CANDELS-like simulations.

3.4 Summary of the bias estimates

Throughout this chapter we have discussed different ingredients that affect the estimation of the residual multiplicative bias as well as the signal-to-noise-dependent corrections. As a summary, we present a final combined estimation of the bias in Table 3.12, which can be applied to weak lensing studies of galaxy cluster as it is done in Chapter 5. This is separately computed in the shear range $|g| < 0.2$ for the two ellipticity components as well as for two signal-to-noise cuts, $S/N_{\rm flux} > 10$ and $S/N_{\rm flux} > 7$.

We start with the most realistic simulations, discussed in Sect. 3.3.2, where we obtained the residual bias after the $S/N_{\rm KSB}$-dependent correction for the CANDELS-like simulations (Eq. 3.12). As it is computed without the matched pairs, it includes the selection bias as it was discussed in Sect. 3.3.2. Due to the fact that the CANDELS-like simulations only partially include the influence that faint undetected galaxies have on the bias estimates, we include in Table 3.12 the change in bias due to the addition of galaxies up to 2 magnitudes fainter than the source population, when comparing to adding 1 magnitude fainter only. This was already discussed in Sect. 3.3.3. Finally, we add the impact of bright cluster members from Sect. 3.2, for clusters at $z > 0.7$, both coming from the change on the residual (Sect. 3.2) and on the selection bias (Sect. 3.3.4), which are presented in Table 3.12 as two different contributions. All these different contributions are mimicking effects that are also in the real data, and account for the final residual multiplicative bias.

Furthermore, due to the large differences in the measured bias based on small changes in the creation of the simulated images, we add extra uncertainties in order to fully capture our confidence in the results presented in this work. From the selection of the PSF model (see Sect. 3.1.7), we estimate half of the difference between the bias obtained when using a

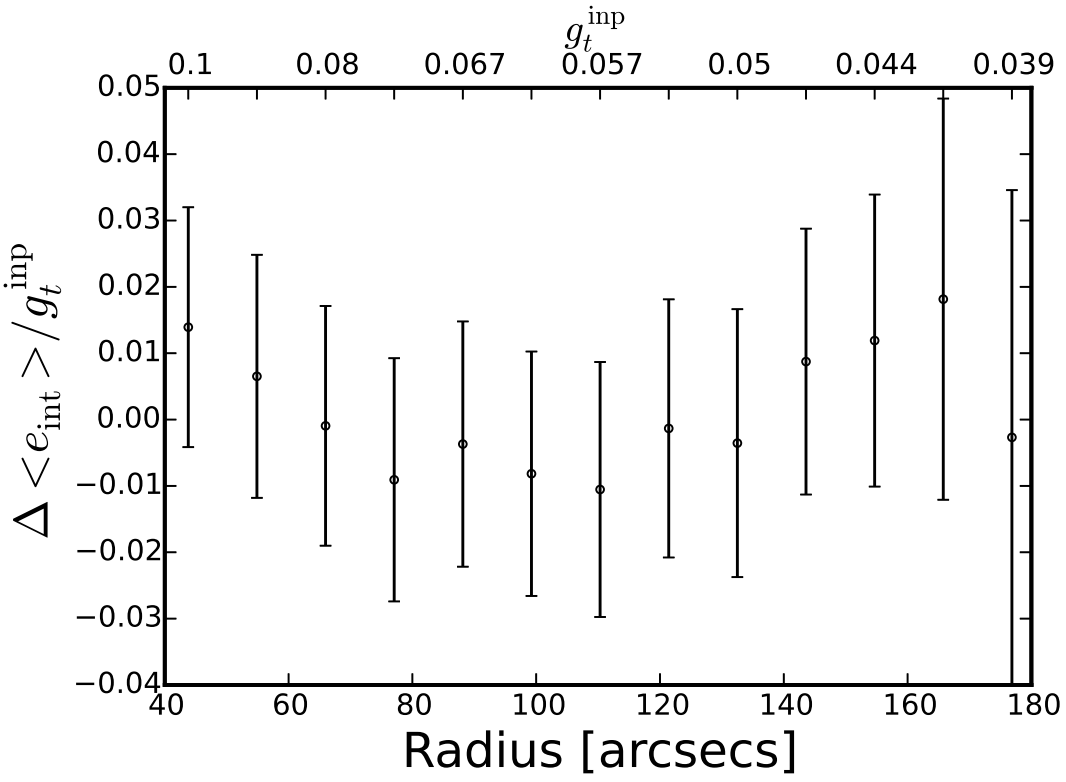

Figure 3.21: Relative difference in the selection bias estimates for the background only and the background+cluster members simulations for clusters $z > 0.7$ and $S/N_{\rm flux} > 7$ galaxies.

Table 3.12: Summary of the contribution of the bias from the different effects for the two $S/N_{\rm flux}$ cuts used in this paper. We present a separated bias for each component for all except for the light contamination due to bright galaxies since that is calculated with the tangential shear, which depends on both components. The modelling errors include the uncertainties due to PSF models and the galaxy light uncertainties.

	$S/N_{\rm flux} > 10$		$S/N_{\rm flux} > 7$	
	m_1	m_2	m_1	m_2
	[$\times 10^3$]			
Residual bias	1.0 ± 4.0	-2.3 ± 4.3	-3.2 ± 4.9	-4.7 ± 4.5
Extra faint $V_{606} > 27.5$ galaxies	-3.7 ± 5.5	-6.0 ± 6.5	-6.1 ± 4.6	-7.0 ± 4.1
Cluster galaxies ($z > 0.7$): Shape bias	4.8 ± 3.8		2.5 ± 4.0	
Cluster galaxies ($z > 0.7$): Selection bias	5.3 ± 1.9		6.0 ± 2.9	
Other modelling uncertainty	± 12.8	± 13.0	± 12.6	± 13.1
Total residual bias + uncertainty	7.4 ± 15.1	1.7 ± 15.7	-0.8 ± 15.1	-3.2 ± 15.3

realistic ACS PSF and the more unrealistic Moffat PSF. Those differences can be seen in Table 3.6. We consider only half of the difference because the use of a Moffat PSF as a model for the HST/ACS PSF is not a realistic choice so using the full difference would be too conservative and not really represent the confidence we have in the simulations. Another source of uncertainty comes from the ellipticity changes on the PSF and how importantly this affects the bias. To account for small discrepancies in the PSF shape, we estimate half the difference between the bias for a circular PSF and when we introduce a 0.1 ellipticity. The final component of this extra uncertainty is a smaller contribution coming from the light profile used in the creation of the mock galaxies (see Sect. 3.1.5). For this, we assume the difference between the use of Sérsic index coming from parametric fits to real galaxies and the case for a flat distribution of the Sérsic index. Again, we do not use the more unrealistic case of a De Vaucouleur profile since this would artificially increase the bias uncertainties. The added uncertainties are shown in Table 3.12 under "Other modelling errors".

With all the different considerations for both the residual bias and the uncertainties, we obtain a final estimation of the bias of $m_1 = 0.0010 \pm 0.0150$, $m_2 = -0.0036 \pm 0.0156$ for $S/N_{\rm flux} > 10$ galaxies and $m_1 = -0.0068 \pm 0.0148$, $m_2 = -0.092 \pm 0.0150$ for $S/N_{\rm flux} > 7$ galaxies. The uncertainties are on the $\sim 1.5\%$ level. These estimates can be used to constraint the mass of galaxy clusters on future HST/ACS observations. In fact, the results obtained in this work have already been used in S20 to estimate weak lensing masses and in Chapter 5 in this work.

One of the main results to take away from this work on HST/ACS simulations is the importance of selection bias, and how simple approximations, such as requiring matched pairs, may no longer be a viable option for accurate and precise bias estimation. The use of grid simulations as we do at the beginning of this chapter, while useful for careful testing of the input parameters, does not provide a realistic scenario to obtain robust bias estimations. The separation of the different contributions may also not be as simple as is expected and more effort should be put into this for future work.

CHAPTER 4

Simulations for other telescopes

The results discussed in Chapter 3 were specifically tailored for simulated HST/ACS images with a detailed study on the input parameters in order to understand the general sensitivity of the bias to changes in the simulations. However, these results cannot simply be extrapolated to weak lensing analysis using different telescopes and instruments. Each telescope, camera and even filter we use has different properties that can influence the way we measure the galaxy shapes. Furthermore, the galaxy population we observe with each setup is not the same, which itself can introduce different biases.

In particular, HST is a space-based telescope that does not suffer from atmospherical distortions. The objects observed with HST appear quite sharp and this helps immensely in our task to determine their shapes. This makes the estimation of the galaxy ellipticity much easier and is the main reason why HST is so widely used for weak lensing analysis. However, observations with it are expensive and difficult to get. For this reason there is also a large number of studies using ground-based images for weak lensing. This increases the need for tailored simulations with the right properties, in order to test how the bias behaves for each setup as we expect them to have larger biases.

Schrabback et al. (2018b) (hereafter S18b) discusses a pilot study for cluster RCS2 J232727.7-020437 using the VLT/HAWK-I camera. They aim to study higher-redshift clusters, which are further away, using galaxies in the K_s band. This is useful as in the near-infrared the atmosphere introduces less distortions and we can obtain sharper images from the ground than in other wavelengths. Galaxies also appear less intrinsically elliptical in this regime. This means, however, that the galaxies we used in Chapter 3 do not really resemble the source population we have in this case.

For other ground-based telescopes, such as the Subaru/Hyper Suprime-Cam, we deal with larger objects as the atmospheric effects are more pronounced. This can also greatly change the biases and creates the need to use simulations with the right parameters.

In this chapter, we study the bias for images using VLT/HAWK-I and Subaru/Hyper Suprime-Cam. We follow a similar procedure as in Chapter 3 but using the input parameters we need to simulate the properties of each telescope. As was done in Chapter 3, we use

real catalogues from images observed with each telescope and analysed with our KSB+ implementation to make sure that the mock galaxy population we are creating resembles the real galaxies.

4.1 VLT/HAWK-I

S18b demonstrate that good seeing VLT/HAWK-I K_s images, which benefit from a sharp PSF (FWHM $\leq 0\farcs4$), yield a similar sensitivity and efficiency for weak lensing studies of clusters at redshift $0.7 \lesssim z \lesssim 1$ as HST/ACS observations when combined with a background selection in gzK_s colour-colour space. They did a pilot study to measure the weak lensing mass of cluster RCS2 J232727.7-020437 which encouraged us to create simulations to obtain a calibration of the shear bias present in VLT/HAWK-I images[1] which can be used in future HAWK-I high-z cluster weak lensing studies of expanded samples. Because the clusters observed with HAWK-I are at higher redshift, the background galaxies will appear redder so we can observe them in near-infrared bands and benefit from their better seeing.

S18b employed the same KSB+ pipeline as used in the previous Chapter for the HST/ACS images, but performing the shape measurements on images in the K_s band. We need to understand the systematics of this particular setup and the corrections coming from signal-to-noise dependencies, to improve the constraints for future studies with expanded samples which are already underway. For this reason, in this section we discuss the results obtained from a new set of simulations, mimicking the VLT/HAWK-I setup and the different galaxy properties in the near-infrared bands. A detailed study of the effects on the bias of choosing different inputs as it was presented before is not reproduced here. Instead, we mainly focus on determining if the signal-to-noise dependent correction obtained in Eq. (3.1) is valid for this setup as well as obtaining an estimate of the residual corrected bias. We did this, first on a grid and later using the real CANDELS positions and magnitudes, following a similar approach to Chapter 3 in order to also study the effect that neighbours have in the bias estimation.

Here we mimic the HAWK-I setup and employ near-infrared-measured galaxy properties, but otherwise largely follow the procedures described in this paper for the generation and analysis of HST-like image simulations (see Chapter 3). We used `GALSIM` to create the simulations but we needed to modify some of our input choices to match the simulated galaxies to the real images obtained with HAWK-I. We still created 10^4 tiles, of 100×100 pixels with a galaxy which had a pixel-level offset from the center of the tile. We also added Gaussian noise and created a separate starfield for the PSF corrections. As was previously explained, we used 50 different shear values for the shear regime $-0.4 < g < 0.4$ (although the bias estimates are obtained on the $-0.2 < g < 0.2$ regime) and created 90-degrees rotated pairs, which reduces the shape noise. The main changes in the simulation input with respect to the ACS-like simulations are those which are intrinsically dependent on the instrument such as a $0\farcs106$ pixel scale and a $0\farcs4$ FWHM Moffat PSF. This means a small change in the

[1] https://www.eso.org/sci/facilities/paranal/instruments/hawki.html

implementation as we use a continuous function for the PSF input as opposed to the situation in Chapter 3, where we used real images. This should not introduce major differences, as the subsampling we used for the HST/ACS PSF tries to reduce the influence the pixelation has on the creation of the simulations, and effectively behave as a continuous function. The use of a Moffat PSF, however, is one of the critical differences when compared to the HST/ACS analysis. In Sect. 3.1.7, we presented a ACS-like simulation using a Moffat PSF. It might be tempting to use that as a comparison with the results here, but this comparison is not straightforward because of the radically different source population and the larger PSF sizes due to the ground-based observations. This is the reason that creating completely new simulations for each setup is needed.

To select the correct light profile distribution for the HAWK-I-like mock galaxies, we used the 3D-HST CANDELS light profile fits (van der Wel et al. 2012; van der Wel et al. 2014) as a reference by randomly drawing a galaxy from the catalogue and using their Sérsic index, half-light radius and ellipticity as input for one mock galaxy. In these catalogues, they fitted Sérsic profiles, and measured the other galaxy properties on real galaxy of the CANDELS fields obtained in the F160W band which is the closest available HST filter to the HAWK-I K_s-band. We changed the input Sérsic indices with respect to the analysis in Chapter 3, where the properties were obtained from observations with the F814W filter which is not a good approximation to the galaxies we see in the near-infrared. The F160W filter we had in these 3D-HST catalogues, despite not being the exact wavelength we were simulating, it is much closer than F814W and therefore, a better match to our HAWK-I galaxies. We expect the galaxies to have similar properties in F160W and K_s so this should not introduce large discrepancies in our results. To use these catalogue as our input, we mimicked colour-selected ($(z - K_s) > \mathrm{MIN}[g - z, 2.5]$) galaxies up to $K_s = 24.2$ (as they do in S18b). However, we studied the impact of using a colour-selected Sérsic index input distribution compared to using the full population. The Sérsic index distribution for the full sample (in blue), compared to the colour-selected sample (in green) are shown in Fig. 4.1 and we can see that they have negligible differences. Both index distributions are quite similar to the distribution used for the ACS-like analysis, also having a peak around 1 and with a median of 1.25 for the full sample and 1.37 for the colour-selected one. This means, as we discussed before, that we have a larger number of exponential galaxies in our analysis. Considering the results in Sect. 3.1.5, which indicates that small changes in the Sérsic index distribution have only subpercent influence on the obtained bias, we do not expect large differences between the bias estimates for both setups. And in fact, the small differences between these distributions change the measured bias at the $\sim 0.5\%$ level only. This also indicates that the differences in the bias caused by the use of a slightly different band as our input should be negligible. In order to have the more realistic scenario we used the colour-selected sample for the bias estimation in this section.

In these simulations we had a smaller intrinsic ellipticity dispersion for the near-infrared galaxies as was shown in S18b. In Sect. 3.1.6, we showed that this had a negligible impact in our estimation of the bias. In any case, since we used the ellipticity coming from the 3D-HST catalogues, we had a input $\sigma(|\epsilon|) = 0.22$ in our mock galaxies, which comes directly from using real catalogues.

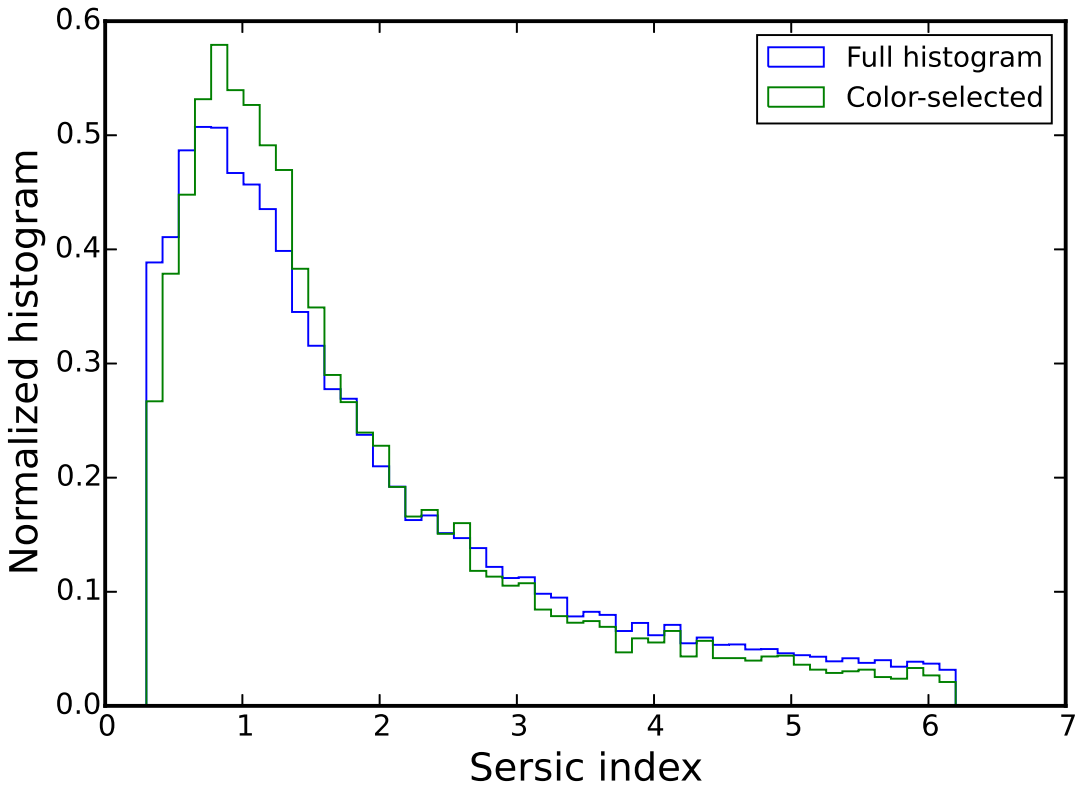

Figure 4.1: Comparison of the distribution of Sérsic indices between the full population (in blue) and the colour selected galaxies (in green) for the HAWK-I simulations.

As explained before, we used the Sérsic index, size and ellipticity of one galaxy in the CANDELS catalogues as input which helps us to capture correlations between these properties. This, as was discussed before, can play an important role in our estimations, especially for lower resolution images. The magnitude correlations were not included here as we used real HAWK-I cluster observations for those. This is motivated by the fact that the catalogues from which we obtained the galaxy shape parameters are observed in a different band and using them as input for the magnitudes could modify our signal-to-noise dependencies.

As was previously done in Chapter 3, in order to have a comparison of our mock galaxies with the real data, we need to compare the statistical properties of both populations. For the comparison of the signal-to-noise ratios (both $S/N_{\rm KSB}$ and $S/N_{\rm flux}$) as well as the size and magnitude distributions, we used catalogues from existing HAWK-I cluster observations analysed in S18b with the same KSB+ implementation. These are colour-selected and have the properties of the galaxies used for the shape determination in clusters. We matched our output distributions with the distribution of these real catalogues, which is shown in Fig. 4.2. As was discussed before in Sect. 3.1, the output and input distributions are not necessarily

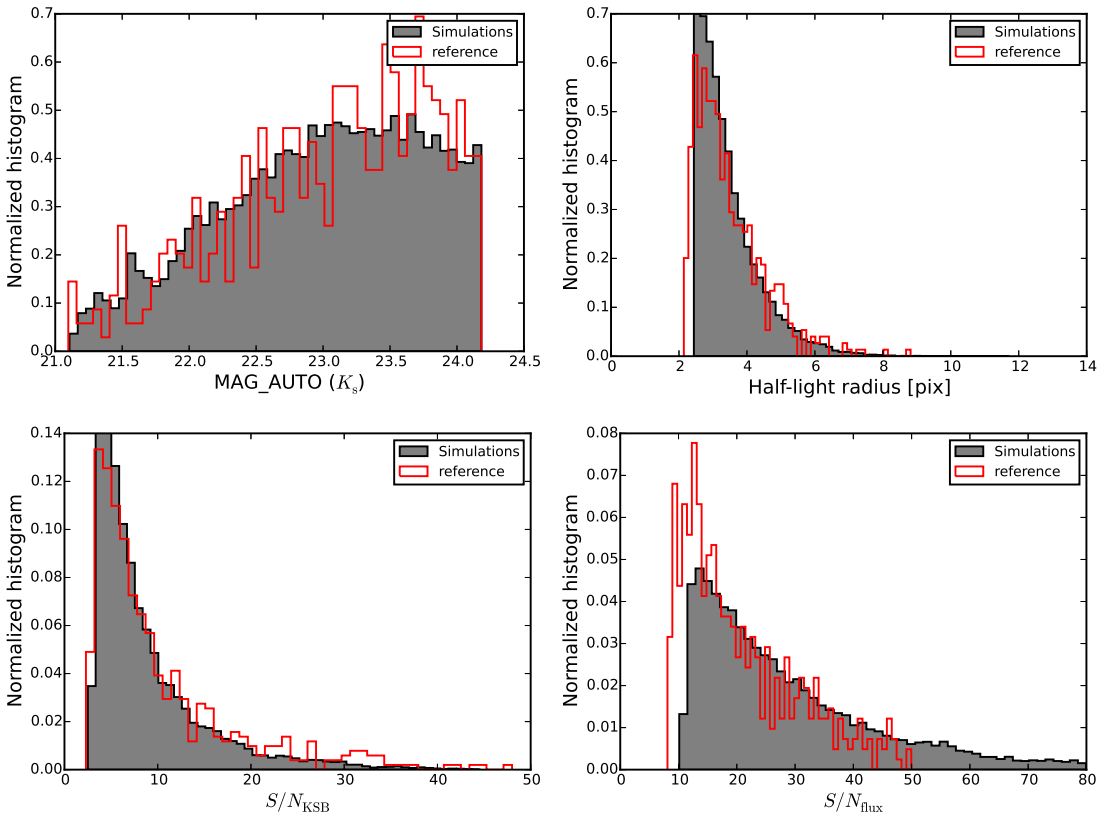

Figure 4.2: Comparisons between the measured distributions in the HAWK-I like simulations and the real image distribution for the magnitudes (MAG_AUTO), the half-light radius measured by `SExtractor`, the KSB signal-to-noise ratio $S/N_{\rm KSB}$ and the `SExtractor` $S/N_{\rm flux}$.

the same, which makes it difficult to have the right properties for our galaxies. However, these are negligible effects that do not change the results shown here. We can see, in Fig. 4.2, good matches for all distributions, with a small discrepancy only in the $S/N_{\rm flux}$ for small signal-to-noise.

4.1.1 Bias from galaxies on a grid

With all these changes, we could expect that there is a need for a $S/N_{\rm KSB}$-dependent correction, and that the one calibrated in Eq. (3.1) for the ACS-like simulations does not properly correct for HAWK-I mock galaxies. The aim of this section is to understand how different the $S/N_{\rm KSB}$ is when compared to the results in Chapter 3. For this, we set up simulations with isolated galaxies placed on a grid, as was done in Sect. 3.1. Using the same correction that was derived there (Eq. 3.1), the residual multiplicative bias we obtained is on the $< 1\%$ level (see Table 4.1), which indicates that there is no need for a new correction for this new setup. Furthermore we plotted the bias dependence on $S/N_{\rm KSB}$ compared to the correction

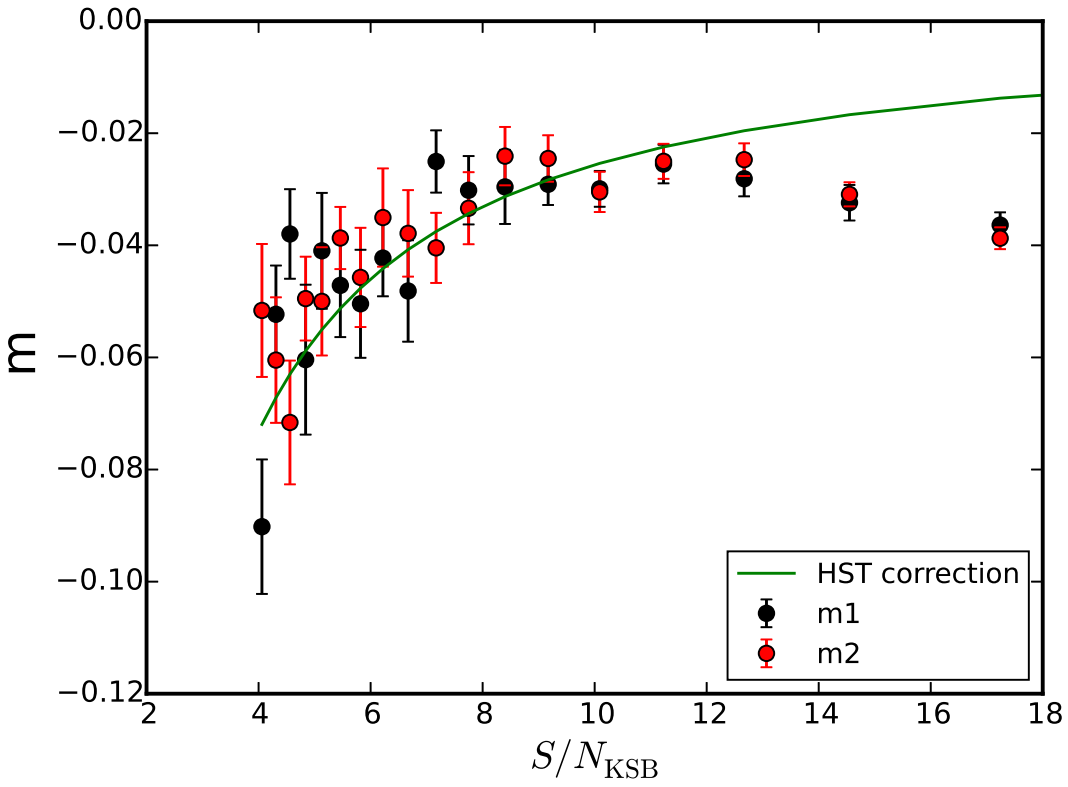

Figure 4.3: Multiplicative bias as a function of S/N_{KSB} in 20 signal-to-noise bins. We show the S/N_{KSB}-dependent correction from Eq. (3.1) which is computed on the ACS-like simulations in green.

Table 4.1: Multiplicative and additive bias for the HAWK-I-like simulations after a cut on $S/N_{\mathrm{flux}} > 10$ and the S/N_{KSB}-dependent correction. These estimates are computed over the shear regime $|g| < 0.2$.

	m	c
e_1	-0.0020 ± 0.0039	0.0010 ± 0.0009
e_2	-0.0019 ± 0.0033	0.0005 ± 0.0009

obtained for the ACS-like simulations in Fig. 4.3. We see that it does not perfectly capture all effects, but due to an overcorrection at small scales and an undercorrection at large scales, the average bias seems to stay low. This indicates that the S/N_{KSB}-dependent correction behaves robustly also for the HAWK-I-like simulations and can be implemented in further weak lensing analysis using $\mathrm{K_s}$ shape estimates. Cautiously we also assume here that the rest of the analysis of the influence of the input parameter should also apply here. In Table 4.1 we show the multiplicative and additive bias, obtained over the $|g| < 0.2$ shear regime for $S/N_{\mathrm{flux}} > 10$. Using a lower S/N_{flux} cut (as we do in Chapter 3) is not possible for this setup,

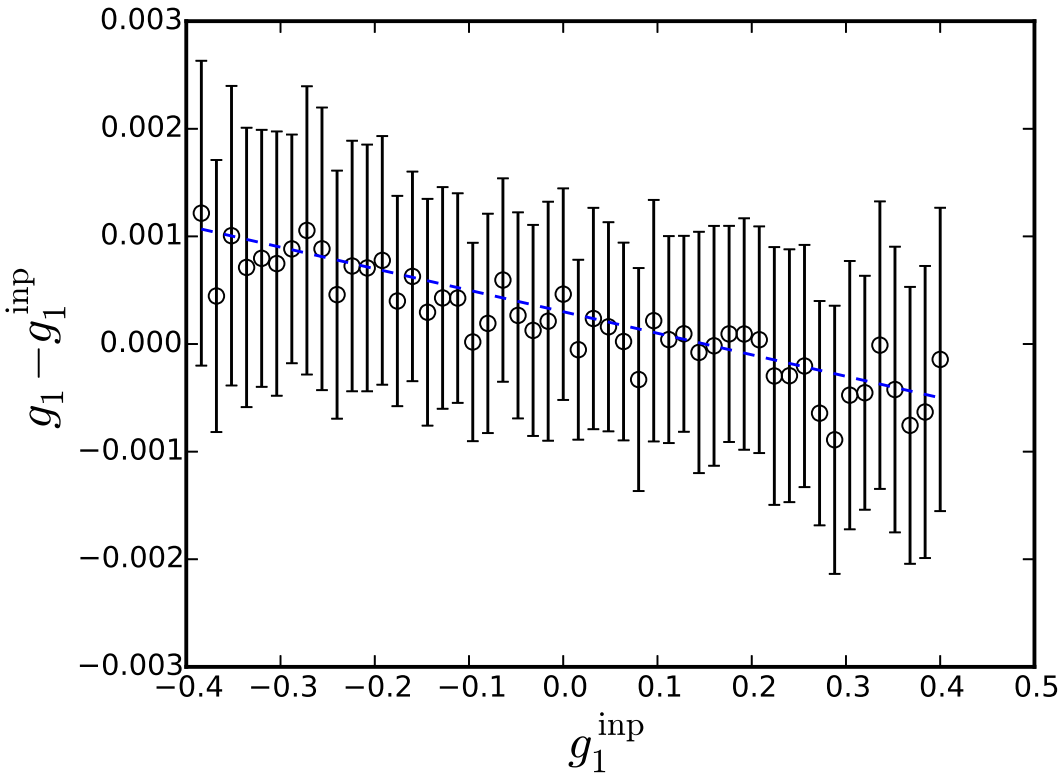

Figure 4.4: Residual multiplicative bias of the first component as a function of input shear for $S/N_{\rm flux} > 10$ galaxies for the HAWK-I-like simulations. This bias estimate is computed after the $S/N_{\rm KSB}$-dependent correction from Eq. (3.1).

as we do not have many galaxies with $S/N_{\rm flux} < 10$ (see bottom right panel of Fig. 4.2). In Fig. 4.4, we show the corresponding dependence of the residual bias as a function of the input shear for $S/N_{\rm flux} > 10$, for the first component. The dashed blue line corresponds to the linear fit for which we obtain the parameters in Table 4.1. We show the full shear regime we created, and see that the strange effect at large shears is not present for this setup. Since the PSF is circularly symmetric in this case, as we are using a Moffat profile, this is not surprising (see Sect. 3.1.7).

4.1.2 CANDELS positions and magnitudes

For a more realistic approach we created a set of simulations using the real CANDELS catalogues as input for the magnitude and position of our galaxies, using a similar implementation to what was done in Sect. 3.3.2, but with the HAWK-I galaxy and telescope properties. We continued using the 3D-HST catalogues as a reference like it was done for the grid setup, but now they provided the input for the position and magnitude of our galaxies as well as

Table 4.2: Comparison of the measured residual multiplicative bias for the HAWK-I-like simulations using the grid positions and the CANDELS positions and magnitudes after a $S/N_{\rm flux} > 10$ cut.

	m_1	m_2
Grid simulation	-0.0020 ± 0.0039	-0.0020 ± 0.0033
CANDELS-like simulation	-0.0190 ± 0.0042	-0.0182 ± 0.0030

their shape. One advantage of using these catalogues is that we have the Sersic profiles of all galaxies and we can create a simulation with the realistic shapes, positions and magnitudes. This was not possible for the HST/ACS setup in Sect. 3.3.2. The rest of the inputs (such as PSF models or pixel scale) were left the same as for the previous section.

As it was already discussed in Chapter 3, using real CANDELS catalogues may not account for the full impact of the faint galaxies in the simulations, depending on how deep the input catalogues are, but it can provide a first estimation of their importance. In fact, the CANDELS catalogues on the F160W band we used are only complete up to $H_{160} = 25$ magnitudes. Since for our estimates we employ our source galaxies until $K_{\rm s} = 24.2$, they are not even one magnitude deeper (and in a different band) than our source population. This, obviously means that we cannot capture the full effect neighbours have on the bias determination, but it can already provide a first estimation of their effect.

We show the residual multiplicative bias in Table 4.2, compared to the bias measured for the grid simulations. We found a $\sim -1\%$ change due to the effect of neighbours. For ground-based data, we expect this effect to be larger than for space-based analysis, so the fact that we already see a 1% effect when only including galaxies less than 1 magnitude fainter than our source galaxies, is not surprising. However, it is difficult to compare these results to what was found for the ACS-like simulations, since we are dealing with a very different source population. Source populations which include fainter galaxies, are expected to suffer from a larger effect due to the clustering of galaxies of similar magnitude. The complexity of this issue indicates that for future surveys it is critical to create simulations that properly include this effect in order to reduce the uncertainties on the bias.

Selection bias is an important effect that should be taken into account as was already seen in Chapter 3. We estimated the contribution of selection bias for the HAWK-I-like simulations by following the same procedure detailed in Sect. 3.3.1. In the previous estimates of the residual bias, such as in Table 4.2, we have required matched pairs, which neglects any selection bias. When separately computing an estimate for it, we found a selection bias of $m_1 = -0.0135 \pm 0.0032$ and $m_2 = -0.0141 \pm 0.0027$. This is smaller than what was found for the ACS-like simulation (see Sect. 3.3.1). But this is not surprising due to the different galaxy populations between the two.

The total change (including selection bias) of the bias due to the more realistic clustering of galaxies is on the $\sim -3.3\%$ level for the HAWK-I-like simulations, which is slightly smaller than what we had for the HST/ACS simulations. However, it is important to keep in mind that the CANDELS catalogues used for these simulations, are only complete up to 0.8 magnitudes deeper than the original background source population. According to Euclid Collaboration

et al. (2019), this is not enough to capture the full effect that faint galaxies have on the bias estimates.

In any case, this behaviour provides a good indication that the $S/N_{\rm KSB}$-dependent correction obtained for the HST/ACS mock galaxies, can also be applied in this case. Using Eq. (3.12) as a correction in this HAWK-I setup we obtained a residual multiplicative bias of $m_1 = 0.0082 \pm 0.0025$ and $m_2 = 0.0088 \pm 0.0028$ for $S/N_{\rm flux} > 10$. This shows an over-correction for this setup, which is understandable as we do not account for the full neighbouring effects.

4.2 Hyper Suprime-Cam

Deep high-resolution observations from HST (as discussed in Chapter 3) or the VLT/HAWK-I setup (discussed in Sect. 4.1) deliver weak lensing sensitivities for studies of clusters at redshift $z \gtrsim 0.7$ that cannot be reached using seeing-limited optical imaging, for which most background sources remain unresolved. Nonetheless, ground-based optical weak lensing data are becoming available for increasing sky areas, making them interesting e.g. for stacked analyses of large sample of high-z clusters. We therefore investigate in this section how accurately our pipeline is able to recover the weak lensing signature of high-redshift clusters in such deep ground-based images obtained under excellent (0.″5–0.″7) seeing conditions.

As an example we analysed a set of simulated images that mimick the properties of deep I-band observations obtained with Hyper Suprime-Cam (HSC, Miyazaki et al. 2012b) on the Subaru telescope[2] as part of the Hyper Suprime-Cam Subaru Strategic Program (Aihara et al. 2018b). A detailed weak lensing analysis of HSC-like image simulations was presented by Mandelbaum et al. (2018c), demonstrating a $\sim 1\%$ general shear recovery accuracy for their shape catalogue (Mandelbaum et al. 2018b) when limiting it to a conservative depth of $i < 24.5$. Aiming at high-z cluster studies we pushed deeper in our analysis in order to increase the background source density. This is simplified by the fact that we only need to achieve an accurate shape calibration for the background-selected galaxies and not the full source population (which covers a wider range in source properties).

The changes we implemented for the HSC-like simulations in this section when comparing to the rest of this work come, again, from the particulars of the telescope and detector setup. The pixel scale of this camera is 0.″2/pixel and the PSF FWHM we select is the average in the typical PSF sizes (0.″6). This means that we have a much lower resolution for these galaxies that the two setups before. Galaxies appear larger in HSC observations due to the stronger impact of atmospherical distortions at these wavelengths. This, fundamentally changes the shape of galaxies we can observe and can lead to very different bias estimates. The PSF model also changes and we used the most realistic available model for our simulated data. It was obtained from the so-called PSF picker[3] which was provided along with the public release of the HSC data. This code does not have an option to create a subsampled PSF, so we interpolated the value of the pixels and transformed it into a smaller pixel grid to effectively

[2] https://www.naoj.org/Projects/HSC/

[3] https://hsc-release.mtk.nao.ac.jp/doc/index.php/tools/

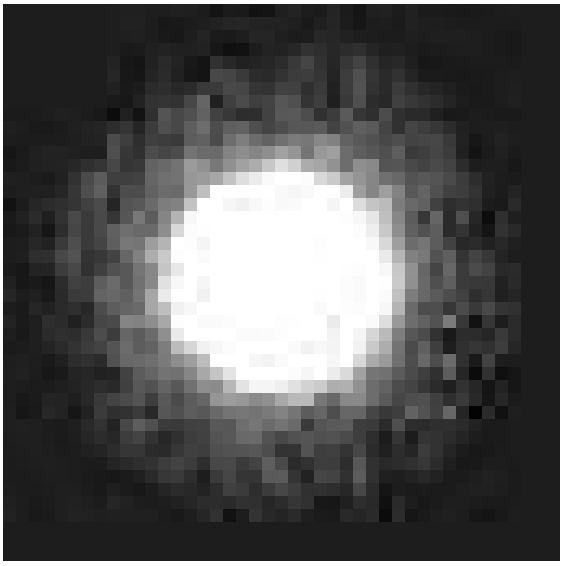

Figure 4.5: The PSF model used for the HSC-like simulations

obtain a subsampling of 3, similar to what was used in Chapter 3. This allows for `GALSIM` to create our mock galaxies without pixelation issues. We tested that this subsampling did not modify the PSF in any meaningful way or introduced artificial biases, and thanks to the smoothness of the profile this was not the case. We also created simulations with different PSFs from the PSF picker by varying the positions and observing dates in order to test how the particulars of the PSF model influence the results. More details on this are discussed in Sect. 4.2.1. An example of one of such PSFs used in this analysis can be seen in Fig. 4.5. As it is clear from the images, the HSC PSF is very different from the HST/ACS PSF in Chapter 3 as it does not have sharp features like we had in the previous case, which can drastically affect the bias measurement.

The setup we used for the creation of these simulations was slightly different from what was explained in Chapter 3 and Sect. 4.1. For the HSC-like simulations we used real images as direct input and not using the parameters obtained through a fit to the images (which was the approach taken before). This is an available option in `GALSIM` which allows to take galaxy cut-outs from the COSMOS field observations and use them as base for our galaxies, instead of creating our mocks from synthetic profiles. Using images as input is a more realistic approach, but it is not possible to do if the PSF size of the simulations is comparable with the PSF size in the real input images. This is due to the fact that real images are already affected by the effects of a PSF. In order to use them we need to perform a deconvolution with a model for their original PSF and re-convolve them with a PSF image which resembles the real PSF of the images we are simulating. If the original PSF and the new PSF are of comparable size, this process creates an artificial pattern in the images that does not exist in real images and does not allow us to obtain any meaningful results. Since the input images were taken with HST, which is a sky-based telescope with great resolution, the PSF for the

HST/ACS-like images in Chapter 3 was the same and these effects dominated over the noise so we could not use the real images and needed to implement the parametric fits. In the case of the HSC discussed in this section, we have a different situation because the PSF size used in the simulations is much larger than the PSF size of the input images used to create the mocks, it is always one order of magnitude larger than the HST/ACS PSF. This allows for the use of real HST/ACS images as direct input for our mock galaxies, which provides a more realistic morphology due to the inclusion of irregularities in the galaxy light profile instead of a simple smooth synthetic profile. To test how this choice influences the measured bias, we compared the use of synthetic profiles (the approach taken in Chapter 3) and the use of real images. This was studied by using the same random selection of objects with the same properties to create one set of simulations for each approach. The obtained bias differed only at the level of 10^{-3}, which is negligible for the uncertainties we obtain in our analysis. Following this small difference we can infer that we can use both approaches in a similar way and obtain consistent results. However, the more realistic simulations will provide a more robust measurement of the bias, so we choose to work with the real images in this section.

We needed to properly match the properties of our input galaxies before we used them as base for our mocks. For this, we performed colour cuts in the catalogue, to select galaxies with photometric redshifts larger than ~ 1 and remove foreground and cluster member contamination. We based our colours in the catalogue from Ilbert et al. (2009), which contains photometric redshifts of galaxies in the 2-deg^2 COSMOS field. It contains most of our galaxies and their magnitudes in 30 bands. More modern catalogues of the COSMOS field, such as COSMOS2015 (Laigle et al. 2016), do not contain information on the g-band, which is used for the colour selection of our galaxies. For this reason, we used the older catalogue Ilbert et al. (2009), despite not being as complete, and lacking some of our objects, by matching the galaxy cut-outs using their sky coordinates with the galaxies in the reference catalogue. After this, we selected galaxies with $g - i < 0.4$ as this removes the cluster members from our sample. The photometric redshifts of the colour-selected galaxies is shown in Fig. 4.6. Since the clusters are around $z \sim 0.5$ to $z \sim 1$, we have selected galaxies which are mainly background galaxies and thus the kind of galaxies we are interested in. The small residual contamination of foreground objects we can see in the mock galaxies, will also be present in real shear measurements using the same colour selection as this process does not completely remove all objects we are not interested on. This fits with our goal of reproducing systematics we have in the real shear analysis. Since we have the photometric redshift information of all these galaxies, we could simply select them to be used as input to our simulations by using their photometric redshifts. This, however, would be less realistic since we do not know the redshift of all our sources in the real analysis. Our aim to mimick the whole analysis process is the reason why we decided to take the colour-selected sample as input.

The main advantage of using real images is that we did not need to assume any particular size, ellipticity or Sérsic index distribution to use as input. This makes the colour-selection on our input galaxies more important, but has the advantage that the correlations between parameters are already included by default. However, the sample of images used as input have magnitudes up to $I_{814} = 25.2$ which is not the same we have in our real cluster observation.

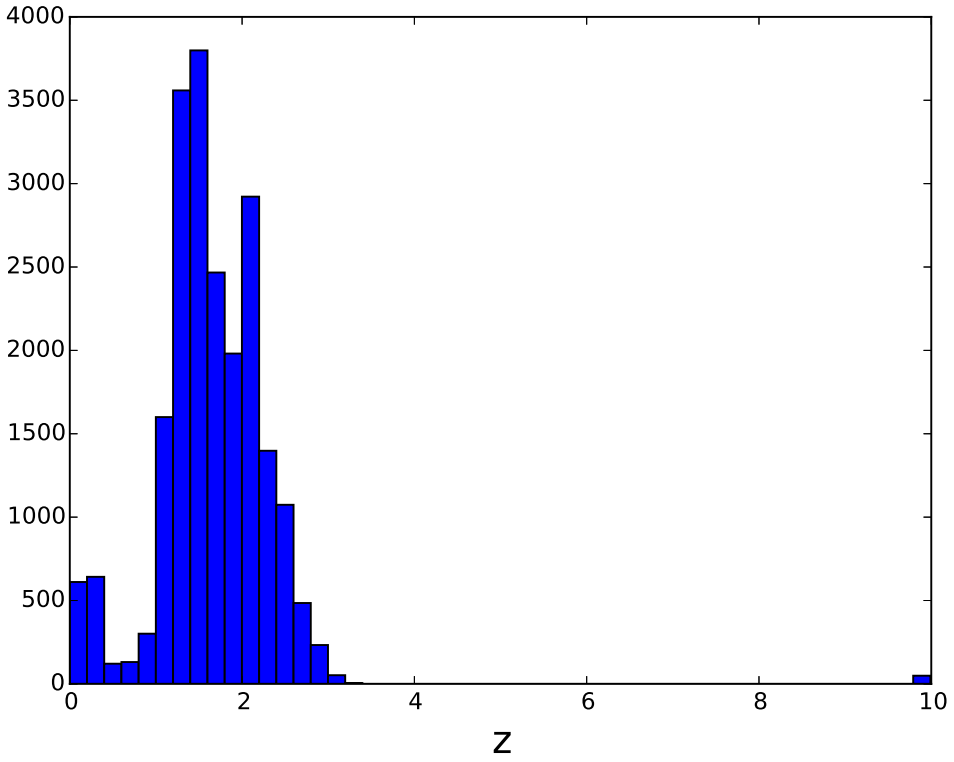

Figure 4.6: The photometric redshift distribution of the colour-selected input sample for the HSC simulations.

In order to match the cluster observations in HSC, we created simulations with slightly fainter magnitudes, up to $i = 25.5$, (note the slightly different filter due to the different telescope) by modifying the input magnitude of the real images accordingly.

As it was done in previous sections, we need a way to compare the mock galaxies with our real images to make sure that we have realistic mocks. To obtain a comparison of the S/N_{KSB}, S/N_{flux}, magnitude and size between simulated and real galaxies, we used catalogues from real HSC cluster observations which were analysed using the same KSB+ pipeline as for the rest of this work. Their measured distributions can be compared to the output parameter obtained from the simulations, which is done in Fig. 4.7. We can, again, see that the matching is not perfect, but as it was argued before, such small discrepancies do not greatly influence our results. Similar to the ACS-like simulations, we tuned some of the input functions, such as the magnitude and the level of the noise in order to resemble the real data parameter distributions. The transformation from flux to magnitudes was also recalibrated using these real image catalogues to obtain the right magnitudes in the HSC i-band.

The first simulation setup was placing our galaxies in a grid, allowing us to study the bias for isolated galaxies. Following the analysis in Sect. 4.1, we studied the validity of the

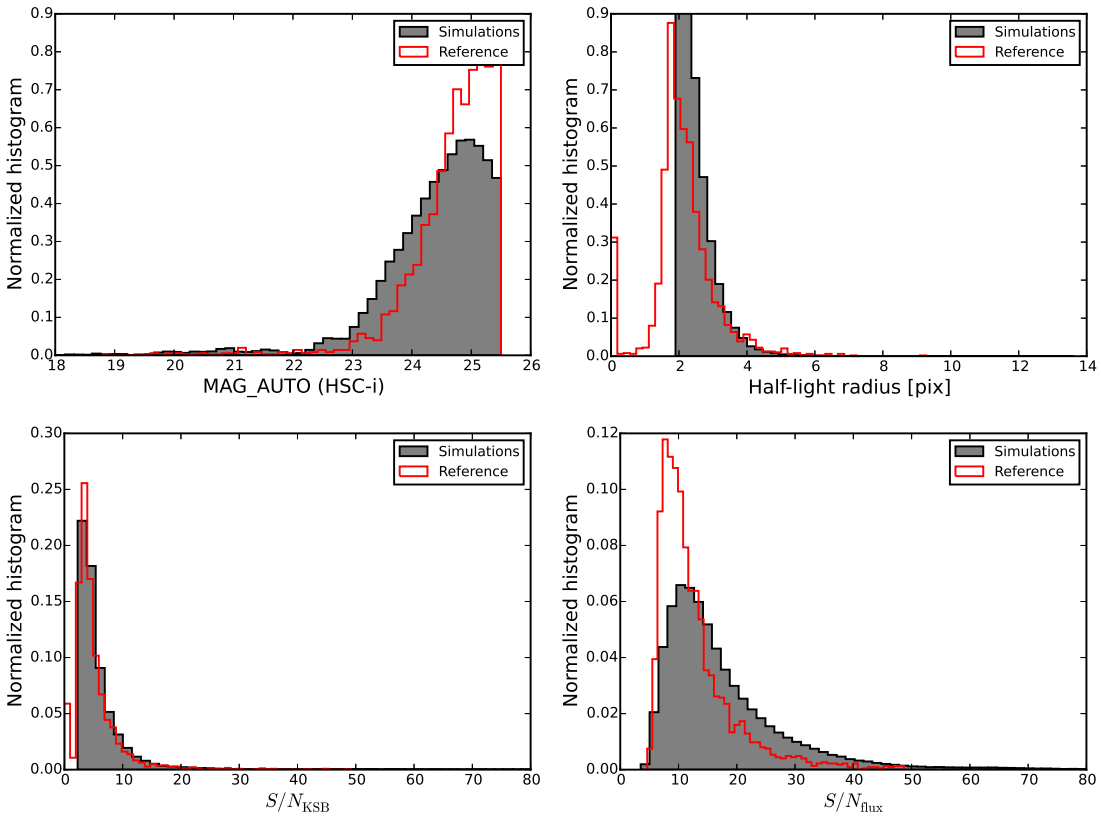

Figure 4.7: Comparisons between the measured distributions in the HSC like simulations and the real image distribution for the magnitudes (MAG_AUTO), the half-light radius measured by `SExtractor`, the KSB signal-to-noise ratio $S/N_{\rm KSB}$ and the `SExtractor` $S/N_{\rm flux}$.

$S/N_{\rm KSB}$-dependent correction. We found that the bias dependence on the $S/N_{\rm KSB}$ for this sample is very different to the ACS-like simulations in Chapter 3 as it is shown in Fig. 4.8. There we can see the points that show the bias measured in 20 signal-to-noise bins with the same number of galaxies in each bin. This is done separately for both components. We also plotted the correction from S10 in blue and the ACS-like correction obtained in Chapter 3 in green. Comparing them, we can see that the dependence here is noisier at the low signal-to-noise end but flatter and with an overall larger bias. This indicates that a new correction can really improve the results so we used the same functional form and recomputed it here. With the correction obtained in Chapter 3, we obtain a $\sim -5\%$ bias, which indicates that we can improve the correction. This recalibration, however, allows us to implement it in future work with real HSC clusters and trust the measured shears obtained using this correction to within 1%. Using the same functional form, the correction for HSC observations is

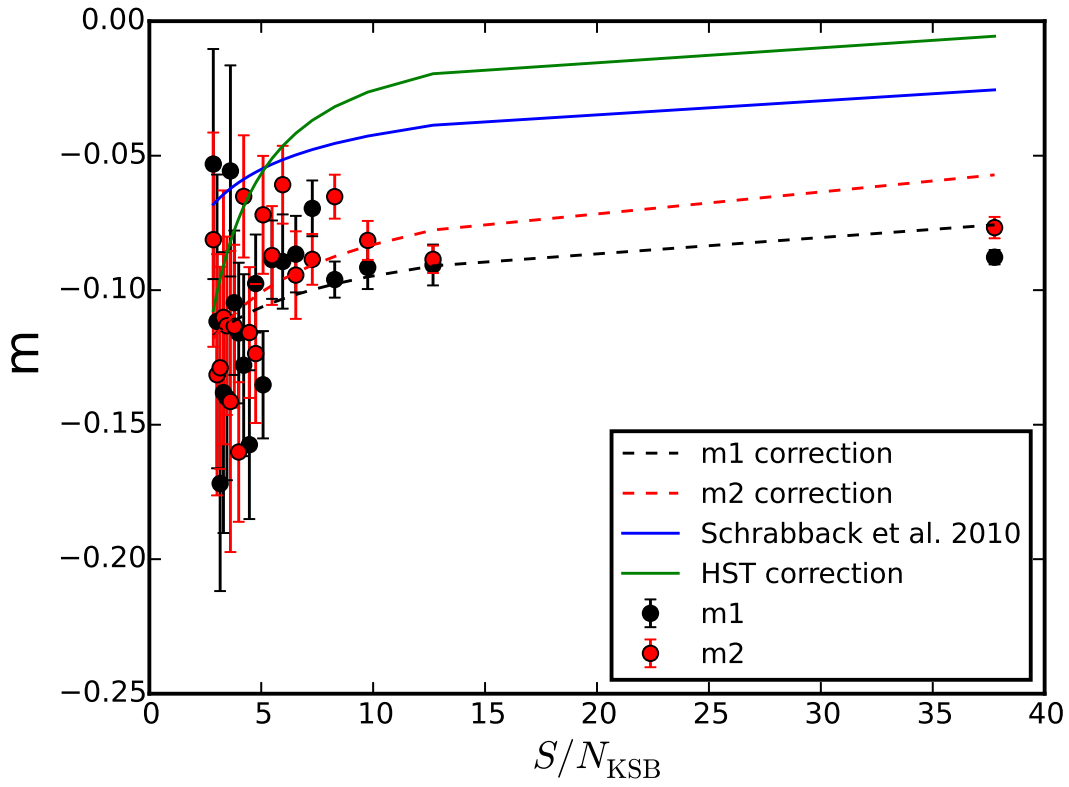

Figure 4.8: The S/N_{KSB} dependence of the bias for the HSC simulations. Shown here are also the corrections from S10 and from Eq. (3.1), computed for the ACS-like simulations. The two dashed lines correspond to the fitted correction obtained from the data for both components.

$$
\begin{aligned}
m_{1\mathrm{corr}} &= -0.139 \left(S/N_{\mathrm{KSB}}\right)^{-0.168} , \\
m_{2\mathrm{corr}} &= -0.158 \left(S/N_{\mathrm{KSB}}\right)^{-0.281} .
\end{aligned}
\tag{4.1}
$$

It follows how the simulated data behaves much better as is it shown in Fig. 4.8 where we plotted the correction of each of the two components with a dashed line.

With this correction, we obtained a bias result for the real images, using our colour-cut sample which can be seen in Table 4.3. The residual bias is below 1% for both $S/N_{\mathrm{flux}} > 10$ and $S/N_{\mathrm{flux}} > 7$. This indicates that it behaves robustly for both signal-to-noise ratio cuts. A plot of the dependence of the difference between the measured and input shear as a function of the input shear is shown in Fig. 4.9. This plot shows the bias for our colour-selected $S/N_{\mathrm{flux}} > 10$ galaxies after the correction from Eq. (4.1). This is a noisier estimate due to the larger seeing and lower signal-to-noise ratios. The effect at large shears discussed in Sect. 3.1.7 seems to also appear here, but due to the noisiness we cannot say how significant

Table 4.3: Residual multiplicative and additive bias for the reference HSC simulations, with colour-selected real galaxies as input. The new correction in Eq. (4.1) was implemented and we show the results for two $S/N_{\rm flux}$ cuts.

		m	c
$S/N_{\rm flux} > 10$	e_1	-0.0037 ± 0.0016	-0.0020 ± 0.0005
	e_2	-0.0012 ± 0.0017	-0.0023 ± 0.0006
$S/N_{\rm flux} > 7$	e_1	-0.0094 ± 0.0016	-0.0031 ± 0.0005
	e_2	-0.0083 ± 0.0020	-0.0015 ± 0.0006

Table 4.4: Residual multiplicative bias for the different colour cuts applied to the input galaxies. They are corrected by the $S/N_{\rm KSB}$-dependent correction from Eq. (4.1), which was computed in the $g-i<0.4$ sample. For the results shown here we only use galaxies with $S/N_{\rm flux} > 10$.

Sample	m_1	m_2
$g-i<0.4$	-0.0037 ± 0.0016	-0.0012 ± 0.0017
$g-i<0.3$	-0.0102 ± 0.0031	-0.0106 ± 0.0031
Full sample	-0.0257 ± 0.0020	-0.0219 ± 0.0020

it is.

Additionally, we tested the changes in the multiplicative bias due to the use of colour cuts to select the input galaxies. We compared the results obtained with the full sample and using only galaxies with $g-i<0.4$ as an input. We also compared the case when we selected galaxies with a more restricted colour-cut $g-i<0.3$ which removes more cluster members at the cost of also removing more galaxies overall. All this is shown in Table 4.4. We see a $\sim 2\%$ change from the full sample to the colour-selected sample, but we only obtain a $\sim 0.5\%$ change when varying the colour threshold from 0.4 to 0.3.

4.2.1 PSF variation across the field

According to the results in Chapter 3, there are two key parameters in the creation of the simulations. One of them, the Sérsic index selection is irrelevant here, due to the use of real images, which should account for the real intrinsic galaxy shapes. The second one is the PSF model used, which is studied in more detail in this subsection. We present the differences coming from choosing a slightly different PSF model to use as input for our simulated HSC images. In order to study this, we selected 25 random different PSFs from the PSF picker, which each has different properties. Each of them was selected from different coordinates of the survey and behaves differently. In particular, in order to quantify the bias change, we focussed here on the bias dependence with the ellipticity of the PSF. This seemed to be important in the case of the ACS-like simulations as was discussed in Sect. 3.1.7 so it is interesting to see what the situation is here.

Different sets of simulations were created with the same input properties (only varying the

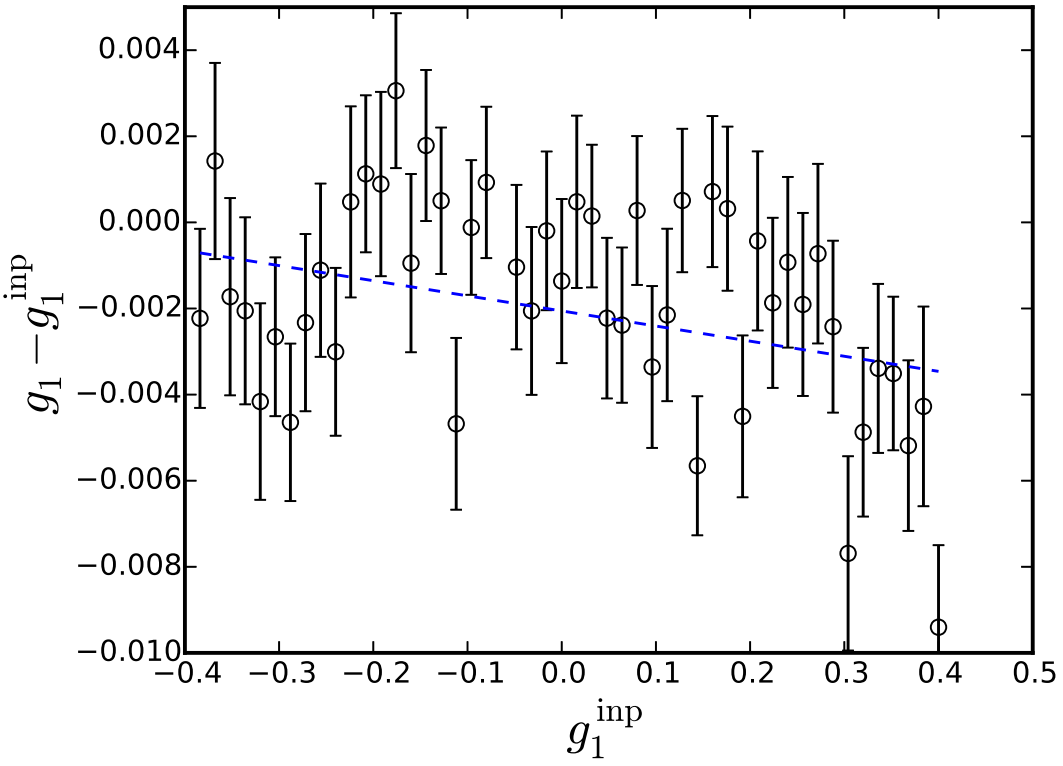

Figure 4.9: The difference between measured and input shear as a function of the input shear for the colour-selected sample with a $S/N_{\rm flux} > 10$ cut and the HSC $S/N_{\rm KSB}$-dependent correction from Eq. (4.1). The blue dashed line is the linear fit which estimates the bias that in reflected in Table 4.3.

PSF) in order to properly compare the differences that come from the changes in the PSF only. The aim of this setup was to test the dependence of the multiplicative and additive bias with the PSF ellipticity. The measurement of the ellipticity was performed by KSB+ using the second-order moments of the stars which we created in a separate starfield. We then averaged all the individual ellipticities of each star to obtain the mean ellipticity of the PSF in such image.

We looked at changes in both the multiplicative and additive bias in Fig. 4.10, where we plotted the obtained bias for each simulation as a function of the PSF ellipticity of the random PSF model. In black we show the bias and ellipticity of the first shear component, and in red of the second one. The differences in the ellipticity ranges covered by each component should not be important for this analysis and is possibly due to the random choice of PSF models or from an asymmetry of the PSF. For the multiplicative bias we see on the upper left panel of Fig. 4.10, a large scatter, but no clear trend. For the additive bias, on the upper right panel, we see a larger bias for larger ellipticities. This is expected since we showed in Sect. 3.1.7 that the additive bias has a dependence with the PSF ellipticity. This seems to also be the case in

the HSC simulations. When we look at the dependence of the cross component, that is, of the bias measured in one shear component as a function of the PSF ellipticity of the other (shown in the middle row in Fig. 4.10), we see that the behaviour switches. In this case, there is some correlation for the multipicative bias and not for the additive bias. When we look at the total ellipticity of the PSF, on the bottom panels of Fig. 4.10, we see no clear dependence of the multiplicative or additive bias. From here, we can get two types of information. On the one hand, the dependence on the total PSF ellipticity is negligible and on the other hand, the scatter of the bias estimation is quite large, which indicates that the uncertainties obtained for the bias according to our simulations should be on the 3% level. The large scatter is not ideal as it makes it almost impossible to properly calibrate the bias at a sufficiently precise level. Real observations will each have a different PSF which can greatly change the bias, so we would need to calibrate it for each particular observing condition. In future work, it would be worth testing how this dependence changes with the use of different and more modern shape measurement methods.

4.2.2 Correlated noise

All the analysis in this work had so far assumed uncorrelated Gaussian noise. Now, for the first time, we show how the noise correlations impact our estimates of the bias. In Mandelbaum et al. (2018a), they described that HSC images have a pixel-level correlation noise as shown in Fig. 4.11 which comes from the co-addition of the single exposures into the final image. This correlation was implemented into our simulations by using the `GALSIM` tools for the addition of the noise. All other inputs were kept the same as in the beginning of this section, in order to make sure that the bias changes are due to the noise.

We obtained a $\sim 0.1\%$ change in the bias due to this correlated noise. Such small difference in the bias indicates that the addition of correlated noise at this level does not influence the shear measurements. And for this reason we do not concern ourselves with this issue for the rest of this work. We cannot compare our results with Mandelbaum et al. (2018a) as there is no estimation of how large is this effect for their work since they include the correlated noise for all their samples.

4.2.3 CANDELS-like simulations

In order to study the effect of neighbours in our simulations for the Subaru/HSC setup, we followed the same idea as in Sect. 3.3.2 and Sect. 4.1.2. We created more realistic simulations using the CANDELS catalogues as inputs for realistic positions and magnitudes. The other properties stayed the same as they were in the rest of this section to study the impact of neighbours. Using the CANDELS catalogues should mostly capture the effects that neighbours introduce in the analysis, since in the real catalogues we have the clustering of faint galaxies. In the case of the I-band (F814W), which is used in the Subaru/HSC setup, the CANDELS field observations are complete up to $I_{814} \sim 27$, which is 1.5 magnitudes fainter than the $i < 25.5$ limit used for our source population. This indicates that it should

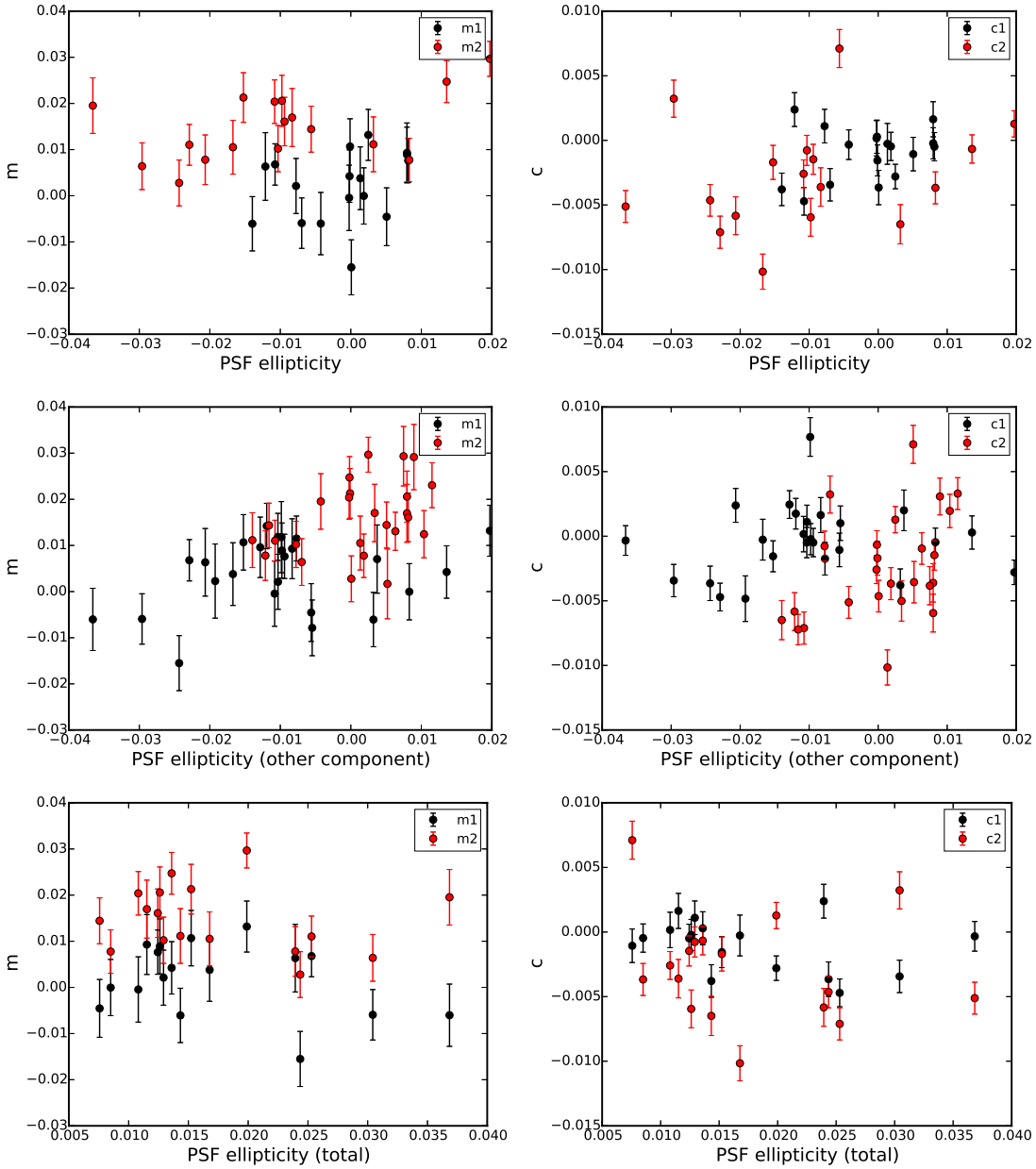

Figure 4.10: Obtained residual multiplicative (left) and additive (right) bias comparison with different PSFs with different ellipticities. The different lines of panels show the bias vs the PSF ellipticity measured in the same component, the other component and the total ellipticity. In black we show the bias estimates of the first component and in red of the second.

capture almost the full effect from neighbours, which is a different situation with what was found in the case of HST/ACS and VLT/HAWK-I setups (see Sect. 3.3.2 and Sect. 4.1.2).

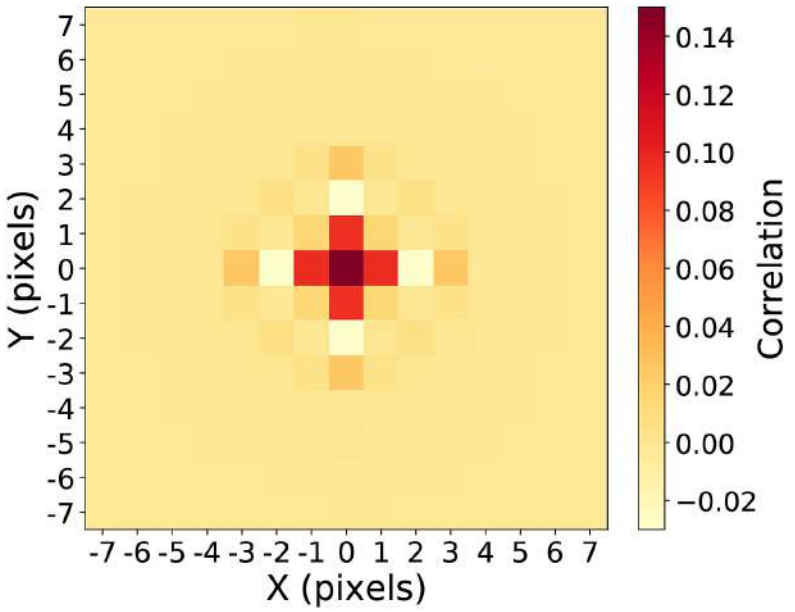

Figure 4.11: The pixel level correlation of the noise. Credit: Mandelbaum et al. (2018a)

Table 4.5: Table with the values for the multiplicative bias of the simulations for isolated galaxies on a grid and for simulations using the correct CANDELS positions and magnitudes. This is shown here for $S/N_{\rm flux} > 10$ galaxies. They are corrected by the same $S/N_{\rm KSB}$-dependent correction computed from the sample without neighbours (Eq. 4.1). No selection bias is present here as we required matched pairs.

PSF	m_1	m_2
No neighbours	-0.0037 ± 0.0016	-0.0012 ± 0.0017
CANDELS mocks	-0.0209 ± 0.0050	-0.0194 ± 0.0044

We show the results in Table 4.5, where we can see there is a $\sim -1.8\%$ shift when we include the realistic positions and magnitudes from real catalogues. For the inclusion of galaxies 2 magnitude fainter in the ACS-like simulations (Sect. 3.3.3), we obtained a similar shift. Since here we only capture 1.5 magnitudes fainter, we would expect an even larger bias for a simulation with galaxies up to $I_{814} = 27.5$, including the full contribution from faint galaxies. This is what is expected as the HST/ACS has a better resolution, and should be less affected from neighbours and blends than the Subaru/HSC. For a cut on $S/N_{\rm flux} > 7$, we also obtain a large effect, with a $\sim -2.5\%$ bias shift.

The selection bias computed over the unmatched pairs can further modify the bias, as it was previously discussed for the other telescope setups (see Sect. 3.3.1). We estimated this effect is $m_1 = -2.05\% \pm 0.35\%$ and $m_1 = -1.97\% \pm 0.29\%$ for the HSC-like setup. This means that accounting for the residual and selection bias for the realistic positions and magnitudes, we need to modify the correction computed on the grid simulation (Eq. 4.1) to

be

$$
\begin{aligned}
m_{1\mathrm{corr}} &= -0.139 \left(S/N_{\mathrm{KSB}}\right)^{-0.168} - 0.041\,, \\
m_{2\mathrm{corr}} &= -0.158 \left(S/N_{\mathrm{KSB}}\right)^{-0.281} - 0.039\,.
\end{aligned}
\tag{4.2}
$$

The final test on how accurate this correction account for the joint effect of selection bias and the effect of neighbours can be done by computing the residual bias not requiring matching pairs in the rotated catalogues. After the correction from Eq. (4.2), we obtain a residual multiplicative bias of $m_1 = -0.0015 \pm 0.0026$ and $m_2 = -0.0017 \pm 0.0020$ for galaxies with $S/N_{\mathrm{flux}} > 7$. Considering the CANDELS catalogues are complete up to 1.5 magnitudes fainter, this should include almost the full contribution of the faint galaxies and the selection bias as opposed to what happened in the last two telescope setups (ACS and HAWK-I).

4.3 Final considerations

In this chapter, we partially reproduce the analysis done in Chapter 3 and apply it to different telescope setups. No estimation of the effect of bright cluster members is done for the HAWK-I-like or HSC-like simulations. This was found to be negligible for the ACS-like setup and, even though we expect a slightly larger effect in this case due to the poorer resolution, it also is a function of the number counts, which are expected to be lower here. This is the reason why we do not include this effect.

From the results presented here, we can gather that the different signal-to-noise cuts do not radically change the bias, and hence, we can use lower cuts (up to $S/N_{\mathrm{flux}} > 7$) and still obtain robust bias estimates. The error budget stays around the 1% level for both setups.

As opposed to the case in Chapter 3, a detailed analysis of the different simulation inputs is also not included in this chapter, so no estimation of the extra uncertainties is added. We assume, following from the analysis shown in Sect. 3.1, around a 1% uncertainty due to the simulation mismatching should account for that. For the HSC-like simulations, the light profile of the galaxies is better constrained, due to the use of real images, so the uncertainty in this case is marginally lower.

CHAPTER 5

Mass reconstruction of relaxed clusters

The use of simulations is key to calibrate the shear measurement methods in order to obtain robust mass estimates of clusters, which was done in Chapters 3 and 4. In this chapter we present a mass estimate of real clusters observed by the HST/ACS, and using the updated calibrations from Chapter 3. We computed the mass estimates of three of the most relaxed galaxy clusters in the 2,500 deg^2 South Pole Telescope Sunyaev-Zel'dovich (SPT-SZ) Survey (Bleem et al. 2015). These clusters are SPT-CL $J0000-5748$, SPT-CL $J2331-5051$ and SPT-CL $J2043-5035$.

As was mentioned in Sect. 2.2, these relaxed clusters have not suffered any recent mergers and have smooth temperature and X-ray profiles. This makes them ideal candidates to serve as an example for the extension of the shear profile to the inner regions. For non-relaxed clusters, it would not be so easy, as their more prominent substructure and less smooth profiles complicate the analysis.

The shear profile of the clusters is measured using the KSB+ algorithm (see Sect. 2.3.3). Galaxies are colour-selected using both the V_{606}-band observations from ACS, where shapes are measured, and the I-band from FORS2 (except for SPT-CL $J2043-5035$, which has ACS mosaics in both bands, and hence we use the I_{814} from HST/ACS), as described in Sect. 2.3.4. The shear profile is then fitted to an NFW profile, assuming a particular concentration, in order to obtain a mass estimate.

5.1 Previous mass estimates

Two of the clusters in this work, SPT-CL $J0000-5748$ ($z = 0.702$) and SPT-CL $J2331-5051$ ($z = 0.576$), were initially studied by S18a, who measured weak lensing shapes using 2×2 HST/ACS mosaic V_{606} images and selected mostly background galaxies using a $V - I < 0.3$ colour cut. For the source selection they used HST I_{814} imaging in the cluster core and VLT I-band imaging in the cluster outskirts. Their measured masses are shown in Table 5.1. In S20 we recently updated these measurements using a revised reference sample for the calibration

Table 5.1: Weak lensing masses for the relaxed clusters in this work from S18a and from S20.

Cluster	M_{500c} (S18a)	M_{500c} (S20)
SPT-CL $J0000{-}5748$	$4.2^{+1.8}_{-1.6} \pm 0.7 \pm 0.3$	$4.1^{+1.7}_{-1.5} \pm 0.8 \pm 0.2$
SPT-CL $J2331{-}5051$	$2.6^{+1.7}_{-1.4} \pm 0.7 \pm 0.2$	$3.3^{+1.9}_{-1.6} \pm 0.7 \pm 0.2$
SPT-CL $J2043{-}5035$	–	$2.9^{+1.5}_{-1.3} \pm 0.7 \pm 0.2$

of the source redshift distribution (Raihan et al. 2020) and employing our revised shear calibration presented in Chapter 3. S20 also incorporate deeper VLT/FORS2 I-band imaging for cluster SPT-CL $J0000{-}5748$ for the source selection, obtained by the ESO programme 0100.A-0217 (PI: B. Hernandez Martin), which includes 10.6ks of integration reaching a limiting magnitude of 27.3. These new observations also correct for some technical issues with the telescope that were present in the old I-band observations.

The third cluster in our sample, SPT-CL $J2043{-}5035$ ($z = 0.723$), had no previous WL mass estimates, but it is studied in S20 using the same calibrations, employing shape measurements from mosaic ACS V_{606} images and a source selection that incorporates mosaic ACS I_{814} imaging for the full cluster field. More details about the particulars of the analysis presented here can be found in S18a and S20.

In S20, for the shear measurements of the cluster we used the KSB+ algorithm which has been explained in detail throughout the rest of this work. For the colour estimates, we used apertures with diameter $0\farcs7$ to estimate the colours in the $V_{606} - I_{814}$ in the inner regions of clusters (and for the full image in the case of SPT-CLJ2043−5035). For the outskirts of the other two clusters, which do not have full HST/ACS mosaics in the I_{814}, we use VLT/FORS2 I-band observations to determine the colours. In this case, we need to first convolve the HST/ACS data with a Gaussian with the size of the VLT/FORS2 PSF to perform a PSF homogeneisation to obtain consistent estimates for the aperture fluxes in both bands. We also apply a galactic extinction correction from Schlegel et al. (1998).

The updated results with better images in S20 are also shown in Table 5.1. These results employ the updated calibrations presented in this work (see Chapter 3), which already improves the constraints when comparing to the results from S18a.

Several issues are important in order to obtain robust mass estimates. One of them, has been the focus of the previous chapters of this work, which is the shear measurement bias. Other important issues come from the redshift determination of the background galaxies which drastically changes the estimates due to the signal dilution coming from the inclusion of cluster members and foreground galaxies in the population of galaxies for which we estimate the shears. An accurate estimation of the redshift distribution after this selection is discussed in Raihan et al. (2020). These two biases, due to shear measurement and photometric redshifts were found to be small and of opposite sign, partially cancelling each other. The improvement is not so much on the accuracy of the results, but mainly it is the uncertainty levels which are reduced by the updated calibrations. The work presented in the next section takes into account the most updated results in these two fields, as does S20.

5.2 Updated mass estimates

One of the results we obtained in Chapter 3, was the bias estimation for the larger shear regime. This means that we can improve the mass estimates of relaxed cluster by using the inner parts, which exhibit stronger shears, and still achieve a similar accuracy.

For general cluster samples effects such as miscentring and substructure have the biggest impact on the shear profiles in the cluster cores. This is what motivated S18a and S20 to remove the cluster cores from their analysis. They only used scales larger than $r > 500$ kpc for the fitting of the radial shear profiles, avoiding the inner regions for the general population of clusters.

In the case presented in this work, we have only selected relaxed clusters, and therefore, there is the possibility of fitting the radial shear profile for $r > 200$ kpc. The selection of this limit ensures that only reduced shear estimates in the robustly calibrated $|g| \lesssim 0.2$ regime are included in the fit (compare Fig. 5.1). The substructure is not so prominent for these clusters and their centers are more robustly determined so they are the perfect candidates to serve as a test case for obtaining tighter constraints via the inclusion of cluster cores and stronger shears. Here we present a comparison between mass estimates that use shear estimates at $r > 500$ kpc vs. $r > 200$ kpc.

As it was mentioned before, as a primary difference to S20 we include smaller scales ($r > 200$ kpc) in the analysis of the reduced shear profiles of these clusters (see Fig. 5.1). As was explained in Sect. 2.3.5, and following S18a and S20 we fit NFW shear profile models (Wright & Brainerd 2000) accounting for the magnitude dependence of the mean geometric lensing efficiency of the sources and the impact of weak lensing magnification on the source redshift distribution. We assume a concentration–mass relation, in our case, following S20, we employ the relation from Diemer & Joyce (2019, D19 henceforth). Assuming the same relation from D19, we can compare the cluster mass constraints fitted only from scales $r > 500$ kpc and when including the information from the inner cluster regions ($r > 200$ kpc).

We list the mass signal-to-noise ratio $S/N_{\mathrm{mass,D19}} = M_{200\mathrm{c}}/\Delta M_{200\mathrm{c}}$ (considering only shape-noise uncertainties) for both fit ranges and all three clusters in Table 5.2. The last column in that table shows the ratio between the signal to noise ratios with each range. We find an average improvement by a factor of 1.38 when the inner scales are included ($r > 200$ kpc). This illustrates that the introduction of the inner regions into the analysis could potentially improve the constraints on the mass as long as the aforementioned miscentring and substructure issues are under control.

Going a step further, Table 5.3 lists the mass constraints obtained when including the inner cluster regions ($r > 200$ kpc), assuming the D19 concentration–mass relation in the second and third column. The D19 concentration–mass relation should be adequate for a general population of clusters, which are approximately mass-selected. This means that it would provide a good estimate for the works in S18a and S20. However, for relaxed clusters, such as the three ones we have here, we expect a higher concentration by a factor ~ 1.14 (compare Neto et al. 2007). Following the work in S18b we therefore perform an additional estimation of the cluster mass, assuming an increased concentration $c_{200\mathrm{c}} = 1.14 c^{D19}_{200\mathrm{c}}$, where $c^{D19}_{200\mathrm{c}}$ is the concentration that corresponds to the best-fit mass from the initial fit when assuming

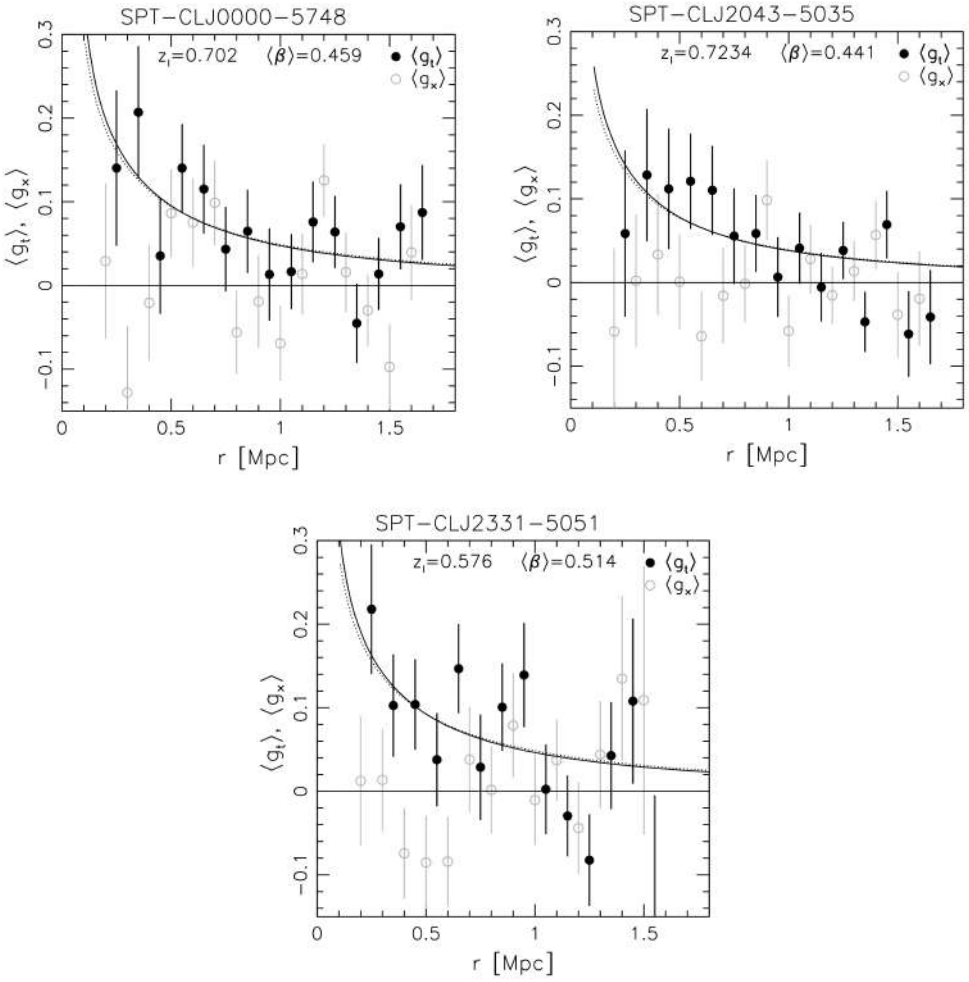

Figure 5.1: Reduced shear profiles around the X-ray centres of the three clusters analysed in this study, showing the tangential (black solid circles) and cross (grey open circles) components. The curves correspond to the best-fitting NFW models assuming the D19 $c(M)$ relation (dotted) and increased concentrations $c_{200c} = 1.14c_{200c}^{D19}$ (solid), which are expected to more accurately represent relaxed clusters.

Table 5.2: Cluster properties and achieved weak lensing mass signal-to-noise ratios.

Cluster	z	$S/N^{>500\mathrm{kpc}}_{\mathrm{mass,D19}}$	$S/N^{>200\mathrm{kpc}}_{\mathrm{mass,D19}}$	$(S/N^{>200\mathrm{kpc}}_{\mathrm{mass,D19}})/(S/N^{>500\mathrm{kpc}}_{\mathrm{mass,D19}})$
SPT-CL $J0000{-}5748$	0.702	2.63	3.25	1.24
SPT-CL $J2043{-}5035$	0.723	2.15	2.61	1.22
SPT-CL $J2331{-}5051$	0.576	1.90	3.19	1.67

Note. — *C*olumn 1: Cluster designation. *C*olumn 2: Cluster redshift from Bleem et al. (2015). *C*olumn 3: Mass signal-to-noise ratio $S/N_{\mathrm{mass,D19}} = M_{200\mathrm{c}}/\Delta M_{200\mathrm{c}}$ (considering only shape-noise uncertainties) obtained from NFW reduced shear profile fits using scales $0.5\mathrm{Mpc} < r < 1.5\mathrm{Mpc}$ and assuming the D19 $c(M)$ relation. *C*olumn 4: Mass signal-to-noise ratio $S/N_{\mathrm{mass,D19}} = M_{200\mathrm{c}}/\Delta M_{200\mathrm{c}}$ (considering only shape-noise uncertainties) obtained from NFW reduced shear profile fits using scales $0.2\mathrm{Mpc} < r < 1.5\mathrm{Mpc}$ and assuming the D19 $c(M)$ relation. *C*olumn 5: Ratio of the values from columns 4 and 3.

the D19 $c(M)$ relation. The resulting mass constraints are also listed in Table 5.3. The differences between the obtained mass using each concentration are only small. These agree within $\sim 1\sigma$ with *C*handra X-ray estimates computed by McDonald et al. (2019) assuming the Y_{X}–M scaling relation from Vikhlinin et al. (2009, compare Table 5.3)

The main sources of uncertainties in this analysis come from the statistical uncertainties (see Table 5.3). The systematic uncertainties, of $\sim 1\%$ for the shear calibration, translates to 1.5% mass uncertainty. Other uncertainties in the analysis come from the mass modelling uncertainty (5.3%) following from S20, in order to reflect possible missrepresentations of the morphology, due to choosing a particular subset of clusters. The scatter on the cluster mass depending on the morphology is robust for the full population, but it might not be as accurate for the relaxed clusters. Another mass uncertainty comes from the calibration of the source redshift distribution is 4.7% (S20). The final total systematic uncertainty is then 7.4%.

Another important issue comes from the complexity of estimating the center of the cluster. Miscentring can cause substantial discrepancies in the mass. S20 use a correction based on N-body simulations, mostly Millennium XXL (Angulo et al. 2012), which works well for the general cluster population. Fortunately, this is not as important for our subset of relaxed clusters which generally have smoother light profiles and the determination of their center with the X-ray profile works relatively well. For this reason this correction is not used in the cluster estimation presented in this work. This means that, on average, the estimated masses of the clusters are lower when comparing to S20.

Table 5.3: Weak lensing constraints derived for the fit range 0.2Mpc $< r <$ 1.5Mpc.

	Using $c(M)$ from D19			Using $c_{200c} = 1.14c_{200c}^{D19}$		
Cluster	M_{200c}	M_{500c}	c_{200c}^{D19}	M_{200c}	M_{500c}	M_{500c,Y_X}
SPT-CL*J* 0000−5748	$5.6^{+1.8}_{-1.7} \pm 0.7 \pm 0.3$	$3.8^{+1.3}_{-1.1} \pm 0.5 \pm 0.2$	3.72	$5.2^{+1.7}_{-1.5} \pm 0.7 \pm 0.3$	$3.7^{+1.2}_{-1.1} \pm 0.5 \pm 0.2$	$4.1^{+0.7}_{-0.6}$
SPT-CL*J* 2043−5035	$4.2^{+1.7}_{-1.5} \pm 0.6 \pm 0.3$	$2.8^{+1.2}_{-1.0} \pm 0.4 \pm 0.2$	3.66	$3.9^{+1.6}_{-1.4} \pm 0.7 \pm 0.3$	$2.8^{+1.1}_{-1.0} \pm 0.5 \pm 0.2$	$4.2^{+0.1}_{-0.2}$
SPT-CL*J* 2331−5051	$5.7^{+1.8}_{-1.7} \pm 0.8 \pm 0.4$	$3.9^{+1.3}_{-1.2} \pm 0.5 \pm 0.3$	3.69	$5.2^{+1.7}_{-1.6} \pm 0.7 \pm 0.3$	$3.6^{+1.2}_{-1.1} \pm 0.5 \pm 0.2$	$4.3^{+0.3}_{-0.4}$

Note. — *C*olumn 1: Cluster designation. *C*olumn 2: M_{200c} constraints obtained when assuming the $c(M)$ relation from D19. *C*olumn 3: M_{500c} constraints obtained when assuming the $c(M)$ relation from D19. *C*olumn 4: Concentration derived from the D19 $c(M)$ relation for the best-fit M_{200c}. *C*olumn 5: M_{200c} constraints obtained for a fixed concentration $c_{200c} = 1.14c_{200c}^{D19}$. *C*olumn 6: M_{500c} constraints obtained for a fixed concentration $c_{200c} = 1.14c_{200c}^{D19}$. The statistical uncertainties listed for the mass constraints correspond to shape noise (asymmetric), uncorrelated large-scale structure projections, and line-of-sight variations in the source redshift distribution. The systematic mass uncertainty amounts to 7.4%. *C*olumn 7: *C*handra X-ray mass estimates computed by McDonald et al. (2019) assuming the Y_X–M scaling relation from Vikhlinin et al. (2009).

CHAPTER 6

Conclusions

The challenge of simulating real weak lensing observations has many difficulties, since a profound understanding of the real properties of galaxies and the telescope setup is required. In the case of the galaxy properties, it is not possible, as we can only obtain the observed properties of the objects and not the intrinsic ones. However, only a realistic simulation, which properly captures the galaxy population, can provide the correct bias that our measurement introduces in the analysis. Using the wrong inputs for our mock galaxy properties can introduce artificial biases and completely change the results. This means that since the real parameters are unknown we need to at least understand how robust the bias estimation is to possible discrepancies. This work has successfully emulated observations from three different observing setups in order to constrain the uncertainties that shear estimation, and hence the estimation of cluster masses through weak lensing, has.

We have also presented a detailed analysis of the input parameters for the creation of HST/ACS cluster image simulations and studied which input choices influence the bias estimation the most and need to be carefully matched. These are mainly the light profile distribution of the galaxies and the PSF properties. With regards to the PSF, the ellipticity of the PSF model used, in particular, seemed to largerly affect the results for the stronger shear regime. The light profile, needs to be roughly correct, although small discrepancies do not introduce large changes in the bias.

We aimed to constrain the uncertainties on the bias to the $1-2\%$ level, as this is sufficient for current and near-future work in galaxy cluster weak lensing studies, while capturing the different effects that contribute to the bias measurements. By calibrating the signal-to-noise ratio-dependent correction using our simulations with galaxies placed on a grid, we have reduced the uncertainty on the noise bias and captured most of the dependence the bias has. The contribution of the faint, neighbouring galaxies is key for a realistic simulation, as it changes the bias estimates on the $\sim -3\%$ level. One aspect, often neglected, is the contribution of the selection bias on the shear estimates. The approach typically taken in shear calibration studies of creating rotated pairs to reduce shape noise effectively cancels selection bias. We found that this effect is on the $\sim -1.5\%$ level, so it is important to include

it. For the simulations which included faint neighbours, the validity of the correction obtained on the isolated galaxies needed to be tested. We saw that a shift to this correction was sufficient to roughly capture the joint dependence of shape measurement and selection bias on signal-to-noise ratio and since the results without matched pairs are much noisier, we chose this approach rather than completely recalibrating it for the CANDELS-like simulations. The last ingredient we needed was the study of the changes in the bias due to the presence of cluster members, which is a cluster-specific issue, not needed for cosmic shear analyses. For this reason, it is normally not included in the bias estimation through simulations. Here we, nonetheless, estimate it to be a small contribution of $\sim +0.3\%$ (plus a change in selection bias of $\sim +0.6\%$). We also found a dependence of this effect with cluster redshift.

We showed that extending the simulated shear regime to $|g| < 0.2$ provides robust estimates, but the full $|g| < 0.4$ includes an unexpected behaviour for strong shears, which deviates from the linear relation found at weaker shears. We should note that for the strong end of this regime, the galaxies would also be affected by flexion which is not included in our simulations. Fortunately, this regime is not typically used so we only show it as an example, but compute the bias estimation using shears up to $|g| < 0.2$ (for the main results). For the first time using our KSB+ pipeline, we have studied the larger shear regime and incorporated fainter galaxies, down to $S/N_{\rm flux} = 7$. Including the lower signal-to-noise galaxies changes the bias by $\sim -0.5\%$ and the total uncertainties are unchanged, so the estimates for $S/N_{\rm flux} > 7$ are still in the accepted uncertainty range and this cut provides a larger number of galaxies to be included in the cluster mass measurement, which can provide better mass constraints since weak lensing benefits from the inclusion of more galaxies in the analysis.

The most important result from this work is an estimation of the uncertainty level of the bias, which is on the $\sim 1.5\%$ level, enough for the aims of this work. This uncertainty mostly comes from the uncertainty on the simulation input choices. This makes us confident the results presented here can be used in future cluster studies using KSB+ on HST/ACS images.

Simulating observations from other telescopes, we obtained similar results although we performed a less detailed analysis. For the VLT/HAWK-I cluster simulations, we saw that the same $S/N_{\rm KSB}$-dependent correction is still applicable to capture the noise bias dependencies. An analysis of galaxies on a grid compared to the use of real galaxy positions allows us for a partial estimation of the contribution neighbours and blends have on the shape measurement as well as the selection bias. This is slightly smaller ($\sim -2.4\%$), but comparable to the level we found for the space-based simulations. However, the input catalogues used for this setup do not include galaxies faint enough to estimate the full contribution to the bias from faint undetected galaxies. All this indicates that the weak lensing cluster analysis of HAWK-I observations is very comparable to the higher-resolution HST images due to the fact that ground-based images appear sharper when observed in the near-infrared regime. In the case of the Subaru/HSC images, we had a different scenario. The ground-based optical observations taken with HSC have very different properties due to a larger seeing and poorer resolution. A new correction was needed as the bias is overall larger, but particularly for the low S/N regime. With this new correction, however, we can reach similar residual bias and uncertainties to the previous two setups. The inclusion of other effects such as correlated noise (which was found to be negligible), a different colour selection of the background

galaxy population, and the importance of PSF variations is also presented. We included realistic galaxy positions and magnitudes to capture the impact of neighbours. Because of this poorer resolution we find that the effect of neighbours and blends is larger than for the previous two setups, changing the bias by $\sim -4\%$. This is still lower that what was found in Mandelbaum et al. (2018a), also for HSC mock images. However, we use a different shear measurement algorithm and implement colour-cuts to select our galaxies. A final estimation for the full residual bias (including selection bias effect) stays within the $\sim 1\%$ uncertainty regime. We should note, however, that some of the effects, such as the bright cluster members are not included in this setup. The bias estimated with the different S/N cuts also remain within the tolerated uncertainty values.

The final part of this work is an application of the results from Chapter 3 to the real analysis of cluster images taken by HST/ACS. With the new correction and the final bias estimation, we recomputed the masses of three relaxed clusters from the 2,500 deg^2 SPT-SZ Survey using the updated corrections and the extended shear regime. Our 1.5% uncertainty on the mass calibration translates into a 2.3% systematic mass uncertainty. Extending the radius regime to the inner part of the clusters, ($r > 200\,\mathrm{kpc}$ instead of $r > 500\,\mathrm{kpc}$ as used by S18a and S20), we can better constrain the mass, obtaining improvements in S/N of a factor 1.38. This was just an example of the application of the results from this work. It indicated that further work on this topic and better corrections for the low signal-to-noise galaxies can further tighten the constraints.

This work has been dedicated to cluster weak lensing studies which is opposed to the current trends in the literature that focus on cosmic shear. Both take similar approaches in most things, but cluster simulations has the benefit of allowing for looser constraints as the shears are stronger. However, the addition of neighbouring galaxies becomes more important as clusters have a larger galaxy density. We aimed to capture most of the different effects that contribute to our shear estimations, and obtain robust corrections for each of the telescope setups.

This kind of work is critical for next generation surveys and I hoped to shine light on some of the more critical issues that need to be considered when creating new simulations. More modern shape measurement techniques will further reduce the uncertainties and remove some of the issues found here as they are heavily dependent on the exact implementation that we are using. A very promising approach to circumvent the problem of creating realistic simulations, especially for future surveys which will probe even deeper regions of the Universe, is the so-called metacalibration approach in Huff & Mandelbaum (2017). They use real images from the survey they are calibrating and transform them as they would be if they suffered from a stronger weak lensing. This allows them to remove the need of simulations and simply compare the results with and without this extra weak lensing effect, which can provide a more realistic estimation of the bias.

When comparing to previous work, we find similar importance of the contribution of faint undetected galaxies to the results in Euclid Collaboration et al. (2019). The study of the selection bias has also been an important conclusion of very recent work (e.g. Kannawadi et al. 2019) and has been corroborated here. Similarly, Kannawadi et al. (2019) performed an analysis of the influence of the simulation input parameter on the bias estimation, reaching

similar conclusions. The main contribution of this work to the larger shear estimation community is the testing of cluster-specific issues and the extension to stronger shear regimes. This has proven to be very promising for relaxed clusters, including larger numbers of source galaxies, which provide more precise estimates of the mass.

As the shortcomings of this work, the lack of enough time to create much larger sets of simulated images caused the uncertainty levels not to be as low as they could be. Furthermore, since in Chapter 3 we were simulating HST/ACS images, which are some of the best-quality data available, we could not use any better resolution catalogues as input for our galaxy properties, as it is done in works simulating ground-based observations (such as Chapter 4). This could be improved with the use of deeper observations with even better resolution to create input galaxy catalogues with a closer estimation of the true galaxy properties. Furthermore, the treatment of certain effects as independent, such as the cluster member addition, might not be sufficiently accurate for the tighter constraints of future studies. For these, a combined simulation setup containing all different effects would provide a much better approach. We also assumed independent distributions for some of the parameters and ignored more complex morphologies of the galaxies, which impacts the bias estimation.

KSB+ has been useful for the current uncertainties, but this work has shown that a calibration uncertainty lower than 1.5% might not be achievable with KSB+. For this, other approaches, such as metacalibration, which do not require simulations, or other methods which have a more robust PSF correction (e.g. Bernstein et al. 2016) can be more useful.

In summary, the use of a larger number of simulations which target the stronger shear for cluster images and account for flexion effects, as well as the development of new methods, can help us obtain better mass estimates and reach the required accuracy for future surveys. This work has helped understand the calibration of the shear bias and has helped tighten the constraints on future studies of large samples of galaxy clusters at high redshift. In particular, these results were already used in S20 and will also be applied to future HAWK-I cluster analysis.

Bibliography

Abbott, B. P., Abbott, R., Abbott, T. D., et al. 2016, Phys. Rev. Lett., 116, 061102

Aihara, H., Armstrong, R., Bickerton, S., et al. 2018a, Publications of the Astronomical Society of Japan, 70, S8

Aihara, H., Armstrong, R., Bickerton, S., et al. 2018b, Publications of the Astronomical Society of Japan, 70, S8

Allen, S. W., Evrard, A. E., & Mantz, A. B. 2011, Annual Review of Astronomy and Astrophysics, 49, 409

Angulo, R. E., Springel, V., White, S. D. M., et al. 2012, MNRAS, 426, 2046

Applegate, D. E., von der Linden, A., Kelly, P. L., et al. 2014, MNRAS, 439, 48

Bahcall, N. A. & Cen, R. 1993, The Astrophysical Journal Letters, 407, L49

Bartelmann, M. 1996, Astronomy and Astrophysics, 313, 697

Bartelmann, M. & Schneider, P. 2001, Physics Reports, 340, 291

Bayliss, M. B., Hennawi, J. F., Gladders, M. D., et al. 2011, VizieR Online Data Catalog, J/ApJS/193/8

Beckwith, S. V. W., Stiavelli, M., Koekemoer, A. M., et al. 2006, The Astronomical Journal, 132, 1729

Bellagamba, F., Sereno, M., Roncarelli, M., et al. 2019, MNRAS, 484, 1598

Bernstein, G. M., Armstrong, R., Krawiec, C., & March, M. C. 2016, MNRAS, 459, 4467

Bertin, E. & Arnouts, S. 1996, AAP, 117, 393

Bharadwaj, S., Sethi, S. K., & Saini, T. D. 2009, Physical Review D, 79, 083538

Bleem, L. E., Stalder, B., de Haan, T., et al. 2015, The Astrophysical Journal Supplement Series, 216, 27

Blinnikov, S. & Sorokina, E. 2004, Astrophysics ans Space Science, 290, 13

Bocquet, S., Dietrich, J. P., Schrabback, T., et al. 2019, The Astrophysical Journal, 878, 55

Böhringer, H., Pratt, G. W., Arnaud, M., et al. 2010, Astronomy and Astrophysics, 514, A32

Bridle, S., Balan, S. T., Bethge, M., et al. 2010, MNRAS, 405, 2044

Buote, D. A. & Tsai, J. C. 1995, The Astrophysical Journal, 452, 522

Caraveo, P. A., De Luca, A., Mignani, R. P., & Bignami, G. F. 2001, The Astrophysical Journal, 561, 930

Carlberg, R. G., Yee, H. K. C., & Ellingson, E. 1997, The Astrophysical Journal, 478, 462

Carlstrom, J. E., Holder, G. P., & Reese, E. D. 2002, Annual Review of Astronomy and Astrophysics, 40, 643

de Blok, W. J. G. 2010, Advances in Astronomy, 2010, 789293

de Jong, J. T. A., Verdoes Kleijn, G. A., Boxhoorn, D. R., et al. 2015, Astronomy and Astrophysics, 582, A62

Diemer, B. & Joyce, M. 2019, The Astrophysical Journal, 871, 168

Dietrich, J. P., Bocquet, S., Schrabback, T., et al. 2019, MNRAS, 483, 2871

Dressler, A., Smail, I., Poggianti, B. M., et al. 1999, The Astrophysical Journal Supplement Series, 122, 51

Einstein, A. 1916, Annalen Phys., 49, 769, [Annalen Phys.354,no.7,769(1916)]

Erben, T., Van Waerbeke, L., Bertin, E., Mellier, Y., & Schneider, P. 2001, Astronomy and Astrophysics, 366, 717

Euclid Collaboration, Martinet, N., Schrabback, T., et al. 2019, Astronomy and Astrophysics, 627, A59

Falomo, R., Scarpa, R., Treves, A., & Urry, C. M. 2000, The Astrophysical Journal, 542, 731

Fenech Conti, I., Herbonnet, R., Hoekstra, H., et al. 2017, MNRAS, 467, 1627

Flaugher, B., Diehl, H. T., Honscheid, K., et al. 2015, The Astronomical Journal, 150, 150

Gardner, J. P., Mather, J. C., Clampin, M., et al. 2006, Space Science Reviews, 123, 485

Gillis, B., Schrabback, T., Maggraf, O., et al. 2019, MNRAS, submitted

Gladders, M. D. & Yee, H. K. C. 2000, The Astronomical Journal, 120, 2148

Goldstein, J. H., Ade, P. A. R., Bock, J. J., et al. 2003, The Astrophysical Journal, 599, 773

Grogin, N. A., Kocevski, D. D., Faber, S. M., et al. 2011, The Astrophysical Journal Supplement Series, 197, 35

Heymans, C., Brown, M. L., Barden, M., et al. 2005, MNRAS, 361, 160

Heymans, C., Van Waerbeke, L., Bacon, D., et al. 2006, MNRAS, 368, 1323

Hildebrandt, H., Viola, M., Heymans, C., et al. 2017, MNRAS, 465, 1454

Hill, J. C., Baxter, E. J., Lidz, A., Greco, J. P., & Jain, B. 2018, Physical Review D, 97, 083501

Hoekstra, H., Franx, M., & Kuijken, K. 2000, The Astrophysical Journal, 532, 88

Hoekstra, H., Franx, M., Kuijken, K., & Squires, G. 1998, ApJ, 504, 636

Hoekstra, H., Herbonnet, R., Muzzin, A., et al. 2015, MNRAS, 449, 685

Hoekstra, H., Viola, M., & Herbonnet, R. 2017, MNRAS, 468, 3295

Hubble, E. 1929, Proceedings of the National Academy of Science, 15, 168

Huff, E. & Mandelbaum, R. 2017, arXiv e-prints, arXiv:1702.02600

Ilbert, O., Capak, P., Salvato, M., et al. 2009, The Astrophysical Journal, 690, 1236

Ivezić, v., Tyson, J. A., Acosta, E., et al. 2008 [eprint: [arXiv]0805.2366v4]

Kaiser, N., Squires, G., & Broadhurst, T. 1995, ApJ, 449, 460

Kannawadi, A., Hoekstra, H., Miller, L., et al. 2019, Astronomy and Astrophysics, 624, A92

Kauffmann, G., Heckman, T. M., White, S. D. M., et al. 2003, MNRAS, 341, 33

Khullar, G., Bleem, L. E., Bayliss, M. B., et al. 2019, The Astrophysical Journal, 870, 7

Kissler-Patig, M., Pirard, J. F., Casali, M., et al. 2008, Astronomy and Astrophysics, 491, 941

Koekemoer, A. M., Faber, S. M., Ferguson, H. C., et al. 2011, The Astrophysical Journal Supplement Series, 197, 36

Krist, J. 2003, ACS WFC & HRC fielddependent PSF variations due to optical and charge diffusion effects, Tech. rep.

Krist, J. E., Hook, R. N., & Stoehr, F. 2011, in Optical Modeling and Performance Predictions V, Vol. 8127, 81270J

Laigle, C., McCracken, H. J., Ilbert, O., et al. 2016, The Astrophysical Journal Supplement Series, 224, 24

Laureijs, R., Amiaux, J., Arduini, S., et al. 2011, ArXiv e-prints, arXiv:1110.3193

Luppino, G. A. & Kaiser, N. 1997, ApJ, 475, 20

Mandelbaum, R., Hirata, C. M., Leauthaud, A., Massey, R. J., & Rhodes, J. 2012, MNRAS, 420, 1518

Mandelbaum, R., Lanusse, F., Leauthaud, A., et al. 2018a, MNRAS, 481, 3170

Mandelbaum, R., Lanusse, F., Leauthaud, A., et al. 2018b, MNRAS, 481, 3170

Mandelbaum, R., Miyatake, H., Hamana, T., et al. 2018c, Publications of the Astronomical Society of Japan, 70, S25

Mandelbaum, R., Rowe, B., Armstrong, R., et al. 2015, MNRAS, 450, 2963

Mandelbaum, R., Rowe, B., Bosch, J., et al. 2014, The Astrophysical Journal Supplement Series, 212, 5

Mantz, A. B., Allen, S. W., Morris, R. G., et al. 2015, MNRAS, 449, 199

Mantz, A. B., Allen, S. W., Morris, R. G., et al. 2016, MNRAS, 463, 3582

Massey, R., Heymans, C., Bergé, J., et al. 2007, MNRAS, 376, 13

McClintock, T., Varga, T. N., Gruen, D., et al. 2019, MNRAS, 482, 1352

McDonald, M., Allen, S. W., Hlavacek-Larrondo, J., et al. 2019, The Astrophysical Journal, 870, 85

Merloni, A., Predehl, P., Becker, W., et al. 2012, arXiv e-prints, arXiv:1209.3114

Merritt, D., Graham, A. W., Moore, B., Diemand , J., & Terzić, B. 2006, The Astronomical Journal, 132, 2685

Merten, J., Meneghetti, M., Postman, M., et al. 2015, The Astrophysical Journal, 806, 4

Miyazaki, S., Komiyama, Y., Nakaya, H., et al. 2012a, in , 84460Z

Miyazaki, S., Komiyama, Y., Nakaya, H., et al. 2012b, in Society of Photo-Optical Instrumentation Engineers (SPIE) Conference Series, Vol. 8446, Society of Photo-Optical Instrumentation Engineers (SPIE) Conference Series, 0

Mohr, J. J., Fabricant, D. G., & Geller, M. J. 1993, The Astrophysical Journal, 413, 492

Munari, E., Grillo, C., De Lucia, G., et al. 2016, The Astrophysical Journal Letters, 827, L5

Narayan, R. & Bartelmann, M. 1996, arXiv e-prints, astro

Navarro, J. F., Frenk, C. S., & White, S. D. M. 1995, MNRAS, 275, 56

Navarro, J. F., Frenk, C. S., & White, S. D. M. 1997, The Astrophysical Journal, 490, 493

Neto, A. F., Gao, L., Bett, P., et al. 2007, MNRAS, 381, 1450

Old, L., Wojtak, R., Pearce, F. R., et al. 2018, MNRAS, 475, 853

Planck Collaboration, Ade, P. A. R., Aghanim, N., et al. 2014, Astronomy and Astrophysics, 571, A16

Planck Collaboration, Ade, P. A. R., Aghanim, N., et al. 2011, Astronomy and Astrophysics, 536, A1

Planck Collaboration, Aghanim, N., Akrami, Y., et al. 2018, arXiv e-prints, arXiv:1807.06209

Postman, M., Coe, D., Benítez, N., et al. 2012, The Astrophysical Journal Supplement Series, 199, 25

Press, W. H. & Schechter, P. 1974, The Astrophysical Journal, 187, 425

Pujol, A., Sureau, F., Bobin, J., et al. 2017, ArXiv e-prints, arXiv:1707.01285

Raihan, S. F., Schrabback, T., Hildebrandt, H., Applegate, D., & Mahler, G. 2020, MNRAS, submitted

Ramos-Ceja, M. E., Basu, K., Pacaud, F., & Bertoldi, F. 2015, Astronomy and Astrophysics, 583, A111

Rebolo, R., Battye, R. A., Carreira, P., et al. 2004, MNRAS, 353, 747

Rhodes, J. D., Massey, R. J., Albert, J., et al. 2007, The Astrophysical Journal Supplement Series, 172, 203

Riess, A. G., Casertano, S., Yuan, W., Macri, L. M., & Scolnic, D. 2019, The Astrophysical Journal, 876, 85

Rowe, B. T. P., Jarvis, M., Mandelbaum, R., et al. 2015, Astronomy and Computing, 10, 121

Samuroff, S., Bridle, S. L., Zuntz, J., et al. 2018, MNRAS, 475, 4524

Santos, J. S., Rosati, P., Tozzi, P., et al. 2008, Astronomy and Astrophysics, 483, 35

Schlegel, D. J., Finkbeiner, D. P., & Davis, M. 1998, The Astrophysical Journal, 500, 525

Schrabback, T. et al. in prep.

Schrabback, T., Applegate, D., Dietrich, J. P., et al. 2018a, MNRAS, 474, 2635

Schrabback, T., Erben, T., Simon, P., et al. 2007, Astronomy and Astrophysics, 468, 823

Schrabback, T., Hartlap, J., Joachimi, B., et al. 2010, AAP, 516, A63

Schrabback, T., Schirmer, M., van der Burg, R. F. J., et al. 2018b, Astronomy and Astrophysics, 610, A85

Schroeder, D. J. & Golimowski, D. A. 1996, Publications of the Astronomical Society of the Pacific, 108, 510

Scoville, N., Aussel, H., Brusa, M., et al. 2007, The Astrophysical Journal Supplement Series, 172, 1

Shearer, A., Kanbach, G., Slowikowska, A., et al. 2010, in Proceedings of High Time Resolution Astrophysics - The Era of Extremely Large Telescopes (HTRA-IV). May 5 - 7, 54

Sirianni, M., Jee, M. J., Benítez, N., et al. 2005, Publications of the Astronomical Society of the Pacific, 117, 1049

Skelton, R. E., Whitaker, K. E., Momcheva, I. G., et al. 2014, The Astrophysical Journal Supplement Series, 214, 24

Skidmore, W., TMT International Science Development Teams, & Science Advisory Committee, T. 2015, Research in Astronomy and Astrophysics, 15, 1945

Springel, V., White, S. D. M., Jenkins, A., et al. 2005, Nature, 435, 629

Stalder, B., Stark, A. A., Amato, S. M., et al. 2014, in Society of Photo-Optical Instrumentation Engineers (SPIE) Conference Series, Vol. 9147, Ground-based and Airborne Instrumentation for Astronomy V, 91473Y

Sunyaev, R. A. & Zeldovich, Y. B. 1969, Nature, 223, 721

van der Wel, A., Bell, E. F., Häussler, B., et al. 2012, The Astrophysical Journal Supplement Series, 203, 24

van der Wel, A., Franx, M., van Dokkum, P. G., et al. 2014, The Astrophysical Journal, 788, 28

van Weeren, R. J., de Gasperin, F., Akamatsu, H., et al. 2019, Space Science Reviews, 215, 16

Vikhlinin, A., Burenin, R. A., Ebeling, H., et al. 2009, The Astrophysical Journal, 692, 1033

Viola, M., Kitching, T. D., & Joachimi, B. 2014, MNRAS, 439, 1909

Wambsganss, J. 1999, Journal of Computational and Applied Mathematics, 109, 353

Wen, Z. L. & Han, J. L. 2013, MNRAS, 436, 275

White, M., Hernquist, L., & Springel, V. 2001, The Astrophysical Journal Letters, 550, L129

White, S. D. M., Navarro, J. F., Evrard, A. E., & Frenk, C. S. 1993, Nature, 366, 429

Wright, C. O. & Brainerd, T. G. 2000, The Astrophysical Journal, 534, 34

List of Figures

List of Tables